Basal Ganglia Modulation of Cortical Firing Rates in a Behaving Animal

Citation

Oldenburg, Ian Anton. 2014. Basal Ganglia Modulation of Cortical Firing Rates in a Behaving Animal. Doctoral dissertation, Harvard University.

Basal Ganglia Modulation of Cortical Firing Rates in a Behaving Animal

A dissertation presented

by

Ian Antón Oldenburg

to

The Division of Medical Sciences

In partial fulfillment of the requirements

for the degree of

Doctor of Philosophy

In the subject of

Neurobiology

Harvard University

Cambridge, Massachusetts

July, 2014

Dissertation Advisor: Professor Bernardo L. Sabatini Ian Antón Oldenburg

Basal Ganglia Modulation of Cortical Firing Rates in a Behaving Animal

Motor cortex, basal ganglia (BG), and thalamus are anatomically arranged in a recurrent loop whose activity is hypothesized to be involved in the selection of motor actions. Direct (dSPN) and indirect (iSPN) striatal projection neurons receive excitatory input from cortex, and are thought to oppositely modulate cortical activity via BG output to thalamus. Here, we test the central tenets of this model in head-restrained mice performing an operant conditioning task using optogenetic manipulation of dSPNs and iSPNs to determine the effects of activity in each pathway on primary motor cortex. We find that dSPN and iSPN activation has bidirectional, robust, and rapid effects on motor cortex that are highly context-dependent, with distinct effects of each pathway during quiescent and active periods. Thus, the effects of activity in each pathway are at times antagonistic and consistent with classic models, whereas in other behavioral contexts the two pathways will work in the same direction or have no effect at all. In a separate but related project, we describe a direct projection from the globus pallidus externa (GP), a central nucleus of the BG, to frontal regions of the cerebral cortex (FC), which is not typically included in models of BG function. Two cell types make up the GP-FC projection, distinguished by their electrophysiological properties, cortical projection patterns and expression of choline acyteltransferase (ChAT), a genetic marker for the neurotransmitter acetylcholine. These cholinergic GP cells receive basal ganglia input and bidirectionally modulate firing in FC of awake mice. Since GP-FC cells receive dopamine sensitive inhibition from iSPNs and dSPNs, this circuit reveals a pathway by which neuropsychiatric pharmaceuticals can act in the BG and yet modulate frontal cortices. Together, these two projects expand our understanding of the complexities of basal ganglia circuitry and its interactions with cortex.

Table of Contents

Acknowledgements

Without a doubt I owe a huge debt of gratitude to my advisor, Bernardo Sabatini. His support, guidance, mentorship, and friendship have been essential to this process. It is often joked that a PhD student knows that he's ready to graduate when he hates his advisor, if this is true then surely this thesis is surely premature. His scientific insight is inspirational, I can only hope to one day become the type of scientist that he is. Thank you!

Throughout my PhD, there have been countless people who have helped me personally, professionally, and scientifically and I thank them all. Every member of the Sabatini Lab past and present has been a great asset these last few years. And each is deserving of a paragraph devoted to them. I especially thank Jun Ding, Kevin Takasaki, Helen Bateup, Jess Saulnier, Nic Trisch, and Chris Straub for all their technical, scientific, and life advice for the last few years. To Arpiar Saunders, my scientific twin and collaborator, and to Gil Mandelbaum, who will continue the legacy of *in vivo* recordings in this lab, I thank you. My great appreciation also goes to Mike Higley, who showed me how to first record from an *in vivo* mouse, and started this entire project.

This thesis would not have been possible without the tireless help of our northeastern coops who have trained the mice and turned graduate school into an experience I never expected. Nor would it have been possible without the help of my thesis committee John Assad, Rachel Wilson, John Maunsell, and Bruce Bean. Thank you.

I offer my thanks to the many mice that contributed to this research; while they may not have understood their role they were key to its success. I thank those early scientists who first thought to use rational experimentation to prove a point, Herophilos, Aristotle, and Ibn al-Haytham. I thank early anatomist Andreas Vesalius for inspiring some of the earliest investigations into the brain, and every scientist who has built upon previous knowledge to advance a field. I thank the General Court of the Massachusetts Bay Colony for the original charter of this school.

I am grateful to the many people who have kept me sane outside of the lab: to all the heroic inspirational champions of Woods Hole, but especially Margaret, Frank, Iggy, and Julia. To Sasha and Hugh for our weeknight dinners. To members of my ultimate team KT, Toad, Corey, Gail, Winst, Aaron, and Ginie. And to my college friends Warren, Matt, Jeremey, and Angela.

It is without a doubt that I would not be here if not for the incredible, unprecedented support of my family. My parents, Carl and Mary, have encouraged and inspired me since I was a child. They continue to help with every step of my life, including proofing every document I write (including this very thesis). My sister, Catie, has been a constant source of support, advice, fine wine, and statistical insight and is without a doubt one of the most brilliant people I know. My brothers in law, Taras and Sam have been my great adventuring buddies the last few years since we've been in the same city. Last I thank my grandparents, aunts, uncles, parents-in-law, and cousins for their unending support and encouragement.

Most importantly, to my adorable wife, Sarah, thank you. Your love, help, support, tolerance, and insight have been immeasurably valuable to me. Words cannot begin to express what you mean to me and how much you have helped me. I look forward to all that the future will hold for us.

Last, thanks to my cat Grace, who is always so proud when I come home smelling like mice.

Chapter 1

Introduction:

The basal ganglia (BG) are an interconnected group of nuclei critical to the control of voluntary movements (Graybiel et al. 1994) and are affected in multiple neurological disorders (DeLong 1990; Albin et al. 1989). Classically, the BG, Thalamus, and Motor Cortex are arranged in reentrant loops, where activity from the cortex converges on direct (dSPN) and indirect (iSPN) pathway neurons of the striatum. These SPNs oppositely modulate activity in the output nuclei of the BG, which subsequently inhibits thalamus, which in turn activates motor cortex. The gross anatomy of BG has led to a push-pull model of BG control over motor cortex (Graybiel et al. 1994; DeLong 1990). However, given that the anatomy is fundamentally static, this model lacks ability to predict the activity of these pathways during phases of an animal's behavior. In this thesis we seek to directly address the fundamental tenants of this model by artificially modulating the activity of the two primary classes of striatal neurons, asking how theiractivity changes the firing in motor cortex in the context of a behaving animal.

1.1 Diseases of the Basal Ganglia

The input to the BG, the Striatum, was first described by name (then *corpus striatum*) almost 350 years ago by Thomas Willis (Willis 1664), although as a large distinct brain structure, its presence was probably known since antiquity. Subsequent anatomists identified other nuclei to create a relatively complete depiction of the BG by the middle of the 19th century. Félix Vicq d'Azyr named the output of the basal ganglia the *substantia nigra* in 1786, and Karl Friedrich Burdach used the term *globus pallidus* in 1810 to denote a separate nuclei located adjacent to the striatum (Lee & Shaw 2012). These nuclei would later be realized as the principle targets of the direct and indirect pathway neurons. Interestingly, from the earliest 1664 descriptions of striatum the connection to motor pathology was suspected; Willis noted a relationship between paralysis and striatal abnormalities (Meyer & Hierons 1964).

Today, the role of the BG in movement is well accepted. Many disorders of the BG, such as Parkinson's and Huntington's Disease, are hallmarked by severe motor impairments. Intriguingly, the BG have recently been implicated in other more cognitive diseases, such as obsessive-compulsive disorder, Tourette's disorder, and Schizophrenia, have also become associated as deficits of the BG. Furthermore, many of the so called 'motor diseases' may also have significant cognitive abnormalities that present later or more in more subtle ways as the diseases progress (Sawamoto et al. 2002), indicating that there may be crosstalk between many modalities. Nonetheless, the majority of the research on basal ganglia diseases has focused on the more obvious motor component of the basal ganglia.

Many treatments of BG movement disorders rely on detailed knowledge of the anatomy of the basal ganglia and its connections. Pioneered in the 1940s sterotaxic lesioning of the Globus Pallidus and later parts of thalamus proved to be a useful treatment in Parkinson's disease and tremor (Gildenberg 2006). However the effects of these lesions are often paradoxically at odds with the predicted roles of the nuclei targeted; pallidal lesions expected to increase the number of unintentional movements may in fact decrease with lesion (Marsden & Obeso 1994). More recently stereotaxic lesions have given way to the implantation of Deep Brain Stimulation (DBS) as an effective, and adjustable means of controlling Parkinson's Disease (Bronstein et al. 2011). In addition, DBS has proven effective at treating Dystonia, Tremor, Huntington's Disease (Biolsi et al. 2008; Montgomery 2004), as well as Obsessive Compulsive Disorder (Heimer et al. 2007). However, the exact circuit level effects of DBS remain debatable, with some reports indicating that the principle effect of DBS might be inhibition of a nucleus or even excitation of neighboring fibers of passage (Gradinaru et al. 2009). Furthermore, given that the exact role of each of these nuclei is poorly understood, it has been difficult to design and predict new targets and new stimulation paradigms for DBS. Understanding the output of the BG, especially in the context of behavior, will enable us to better predict the overall function of the BG and allow us to discover what has changed in disease states.

1.2 Architecture of the Basal Ganglia

Classical models of the BG present multiple parallel closed loop pathways, involving different regions and nuclei for different modalities (Haber 2003; Parent & Hazrati 1995). These largely segregated pathways all involve extensive convergent input from many cortical regions onto the striatum, but can output through one of several output nuclei to targets including Thalamus and Superior Colliculus, which complete the loop by synapsing in cortex. In contrast to the Cortex, the predominant neurotransmitter throughout the basal ganglia is GABA; and each nucleus inhibits or disinhibits the ongoing activity of its targets (Chevalier & Deniau 1990).

In the case of the motor system, the motor cortex sends glutamatergic inputs to the BG and is in turn influenced by the BG via their inhibitory output to the thalamus and other nuclei. Convergent excitatory input to the BG from motor cortex and other regions arrive in the dorsal striatum and synapse onto striatal projection neurons (SPNs) (Alexander et al. 1986). These inputs are somatotopically organized, and this organization is preserved throughout downstream nuclei (Nambu 2011; Ebrahimi et al. 1992). Still, convergence between different motor cortices is present in striatum (Takada et al. 1998). The output of striatum consists of two separate classes of GABAergic neurons known as the direct (dSPN) or indirect (iSPN) pathway SPNs. The direct pathway, also known as the striatonigral pathway, projects directly to the Substantia Nigra pars reticulate (SNr) (Gerfen et al. 1990). Whereas, the indirect, or striatopallidal, pathway synapses in the external segment of the Globus Pallidus (GPe). The GPe inhibits the SNr directly and via an intermediary nucleus the Subthalamic Nucleus (STN). Unlike the GPe, and SNr the STN sends excitatory projections, and receives glutamatergic inputs from cortex, in what has been called the hyperdirect pathway (Nambu et al. 2002). The SNr subsequently inhibits several thalamic nuclei including ventrolateral thalamus (VL) and mediodorsal (MD) (Deniau et al. 1978). These nuclei complete the loop via an excitatory projection back to primary motor cortex and striatum. (See **Figure 1.1**)

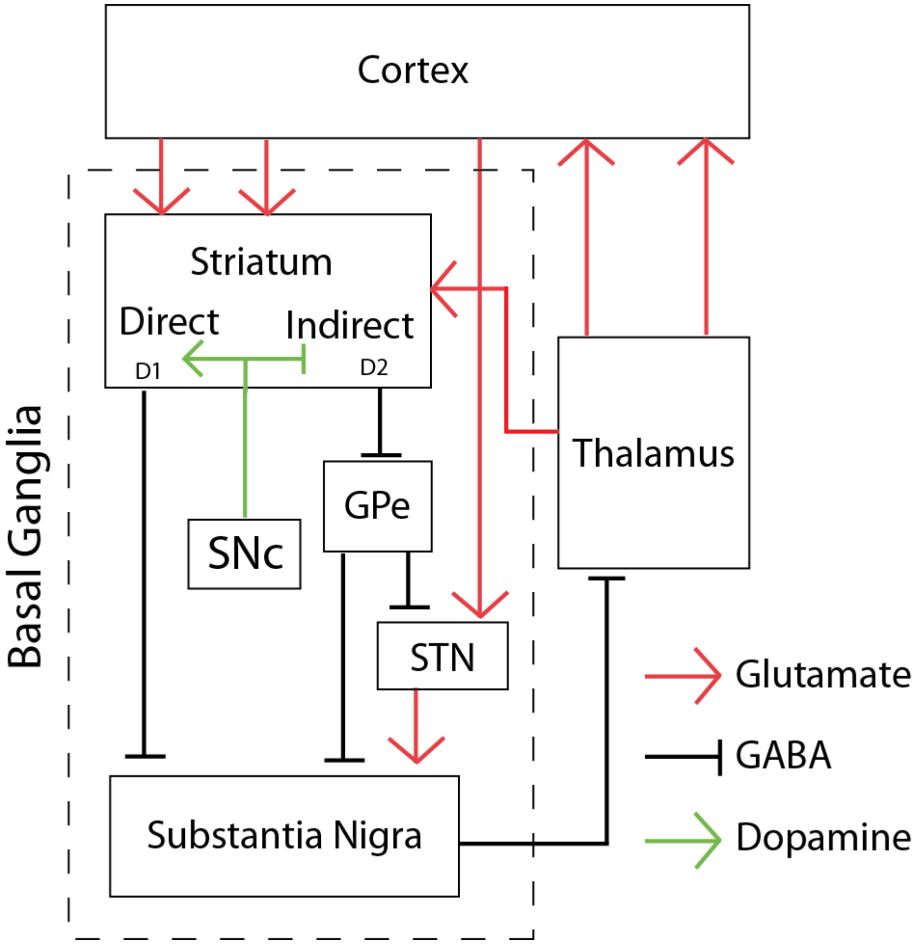

Figure 1.1 Simplified Basal Ganglia Architecture

While the direct and indirect pathways are commonly described as distinct, there are multiple avenues by which the two pathways interact. First, both direct and indirect pathway cells mutually inhibit each other, through reciprocal GABAergic synapses. Next, direct pathway striatonigral, cells have been shown to also send axon collaterals to the GPe (Cazorla et al. 2014; Kawaguchi et al. 1990), although the full importance of this projection remains unclear. And finally, both pathways synapse in the same region of SNr, where individual nigral cells can receive input from both dSPNs and GPe cells (Smith & Bolam 1991).

In addition to the classical cortex-BG-thalamus-cortex loop, there are multiple other loops within the basal ganglia, which are possible given the known connections between these nuclei. Most obvious is the excitatory input from intralaminar thalamic nuclei to the striatum (Smith et al. 2004). However, there also exists reciprocal projections between the GPe and the STN (Graybiel 1990), and back from the GPe to the striatum (Kita & Kitai 1994). Furthermore, the dopaminergic projections from the Substantia Nigra *pars compacta* (SNc) target both classes of striatal projection neurons and receives direct input from the SNr, providing yet another route by which striatal activity could influence itself. To further complicate matters, direct projections from the GPe to the PF of the Thalamus has recently been reported allowing for an additional output of the basal ganglia (Mastro et al. 2014). These multiple loops further confound the interpretation of how this system is expected to behave.

1.3 Cell types and Interneurons of the Striatum

The striatum is the primary input structure to the BG, and will be the target of most of our manipulations in this work. As such it is necessary to briefly explore the cell types that exist in the striatum and how they may interact. The most abundant cell types in the striatum are unequivocally the GABAergic dSPNs and iSPNs, originally called the Medium Spiny Neurons, these projection neurons make up >95% of the neurons in the striatum (Tepper et al. 2004). These neurons principally target other SPNs to cause lateral inhibition (Wilson & Groves 1980). *In vivo* SPNs are thought to fire in a phasic manner engaging in so called up and down states (Stern et al. 1998). Many SPNs fire in response to different parts of movements, cues and actions (Aldridge et al. 1980; Jin et al. 2014). But interestingly, both classes of SPN fire at the beginning of action bouts (Cui et al. 2014). This has lead to the theory that the basal ganglia is responsible for 'Chunking' information and forming habits (Graybiel 1998). Still other models of the functional role of SPNs focus on their role in reward, dopamine from the SNc and ventral tegmental area into striatum is a reward signal (Bayer & Glimcher 2005). Activity of dSPNs and iSPNs is inherently appetitive and aversive (Kravitz et al. 2012), indicating that SPNs may play a crucial role pairing reward information to its context.

No description of the neurons of the striatum would be complete without some reference to the existence of patches. SPNs of both varieties are spatially segregated into functionally distinct compartments known as patches or striasomes, that can be identified by opiate markers (Gerfen 1984). SPNs near the boundaries of patches and the surrounding matrix respect the boundaries of these regions (Dongen et al. 2008). The exact functional role of these regions is not well known.

The second most prominent cell type in the striatum is the Cholinergic Interneuron (CIN), also known as the tonically active neuron in most *in vivo* recording contexts due to its regular firing and easy identification. CINs make up 1-2% of the cells in the striatum. They fire regularly and provide the sole source of Acetylcholine (Ach) to the striatum (Cazorla et al. 2014; Kravitz et al. 2010; Kawaguchi et al. 1990; Marsden 1982; Bateup et al. 2010; Tepper & Bolam 2004; Kreitzer & Berke 2011). Due to their tonic firing, it has been proposed that CINs tonically release Ach in the brain. In fact the striatum has one of the highest concentrations of Ach markers anywhere in the brain (Weiner et al. 1990). Furthermore, CINs pause their firing in response to cues that indicate reward (Kimura et al. 1984). Given the great number of nicotinic and muscarinic acetylcholine receptors on SPNs and incoming glutamatergic fibers (Oldenburg & Ding 2011), as well as their direct release of glutamate onto SPNs (Higley et al. 2011), it is likely that CIN activity is regulating the activity of SPNs in a complicated way. Ach presynaptically inhibit fibers onto SPNs while postsynaptically exciting them (Oldenburg & Ding 2011), thus a pause in their firing could dramatically change striatal circuits. Cholinergic neurons are also located in other adjacent structures, including the Globus Pallidus (Haber et al. 1985), but their role there is less well understood, a topic that will be discussed in the 3rd chapter of this thesis.

Finally there exist several other classes of interneuron, including the fast spiking parvalbumin (PV), the neuropeptide Y (NPY) or Somatostatin expressing cell, and the Calretinin expressing cell (Tepper & Bolam 2004). Each of these classes of neurons make up <1% of the cells in striatum, and very little is known about their function *in vivo*. Each of them interacts with the SPNs and other neurons of the striatum to mediate many additional layers of complexity in the system.

1.4 Classic Model of Basal Ganglia Function

The classic model of the BG and its role in movements was first presented in 1982 (Marsden 1982), but was expanded and clarified throughout the 80s and 90s (Albin et al. 1989; Alexander & Crutcher 1990; Graybiel 1990; Chevalier & Deniau 1990; Parent 1990; DeLong 1990; Parent & Hazrati 1995). Based on the anatomy described above, the model predicts that the direct and indirect pathways are in opposition to each other, each exerting a push-pull effect on movements and cortical activity. Thus, imbalance of these pathways leads to disease states such as in Parkinson's and Huntington's Disease. From this model one would predict that it is the competition between these two pathways, and between the dSPNs and iSPNs themselves, that regulate the decision to move. From there, it is easy to imagine that different microcircuits of the basal ganglia could represent different plans or goals, and that the BG both sorts through these goals to determine an action. However, much of this theory remains untested; it is the purpose of this thesis to directly address the accuracy and completeness of this classic model of Basal Ganglia.

The classic cortex-basal ganglia-thalamus-cortex model was created based on several classes of studies and adapted to fit the observations in disease states. First, numerous anatomical studies, mostly involving single neuron filling and tracing or transynaptic viral tracing, have been used to map out the major connections between the basal ganglia, thalamus, and cortex (Gerfen et al. 1982; Smith & Bolam 1989; Kawaguchi et al. 1990; Kelly & Strick 2004). With knowledge of the neurotransmitters released for each of these projections, the modern looped architecture was formed. Second, the opposing nature of the direct and indirect pathway was first predicted by observations of human patients with lesions to parts of their basal ganglia or diseases such as Parkinson's or Huntington's disease (Marsden 1982). This antagonism between the two pathways has since been supported via genetic and optogenetic studies, which show direct pathway activation having a pro movement effect, whereas indirect pathway activation generally decreases movements (Kravitz et al. 2010; Bateup et al. 2010; Kreitzer & Berke 2011). Lastly, electrophysiological recordings from BG nuclei during optogenetic activation of either pathway has confirmed that iSPNs and dSPNs act in opposition to each other in the SNr despite there a large heterogeneous response (Freeze et al. 2013).

These approaches, however, have lead to certain biases in the models of basal ganglia architecture and function. Namely, that all the models focus on the bulk properties of each pathway and cell type, while remaining indecisive to the effects of small unexpected connections. Single neuron reconstructions can often suffer from low numbers of cells, while bulk tracer injections lack the cell type specificity necessary to parse these circuits. For example, while the existence of crossed projections from the dSPN to the GPe have been known since the time of the first basal ganglia models, yet the role of these neurons is not understood nor typically included in standard models (Cazorla et al. 2014; Kawaguchi et al. 1990). The recent study by Freeze and colleagues furthers this concern, demonstrating that while activation of either dSPNs or iSPNs in bulk has the general effect of inhibiting or disinhibiting the SNr as predicted, there are many cells that behave in the opposite from predicted direction (Freeze et al. 2013). This heterogeneity certainly changes the computation being carried out by the basal ganglia, and should not be overlooked when designing models of its actions.

Finally, many of the fundamental predictions of the existing classical model remain untested. Namely, whether direct and indirect pathway neurons of the striatum affect ongoing firing in cortex, and whether the effects of two pathways remain in an opposition in cortex. In order for these predictions to be true cortex would need to be dynamically and strongly responsive to thalamic input from regions that also receives strong BG input. This BG input would have to be tonically firing, such that it can be bidirectionally modulated by both the direct and the indirect pathway. However, even if these assumptions are correct, this classical model is static, offering no predictions on the time it takes for a basal ganglia modulation to reach the cortex or what effect BG activity has during or leading up to a movement. For these reasons we examined how BG modulates cortical firing rate in an awake behaving animal.

1.5 General Approach

It is our general goal to get a finer understanding of what the role of the direct and the indirect pathway are on the firing rates in cortex. As the basal ganglia is actively engaged in movements it seems only logical to design our study to compare both the role of the basal ganglia during periods that an animal is moving and during periods where the animal is still. As such we have done all of the following studies in the context of an animal that is trained to do a head fixed operant conditioned task.

Cued motor tasks are typical for basal ganglia research, and engage BG circuitry (Haber 2003). In all the following studies, head fixed animals will be tasked to withhold pressing a lever until they hear an auditory cue; then pressing within a certain time window will be rewarded with water. It is not the goal of this study to make any conclusions on the changes to the behavior of the animal. Indeed changes in reaction time or success rate could be attributed to a variety of causes. Instead, by comparing periods where the animal is attempting this task vs. periods where it is not moving, we can compare periods where the basal ganglia is engaged and when it is not. If artificial BG activation has a differential effect during these times, we may be able to ascribe some of those differences to the ongoing activity of BG. Furthermore; it was never the goal of this study to simply be an observational one. That is, from conception we wanted to manipulate the system to see what the results of those manipulations would be, and not merely the correlation between two structures.

For these reasons, we have used virally injected Cre dependent Channel Rhodopsin 2 (ChR2) in a mouse line expressing Cre in either only the iSPN population, or the dSPN population, as has been reported previously (Freeze et al. 2013; Kravitz et al. 2010). These pathways will be stimulated locally while we record activity from one of several brain regions using extracellular multielectrodes. The classic model predicts that there will be some inhibition and disinhibition of cortex, but is unable to predict the context in which this will happen or the style in which changes will occur.

Chapter 2

Antagonistic but not opposite regulation of primary motor cortex by basal ganglia direct and indirect pathways

Ian Antón Oldenburg and Bernardo L. Sabatini

This chapter is based on work that has been submitted for publication.

2.1 Abstract

Motor cortex, basal ganglia (BG), and thalamus are anatomically arranged in a recurrent loop whose activity is hypothesized to be involved in the selection of motor actions. Direct (dSPN) and indirect (iSPN) striatal projection neurons receive excitatory input from cortex, and are thought to oppositely modulate cortical activity via BG output to thalamus. Here, we test the central tenets of this model in head-restrained mice performing an operant conditioning task using optogenetic manipulation of dSPNs and iSPNs to determine the effects of activity in each pathway on primary motor cortex. We find that dSPN and iSPN activation has bidirectional, robust, and rapid effects on motor cortex that are highly context-dependent, with distinct effects of each pathway during quiescent and active periods. Thus, the effects of activity in each pathway are at times antagonist and consistent with classic models, whereas in other behavioral contexts they are suppressed or transiently reversed.

2.2 Introduction

The basal ganglia (BG) are an interconnected group of nuclei critical to the control of voluntary movements (Graybiel et al. 1994) and whose dysfunction contributes to multiple neurological disorders (DeLong 1990; Albin et al. 1989). Many disorders of the BG, such as in Parkinson's and Huntington's diseases, are hallmarked by severe motor impairments. Classical models of the BG present a closed loop architecture in which motor cortex sends glutamatergic inputs to the BG and is in turn influenced by the BG via their inhibitory output to the thalamus. In particular, convergent excitatory input to the BG from motor cortex and other regions arrive in the dorsal striatum and synapse onto striatal projection neurons (SPNs). SPNs comprise the outputs of the striatum and are subdivided into the striatonigral and striatopallidal pathways. The striatopallidal projection is formed by GABAergic indirect pathway SPNs (iSPNs), which inhibit neurons of the external segment of the globus pallidus (GPe) whereas the striatonigral pathway arises from direct pathway SPNs (dSPNs), which inhibit the substantia nigra pars reticulata (SNr)(Gerfen et al. 1990). Although the two pathways are typically described as targeting different downstream nuclei, there are axon collaterals from striatonigral cells in GPe (Cazorla et al. 2014; Kawaguchi et al. 1990). Furthermore, direct and indirect pathway neurons functionally interact in the striatum, via reciprocal GABAergic synapses, and in the SNr where individual neurons receive both dSPN and GPe inputs (Smith & Bolam 1991). The SNr in turn sends GABAergic innervation to the ventrolateral thalamus (VL), which closes the loop via glutamatergic projections back to motor cortex.

This model, in which the BG exert push-pull effects on cortex via inhibition and disinhibition of thalamus (Deniau & Chevalier 1985; Alexander & Crutcher 1990), has emerged from several classes of studies. First, anatomical tracing of axons of individual neurons and transynaptic labeling confirmed the architecture outlined above, and revealed additional interconnections with the subthalamic nucleus, superior colliculus, and other thalamic nuclei (Gerfen et al. 1982; Smith & Bolam 1989; Kawaguchi et al. 1990; Kelly & Strick 2004). The results of these anatomical studies, in conjunction with knowledge of the major neurotransmitters expressed at each projection, were used to build a model of BG circuitry and function. Second and more recently, the behaviorally antagonistic nature of the striatonigral and striatopallidal pathways has been supported via genetic and optogenetic studies, confirming that activity in the former is, at least in terms of open field locomotor activity, generally pro-kinetic and in the latter anti-kinetic (Kravitz et al. 2010; Bateup et al. 2010). Lastly, cell-type specific optogenetics were used to separately activate the physically intermingled dSPN and iSPNs and electrophysiologically confirm antagonistic effects of each pathway on downstream BG nuclei such as SNr (Freeze et al. 2013).

Nevertheless, the final predictions of the model – that BG control motor cortex activity in a closed loop fashion and that striatonigral and striatopallidal projecting neurons exert opposing effects on cortex – remain untested. Furthermore, several assumptions on which this model is built are untested. Firstly, it is assumed that activity in motor cortex is dynamically and strongly influenced by ascending inputs from thalamic regions that are under the inhibitory control of BG. In addition, it assumes that the inhibitory output of the BG is tonic and powerful such that its bidirectional modulation is sufficient to alter action potential firing in downstream circuits. Conversely, it assumes that collateral inhibition within and across SPNs of each pathway is insufficient to suppress the predicted effects of activation of each pathway in isolation. Lastly, the classic model is static, differences in how the BG influence the cortex during different behavioral states is unknown.

To address these unknowns we functionally tested the underpinnings and predictions of the classic model of BG in awake, behaving mice. Mice were trained to perform a simple operant conditioning task, and the effects of optogenetic manipulations of dSPN or iSPN activation on primary motor cortex were evaluated. Our results support the classic opponency model of the BG such that the striatopallidal pathway suppresses trained movements and basal activity in primary motor cortex whereas the striatonigral pathway has converse effects. Both pathways exert large and powerful effects on cortex with approximately two-fold alterations in cortical firing rates revealed within ~150 ms of optogenetic manipulations in striatum. Although antagonistic effects of dSPN and iSPN activation dominate at the population and behavioral levels, individual cells in cortex show more complex responses to manipulation of striatal activity such that groups of neurons located in superficial layers of primary motor cortex display transient increases in firing in response to iSPN activation. Furthermore the effects of dSPN activation on cortex depend heavily on behavioral state such that, even in neurons whose baseline firing rate is strongly modulated, activity around movements and behaviorally relevant sensory cues are unaffected.

2.3 Results

2.3.1 Head-fixed operant conditioning

Studies of circuit interactions between the striatum and motor cortex require electrophysiological analysis in awake, behaving animals since striatal activity is minimal under anesthesia and the neuromodulatory state of the structure depends crucially on behavioral context (Mahon et al. 2006; Spampinato et al. 1986). Therefore, mice were trained in an operant conditioning task in which a motor action carried out in short latency following an auditory cue led to a water reward. The task was designed (see below) to include periods of enforced no movements, cued movements for reward, and spontaneous movements, allowing analysis of circuit interactions during different classes of motor actions.

Animals were habituated to sit in a plastic tube that supported their weight while restrained by a surgically implanted titanium headpost (see methods). Mice had access to a water delivery spout which could be licked for reward as well as to a lever within reach of the left forepaw (adapted from (Histed et al. 2012)). All depressions and releases of the lever were recorded by a microswitch positioned at the fulcrum. The cue consisted of a 50 ms 10 kHz tone delivered from a speaker located approximately 10 cm from the animal. Four mice were trained simultaneously with each apparatus placed in a separate sound-attenuating box.

Animals were trained using an adaptive program that dynamically altered the difficulty of the task based on individual in-session performance (see methods) (**Figure. 2.1a**). After reaching benchmarks with the adaptive program (usually after 14 training days), mice were switched to a static program with fewer adjustable parameters (**Figure 2.1b**). A large fraction of mice became proficient at the task, with short (<1.5s) reaction times and earning rewards in a high fraction of trials (**Figure 2.1c**).

The duration of training varied considerably but 2-3 weeks were generally required to reach proficiency (>125 rewards in 90 min) (**Figure 2.1d**). Proficient mice were moved to an electrophysiology rig with nearly identical layout to the training rigs for subsequent analysis.

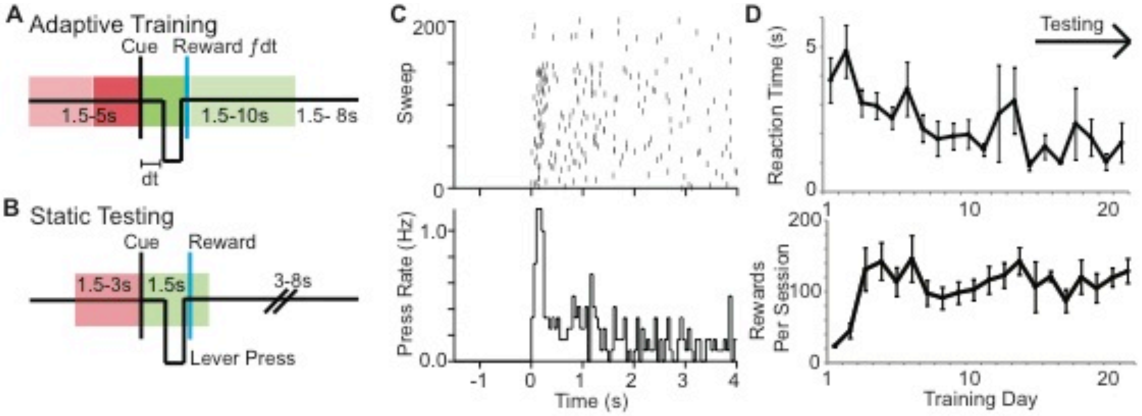

Figure 2.1. Operant conditioning task structure and performance.

(A) Schematic of the training and testing task designs. After the start of the task, if the mouse refrains from pressing a lever for a variable length period ($T_{nopress}$=1.5-5 s, red), then a 10 kHz tone is played ("cue"). Following the cue is a reward period (T_{reward}=1.5-10 s, green) in which the animal receives a water drop if it presses and releases the lever. During training the duration $T_{nopress}$ and T_{reward} are progressively and dynamically adjusted based on the animals performance to shape its behavior and reaction times. Throughout training $T_{nopress}$ is randomly varied to prevent an interval timing strategy, while ΔT_{reward} is reduced to keep the task challenging for the animal. Furthermore, the volume of water per reward (V) is proportional to reaction time ($\Delta T_{reaction}$, measured from the end of the tone to the level release) such that V= 8 µl, if $\Delta T_{reaction}$ < 200 ms , linear decreases to 4µl up to $\Delta T_{reaction}$=1s, and further linearly decreases to 2µl at the maximally allowed $\Delta T_{reaction}$.

(B) For behavioral testing and recordings sessions, a static version of the task is used in which $T_{nopress}$ is randomly chosen from 1.5-3 s, $\Delta T_{reaction}$=1.5 s, V= 4 µl.

(C) Raster plot (*top*) and summary histogram (*bottom*) of lever presses times relative to the tone (t=0) for a single testing session of a well-trained animal.

(D) Summary (n=8 mice) of the behavioral metrics during training of the mice used for recordings, showing that mice improve on this task over 2 to 3 weeks. Reaction time (*top*) is the mean time from tone to first lever press after the tone including those that fall outside of the reward window. Rewards per session *(bottom*) the number of rewards received in each 90 min session. Animals reached criterion levels for testing and recording typically after 14-21 days. Note that the switch to the static variant of the task usually occurs around training day 14.

2.3.2 Optogenetic manipulation of dSPNs and iSPNs

To gain optical control of each pathway, transgenic mice expressing Cre recombinase in either indirect pathway iSPNs (*Adora-2A-Cre*) or direct pathway dSPNs (*Drd1a-Cre*) were injected with 500 nl Adeno Associated Virus (AAV) encoding Cre-dependent Channelrhodopsin (ChR2) tagged with mCherry (AAV 2/5-DIO-CR-mCherry). The injection was performed one week prior to the beginning of training and during the same surgery at which animals were fitted with a titanium headpost. The injection was directed to coordinates for striatum, resulting in transduction of neurons throughout the striatum, with little or no infection in overlying cortex. Fluorescently labeled projections from dSPNs or iSPNs reached the expected targets of SNr and GPe, respectively (**Figure 2.2a**). In a subsequent surgery, a multimode fiber optic was chronically implanted in the dorsal striatum to stably illuminate the site of infection.

In order to assess the effectiveness of optogenetic stimulation, in a subset of experiments a 16-channel extracellular recording electrode was placed in striatum while the animal performed the task. The recording electrode was either targeted to the field of illumination of the chronic fiber optic, or, when that was difficult due to space constraints, fitted with a fiber to form an optrode and lowered into the infected region. In both cases striatal units were identified and modulated by ChR2 activation with blue light (**Figure 2.2b**). The degree of modulation of each unit by optogenetic activation in the striatum was calculated as:

$$I_{ChR2} = \frac{f_{on} - f_{off}}{f_{on} + f_{off}}$$

with f_{on} and f_{off} corresponding the average firing rates of individual units with the laser on or off, respectively, calculated during the 1.5 s baseline period with no movements before the delivery of the conditioned cue.

Figure 2.2. Channelrhodopsin (ChR2) mediated modulation of striatal projection neurons and behavior

A, Saggital brain slices showing ChR2 expression (red) following injection of Cre-dependent ChR2-mCherry encoding AAV in mice that express Cre in iSPNs (iSPN-ChR2, left) or dSPNs (dSPN-ChR2, right). Images were consistent with histology from all recorded animals (n=7 ISPN-ChR2, N=8 dSPN-ChR2).

B, Example raster plots and histograms of putative ChR2-expressing SPNs units from iSPN-ChR2 (left) and dSPN-ChR2 (right) animals. Blue indicates period of 473nm light illumination.

C, Histogram of indices of modulation of firing rate (I_{ChR2}) of separated units by ChR2 activation. I_{ChR2} is the difference in the baseline firing rate between light on and off divided by the sum of those firing rates. Baseline firing was measured during the period up to 1.5s before the tone during which no movements are detected. Red bars indicate units that were statistically significantly modulated by light (T-Test, $p<0.05$, iSPN 35/76 units across 3 animals; dSPN 57/98 units across 3 animals). The population of striatal units do not demonstrate consistent change in firing rates to iSPN activation although many cells change their firing rates, average index -0.06 ($p>0.05$ Wilcoxon Signed Rank Test, n=76 units, N=3 Animals, left), but do to dSPN activation, average index 0.31 ($p<0.0001$ Wilcoxon Signed Rank Test, n=98 units, 3 Animals, right).

D, Summary of changes in behavioral metrics resulting from ChR2-activation light stimulated trials. iSPN-ChR2 animals (N=7 animals), dSPN-ChR2 (N=8 animals), or ChR2-negative control animals (N=3 animals) were scored for changes in rate of presses (far left), duration the lever was held down (left), Reaction time for a rewarded trial (right), and percentage of trials that were rewarded (far right) as a ratio of performance in baseline conditions and with blue light stimulation (* indicates $P<0.05$ Wilcoxon Signed Rank Test, Theoretical Median 1.0 no change).

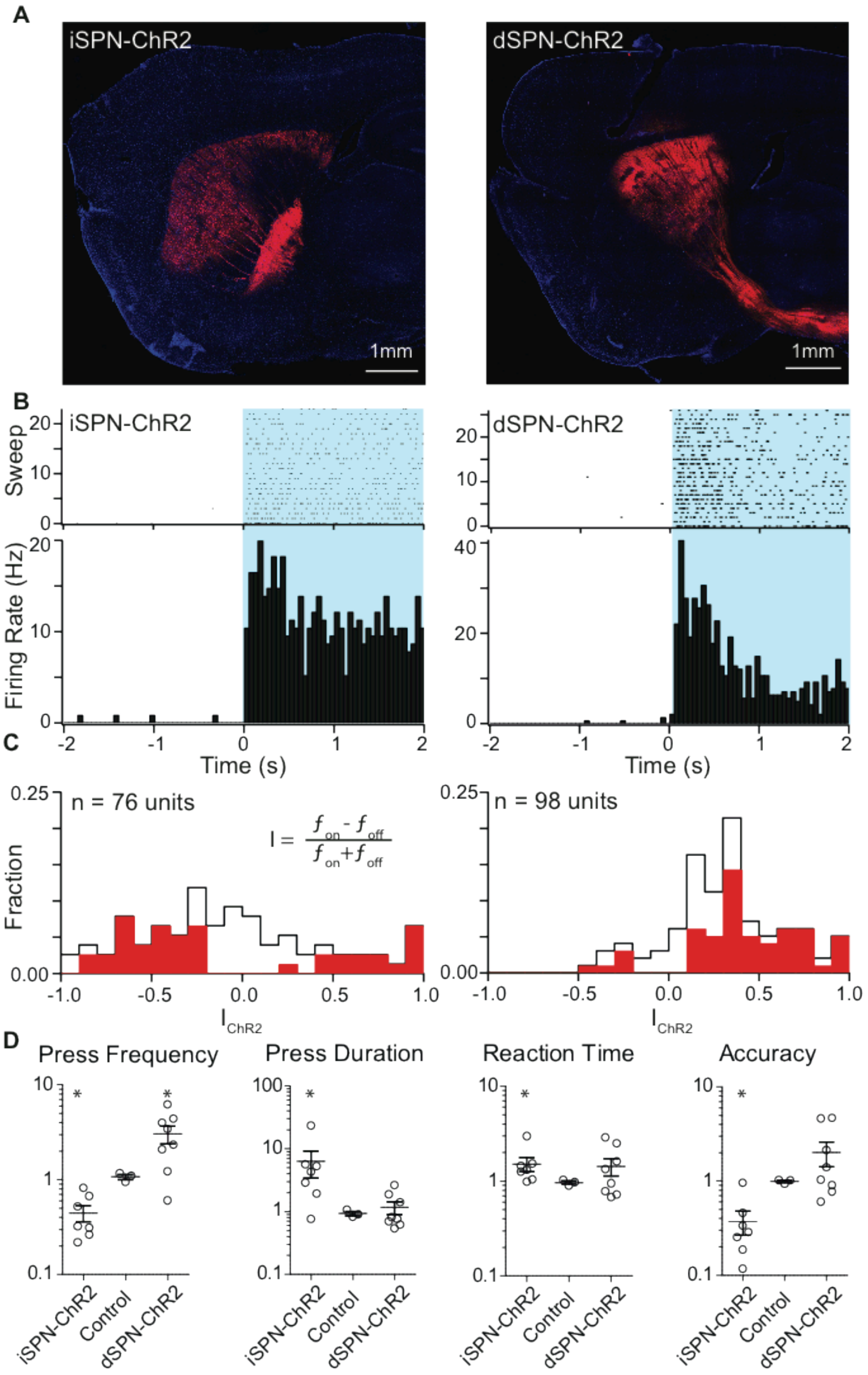

Figure 2.2 (continued): Channelrhodopsin (ChR2) mediated modulation of striatal projection neurons and behavior

Activation of iSPNs or dSPNs modulated activity in striatum over a broad range with individual neurons showing suppression or enhancement and I_{ChR2} distributed over much of its -1 to 1 dynamic range. In each condition, approximately 10% of units had $I_{ChR2}>0.75$, corresponding to a 7-fold increase in action potential firing rate (7/76 iSPN units, 9/98 dSPN units). These units had low basal firing rates prior to the optogenetic stimulus (average Hz 0.32± 0.10 dSPN, 0.49±0.13 iSPN, $p>0.2$ Mann Whitney Test between pathways), and robustly responded to light within 50 ms (**Sup Figure 2.1**); thus, these neurons likely represent ChR2-expressing neurons that were directly stimulated. Overall, optogenetic stimulation increased the firing rate of ~40% (30/76 units) and 86% (85/98 units) of striatal units when activating iSPNs and dSPNs, respectively, presumably through a combination of direct activation and network effects. Furthermore, in both sets of experiments neurons also were identified in the striatum that were inhibited by light. Such inhibition could results from SPN to SPN GABAergic synapses, which exist among and across neurons of each pathway (Wilson & Groves 1980; Kozorovitskiy et al. 2012) as well as from long-range circuit effects. Inhibition was rare following activation of dSPN (4 of 98 units showed significant reductions) and more common following iSPN activation (27 of 76 units) (**Figure 2.2c, Sup Figure 2.1**).

Two possible effects could contribute to the differences in the fractions of activation and suppressed units seen with stimulation of iSPNs and dSPNs. First, collateral synapses are more commonly formed and are stronger when the presynaptic partner is an iSPN (Taverna et al. 2008). Second, the prediction of the classic model of BG function is that iSPN activation should lead to net reductions in excitatory drive to striatum, thereby further reducing activity in this structure, whereas dSPN activation should lead to net increased excitation of striatum.

2.3.3 Behavioral effects of pathway stimulation:

To determine the behavioral effects of iSPN or dSPN activation, we stimulated each pathway through the chronically implanted fiber (see methods) on alternating trials using 1.5-3 mW of 473 nm light. Similar protocols have been used previously to manipulate SPN activity in awake mice (Kravitz et al. 2010). iSPN activation reduced and dSPN activation increased the frequency of lever presses (**Figure 2.2d**; ratio of press frequency with ChR2 activation to control trials: iSPN 0.45±0.09 N=7 mice, dSPN 3.1±0.66 N=8 mice; $p<0.05$ Wilcoxon Signed Rank Test for each) whereas uninfected control mice showed no modulation (1.1±0.06 N=3 mice, n.s. Wilcoxon Signed Rank Test). Reaction time (in trials where the animal received a reward) was lengthened by either iSPN or dSPN activation (Ratio of reaction time: 1.5±0.25 iSPN, $p<0.05$; 1.4±0.30 dSPN, n.s.; 0.97±0.04 uninfected, n.s.; Wilcoxon Signed Rank Test). In addition, press duration was increased via iSPN activation but unaffected by blue light in control or dSPN infected mice (iSPN 6.3±2.9 $p<0.05$, dSPN 1.2±0.27 n.s., control 0.93±0.07 n.s. Wilcoxon signed rank test), indicating delayed and slowed kinetics of even highly trained reward-reinforced movements with iSPN activation. Finally, overall accuracy (rewards per tone with and without pathway stimulation) was reduced by iSPN activation and enhanced via dSPN activation (Ratio of accuracy: iSPN 0.37±0.10 $p<0.05$, dSPN 2.0±0.60 n.s., control 0.99±0.030 n.s, Wilcoxon signed rank test).

2.3.4 Effects of dSPN and iSPN activation on motor cortex in quiescent animals

To study the effects of striatal activity on cortical function we inserted multielectrode arrays in the forepaw region of primary motor cortex (M1) contralateral to the lever and ipsilateral to the chronic fiber located in striatum (**Sup Figure 2.2a**). The stereotaxic location of forepaw M1 (0.25 anterior, 1.5 lateral from bregma) was confirmed in advance via microstimulation in anesthetized mice, which reliably produced twitches in the forepaw in 4 out of 5 animals, in agreement with previous reports (Tennant et al. 2011) (**Sup Figure 2.2b**). Furthermore, ongoing activity in this area is acutely necessary to carry out the trained task as focal pharmacological inactivation via injection of GABA (50 nl, 100 mM) in this region transiently impaired performance (for 140s to >1000s, in 2 animals) (**Sup Figure 2.2c**).

Classic models postulate that activity of primary motor cortex is up- and down-regulated by BG-mediated disinhibition and inhibition of ascending thalamocortical projections. In this model, the thalamus is tonically inhibited by the SNr which itself can be inhibited by dSPN input (thereby disinhibiting thalamus) or disinhibited by iSPN effects in GPe (thereby further inhibiting thalamus). Two inherent assumptions in this model are that ongoing thalamocortical activity accounts for a significant fraction of cortical excitation and that increasing SNr activity inhibits the thalamic projection neurons responsible for this drive.

To determine if increasing iSPN firing modulates ongoing activity of primary motor cortex, iSPNs were stimulated via ChR2 during quiescent periods in which the mice made no movements and received no auditory stimulus or reward. Consistent with classical models, activation of iSPNs strongly reduced the average firing rate of many cortical units in this baseline period (**Figure 2.3a-d**): of 193 units recorded from 4 animals, the firing rates of 136 units were significantly changed (132/193 inhibited, 4/193 excited, each significant unit $p<0.05$ 2-tailed t-test on alternating trials). The population firing rate was reduced significantly with an average modulation index of -0.31 corresponding to ~47% decrease (**Figure 2.3b**; $p<0.0001$ n=193 units, Wilcoxon Matched pairs signed rank test). These results indicate that activation of iSPNs, which have no direct output to cortex, reduce cortical firing rates, presumably by reducing thalamocortical drive.

Figure 2.3. Antagonist modulation of primary motor cortex by direct and indirect pathways.

A, iSPN activation decreases (left) and dSPN activation increases (right) firing rates in motor cortex. Example raster plots (top) and histograms of activity (bottom) of isolated cortical units in control conditions and during optogenetic activation in striatum (blue).

B, Indices of modulation (I_{ChR2}) of firing rates cortical units for iSPN or dSPN optogenetic activations. Indices were calculated based on the firing rates during the 1.5s period before the tone in which no movements were detected (as in **Fig 2.2C**). Red bars indicate units that were statistically significantly modulated by light (iSPN: 136/193 units across 4 animals; dSPN: 103/136 units across 4 animals; t-test, $p<0.05$). As a population cortical units were also significantly modulated by each optogenetic manipulation ($p<0.01$, Wilcoxon signed rank).

C, Mean firing rate across all cortical neurons for the period around the on (*left*) and off (*right*) light transitions. Gray bars are ± SEM.

D, Pseudocolored plot of changes in firing rate of all units normalized to the baseline period and ordered by light modulation index (low to high). Blues and purples represent low firing rates whereas yellow and red represent high firing rate.

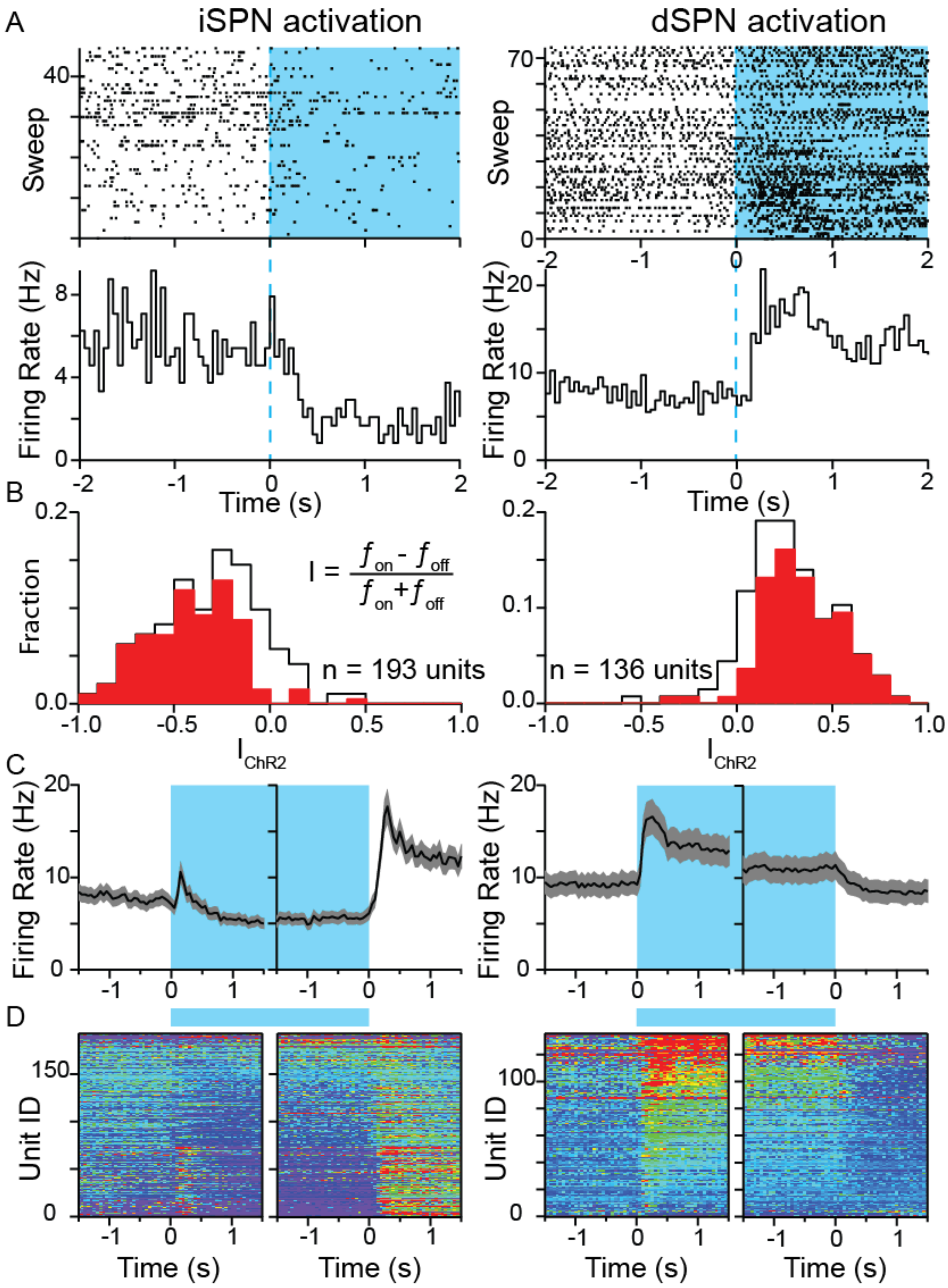

Figure 2.3 (continued): Antagonist modulation of primary motor cortex by direct and indirect pathways.

To test if the BG exert tonic inhibition on cortical activity via inhibition in thalamus, we examined the effects of disinhibiting thalamus via activation of dSPNs during quiescent periods as above. The average basal firing rate in motor cortex in these experiments and transgenic mice was the same as for iSPN manipulations above (iSPN 9.6±0.99 Hz, dSPN 9.0±1.3 Hz, n.s. Mann Whitney). In response to optogenetic activation of dSPNs a large portion of cortical units were significantly modulated (Figure 2.3a-d): of 136 units from 4 mice, 103 significantly changed their firing rates (100/136 excited, 3/136 inhibited, p<0.05 2 tailed t-test on alternating trials). The population firing rate was significantly increased with an average modulation index of 0.28 (Figure 2.3b; P<0.0001 n=136 units, Wilcoxon Matched Pairs signed rank test) corresponding at an ~80% increase

2.3.5 Kinetics of striatal modulation of cortex

Modulation of cortex by changes in iSPN and dSPN activity requires inhibition and disinhibition in a polysynaptic circuit. Furthermore, interactions within the BG and from the BG to thalamus are mediated by spontaneously active GABAergic projection neurons. Therefore, increasing the activity of a downstream structure occurs via relief of tonic inhibition, a process whose kinetics is inherently limited by the moderate firing rates of the projection neurons. In order to determine the delay from alterations in striatal activity to modulation of cortex, we measured the latency for significant alterations in activity of highly modulated cortical units following light transitions in the striatum (**Figure 2.3d and Sup Figure 2.4**). The time for significant modulation of each unit varied considerably but was on average fast (dSPN 123 ± 7ms; iSPN 169 ± 21). Thus, despite lack of a direct output from striatum to cortex, the effects of dSPN and iSPN activation on cortex are both large and rapid with approximately 2-fold effects engaged within ~200 ms. This indicates that ascending thalamic inputs to cortex provide a basal drive that underlies cortical activity and can be rapidly inhibited or disinhibited by striatal output.

Immediately following ChR2-activation of iSPNs the average cortical population activity increased briefly before decreasing (**Figure 2.3c**). Inspection of activities of individual units revealed that this was due to a large, transient increase in firing rates in a subset of cortical units whose activity was altered as quickly (140 ± 11 ms) following iSPN activation as that of the inhibited neurons. To quantify this effect and separate the transiently up-regulated units, we calculated a modulation index I_{early} comparing the action potential firing rates 0.5 s before and after laser activation. Units with I_{early} >0.1 were examined separately from those with I_{early} <-0.1 (**Figure 2.4a**). Units with a positive I_{early} displayed a strong excitatory response to the offset of light and were found in nearly all recording sessions (**Figure 2.4a**, **Sup Figure 3a**). Furthermore, across the population the values of I_{early} and I_{ChR2} for each unit were anti-correlated (**Sup Figure 2.3b**). Interestingly, units with I_{early} > 0.1 displayed similar behavior at the light-on and light-off transitions – units with transient activation at light-on were also transiently activated at light-off. Nevertheless, the long-term effect of iSPN activation on these units fit the classic model with decreases and increases in activity at long-times (> 500 ms) after the transitions to laser on and off, respectively.

Units with positive I_{early} were found at significantly shallower recording sites than those with negative I_{early} (I_{early} > 0.1: 579 ± 29 µm, I_{early} <-0.1: 874 ± 40 µm. $p<0.0001$, Mann Whitney test. **Figure 2.4a**). Conversely, separate calculation of average I_{early} for units at shallow (100-750µm) vs. deep (>750µm) recording locations results in I_{early} = 0.19 and -0.12, indicating that transient activation following iSPN stimulation was more likely for superficial cortical units than for those in deeper layers. Whereas a difference in I_{early} was readily apparent as a function of depth following iSPN activation, no evidence of different populations was observed with dSPN activation at either the laser on or off transitions (**Figure 2.4c,f; Sup Figure 2.3d-f**). This non-canonical effect of iSPN modulation cannot easily be explained via lateral inhibition between pathways due to its transient nature and symmetric light-on and light-off behavior.

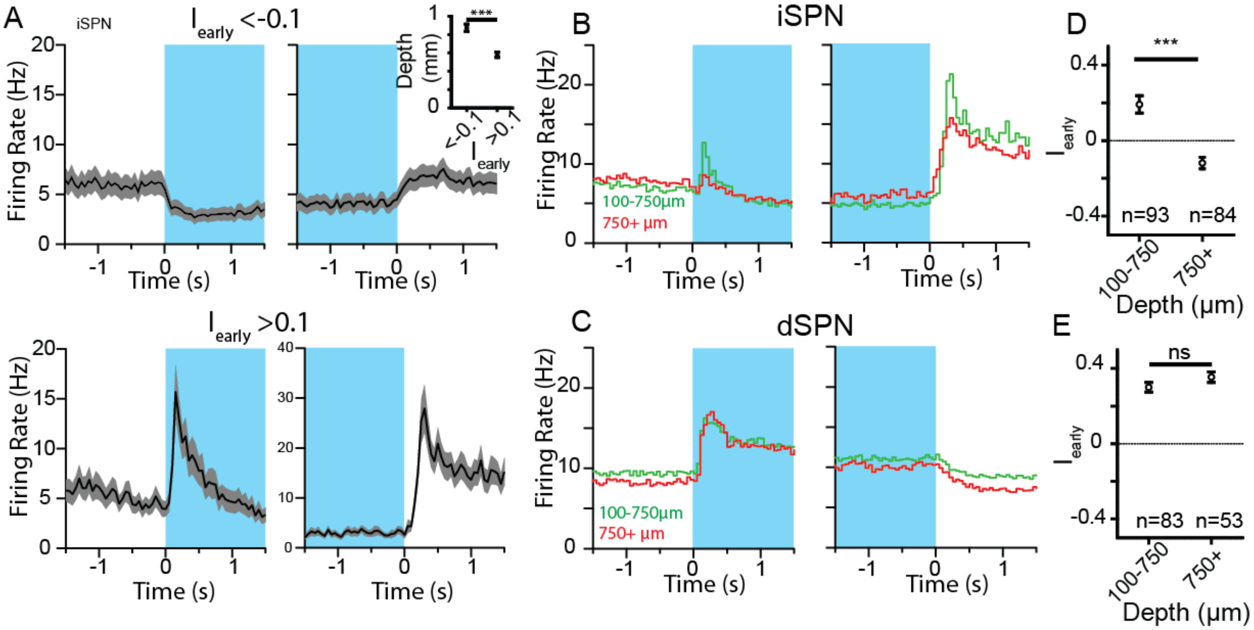

Figure 2.4. Depth of Units with positive I_{early} in Direct and Indirect pathway.

A, iSPN activation (blue bar) inhibits some units (top) and transiently excites others (bottom). Those units that showed transient excitation (I_{early} >0.1) were located shallower than those that did not show excitation (inset) (I_{early} >0.1: 579 ± 29 µm n=59 units, I_{early} <-0.1: 874 ± 40 µm n=63 units. p<0.0001, Mann Whitney test).

B-C, Transient excitation by iSPN is more prominent in shallow units (green), than deep units (red), but no depth-based differences in response dSPN activation were observed.

D-E, Mean I_{early} by depth is significantly different with iSPN activation (100-750µm 0.19 ± 0.05 vs >750µm -0.12 ± 0.03; p<0.0001, Mann Whitney Test) but not changed by dSPN activation (100-750µm 0.30 ± 0.03 vs >750µm 0.35 ± 0.03; n.s. Mann Whitney Test).

2.3.6 State dependent effects of dSPN and iSPN activation on motor cortex

In order to determine the effects of striatal activity on motor cortex during movements, we examined cortical activity around lever presses carried out in response to the auditory cue for reward or initiated spontaneously. In all mice there was significant activation of cortical units around movements and cues. We separately considered three periods: 1, failure trials in which the animal failed to press the lever within the allotted reward time and with activity aligned across trials by the time of the tone onset; 2, success trials as in (1) in which the mouse made the movement in the allotted time; 3, spontaneous movements in which the animal pressed the lever outside of the 1.5s reward window, thus in a time well separated from tones or rewards and aligned across trials to the time of the lever depression.

Indirect pathway activation reduced the firing rate of units during the 0.5s around a spontaneous press (3) or after a failure trial (2), (**Figure 2.5a,c**, P<0.0001 Wilcoxon matched-pairs signed rank test). The degree of inhibition was weaker at spontaneous presses than during the baseline inhibition (I_{ChR2} = -0.31±0.02 vs. $I_{ChR2\ during\ press}$ = -0.06±0.02, p<0.0001, KW statistic: 512.7, Kruskal-Wallis test with Dunn's Multiple Comparison; 132/193 units inhibited baseline vs. 47/193 units inhibited during movement), but unchanged during failure trials ($I_{ChR2\ during\ failure\ trial}$ = -0.24±0.02, p>0.05, Kruskal-Wallis Test with Dunn's Multiple Comparison, 132/192 units inhibited baseline vs. 118/193 units inhibited during cue) (**Sup Figure 2.5a**).

Unlike the indirect pathway and in striking difference to the quiescent state, direct pathway activation had no effect on firing rates during spontaneous presses and fail trials (**Figure 2.5b,d, Sup Figure 2.5b**, - $I_{ChR2\ during\ press}$ = 0.02±0.02, $I_{ChR2\ during\ failure\ trial}$ = 0.00±0.02 light index during fail trial, n=136 units. p>0.05. Wilcoxon matched-pairs signed rank test). The lack of elevated firing rates was not due to a ceiling effect as the firing rates during failure trials, with or without light, were significantly less than those during spontaneous presses and success trials (**Figure 2.5d**; failure trial 14.8±1.8 Hz press 22.6±2.4 Hz, p<0.0001 Wilcoxon matched-pairs signed rank test).

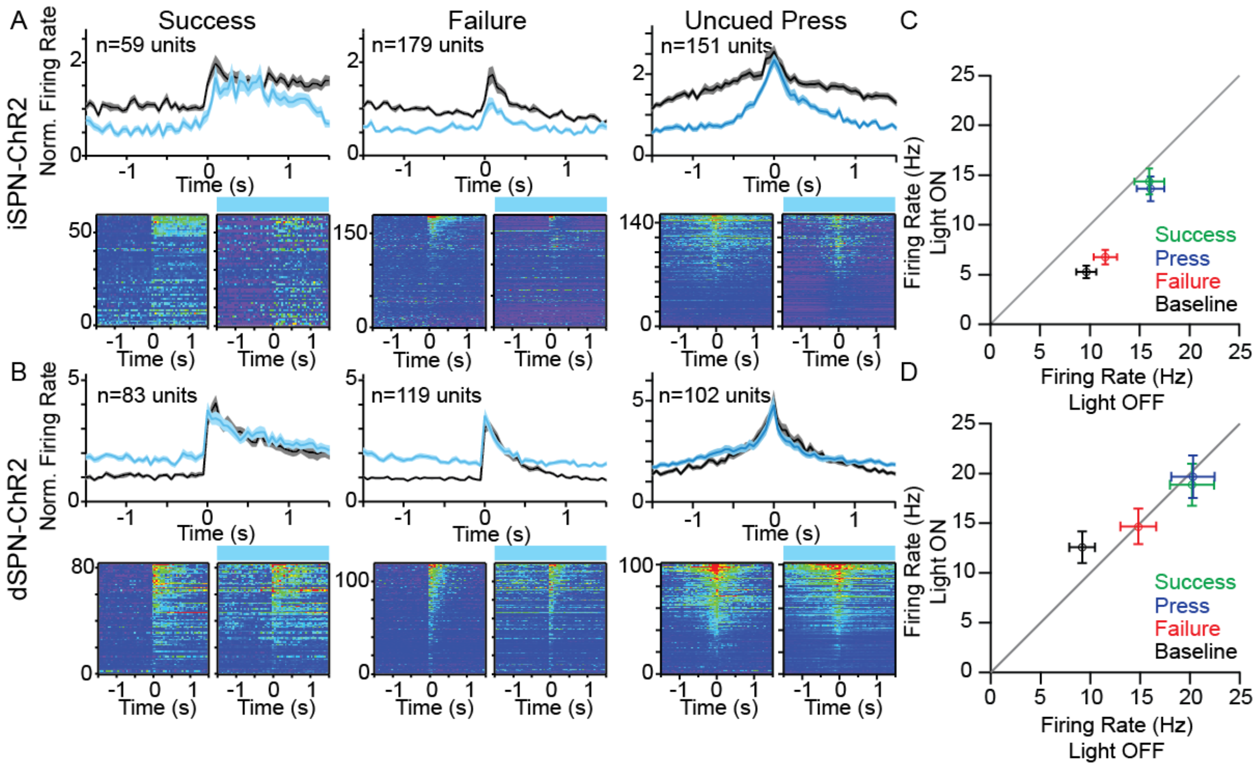

Figure 2.5. Differential effects of striatal activation across behavioral epochs.

A-B, Normalized average firing rates of cortical units (*top*) aligned to either the tone (t=0) for trials in which the mouse did (Success) or did not (Failure) press the lever during the rewarded interval or to the down lever press (Uncued Press) for spontaneous lever presses outside of the task period. The firing rate of each neuron was normalized to that in the baseline period (1.5s prior to a tone). Units were rejected for analysis if there were less than 30 spikes in the baseline periods for that class of event (presses, success tones, or failure tones). Trials with optogenetic activation of iSPNs (A) or dSPNs (B) are in blue and trials without activation are in gray. Shaded regions display the ± SEM. *bottom,* Individual units' normalized firing rate presented as a pseudocolored plot and ordered by the press or tone modulation index (low to high), without (left) or with (right) optogenetic activation.

C-D, Firing rates of all units during the 1.5s baseline period, the +/-250ms around a press, or the 0.5s after a Tone (failure or success), with (y-axis) and without (x-axis) iSPN (C) or dSPN (D) optoactivation are plotted. Error bars indicate +/- SEM. iSPN activation (C) decreased firing rates during the 1.5s baseline (9.62±1.0 Hz Off to 5.51±0.62 Hz On, n=193, P<0.0001 Wilcoxon matched pairs signed rank test), 0.5s after a success trial (15.96±1.5 Hz Off to 14.35±1.3 Hz On, n=153, P<0.01 Wilcoxon matched pairs signed rank test), 0.5s after a failure trial (11.53±1.2 Hz Off to 6.77±0.72 Hz, n=193, P<0.0001 Wilcoxon matched pairs signed rank test), and the 0.5s around an uncued press (16.09±1.4Hz Off to 13.64±1.2 Hz On, n=179 P<0.0001 Wilcoxon matched pairs signed rank test). dSPN activation did not increase firing rates 0.5s after success trials (20.21±2.2Hz Off to 18.86±2.130Hz on, n=136, p=0.011 Wilcoxon matched-pairs signed rank test), 0.5s after a failure trial (14.81±1.8Hz Off to 14.68±1.8Hz On, n=136, p>0.05 Wilcoxon matched-pairs signed rank test), and 0.5s around an uncued press (20.30±2.2Hz Off to 19.67±2.1Hz On, n=136, p>0.05 Wilcoxon matched-pairs signed rank test) but did increase the 1.5s baseline period (9.03±1.3Hz Off to 12.73±1.6Hz On, n=136, p<0.0001 Wilcoxon matched-pairs signed rank test).

To test if this difference in the population level response of motor cortex to activation of iSPNs and dSPNs is also reflected in the activity of individual neurons, we calculated a firing rate modulation index for each unit for each behavioral epoch. A spontaneous lever press firing rate modulation index (I_{press}) was calculated as:

$$I_{Press} = \frac{f_{press} - f_{baseline}}{f_{press} + f_{baseline}}$$

with f_{press} being the average firing rate in a ±0.5 sec interval around the press and $f_{baseline}$ the average firing rate in the quiescent period. As above, this index ranged between -1 and +1 indicating, respectively, all activity in the baseline state and all activity in the peri-press period. A value of 0 indicates no change in average firing rate at the time of spontaneous presses. Similar I_{fail} and $I_{success}$ indices were calculated for the activity in failure and success trials, comparing the baseline activity to that in 0.5s period after the tone (I_{fail} = 0.04 ± 0.02 iSPN, $I_{success}$ = 0.22 ± 0.02 iSPN; I_{fail} = 0.32 ± 0.02 dSPN $I_{success}$ = 0.32 ± 0.02 dSPN; all significantly greater than no change (index =0), $p<0.05$ Mann Whitney). As expected in primary motor cortex, individual units were strongly modulated during spontaneous presses, with most units increasing activity (average I_{press}=0.31±0.02 iSPN, I_{press}= 0.45± 0.03 dSPN; **Sup Figure 2.5c**).

The effects of optogenetic activation of dSPNs and iSPNs on the activity patterns of individual units in motor cortex are complex. In the simplest interpretation, the motor characterof individual units is unaffected by manipulation of each pathway in the striatum as in both sets of experiments there was a high degree of correlation of I_{press} measured without and with BG activation (**Figure 2.6a**) (Spearman's coefficient: 0.49 iSPN, 0.83 dSPN, $p<0.0001$). Thus, units that showed significant changes in activity at the time of spontaneous presses without optogenetic stimulation continued to do so during the stimulation. Furthermore, I_{press} of individual units was generally increased by activation of iSPN and decreased by activation of dSPN, an effect that was also clear at the population level (**Sup Figure 2.5c-d**).

Such changes suggest that the ability of an ideal observer to predict the onset of a spontaneous movement based on the activity of primary motor cortex should be enhanced by activation of iSPNs and degraded by activation of dSPNs, an effect not readily predicted by classic models of BG-cortex interactions. Indeed a simple population spike count threshold model revealed such effects when analyzed by receiver-operator characteristics (ROC). In this model presses are generated at periods of high population firing above a threshold (**Figure 2.6b**, see Methods) with no time dependence. Thus, the total spike count in each time bin is analyzed independently without hysteresis or refractory periods. In the basal state, this model generated good predictions of movement onset with area under the curve (AUC) values of 0.83 ± 0.02 for iSPN-ChR2 recordings and 0.90 ± 0.03 for dSPN-ChR2 recordings. As predicted above, upon optogenetic activation of iSPNs AUC increased in nearly every recording (to 0.92 ± 0.01 with iSPN activation n=11 recordings, p<0.01 Wilcoxon matched pairs signed rank test). Conversely, upon dSPN activation AUC decreased in every recording (to 0.81 ± 0.04 with dSPN activation, n=9 recordings, p<0.001, Wilcoxon matched pairs signed rank test; **Figure 2.6c-d**).

Given the observed changes in the firing properties in motor cortex, we examined the possibility that BG exert selective control over certain functionally relevant cells in motor cortex. We compared modulation of firing by press (I_{press}) to that unit's modulation by BG activation (I_{ChR2}). We find that the degree of modulation of each unit by activation of the iSPNs was not predictive of the degree of modulation of the unit by spontaneous movements – I_{press} and I_{ChR2} showed no correlation (**Figure 2.7a,** Spearman's Coef: -0.003 n.s.). In contrast, activation of dSPNs increased the basal activity of neurons in primary motor cortex that were more active at the time of the press. The relationship between I_{press} and I_{ChR2} for activation of dSPNs displayed remarkable correlation with R=0.71 (**Figure 2.7b**, p<0.01

Spearman's). This indicates that the motor cortex neurons most sensitive to the activity of iSPNs are not the same as those most highly regulated by dSPN activity.

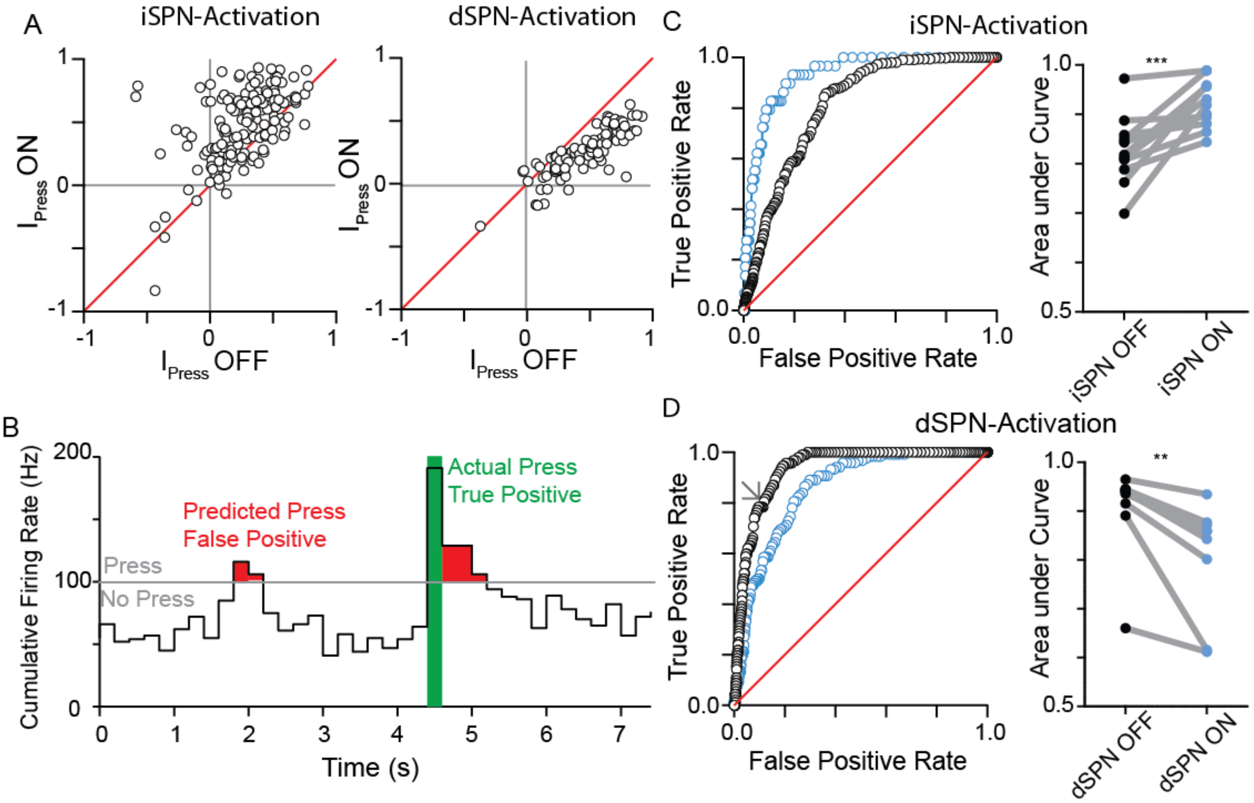

Figure 2.6. Bidirectional changes in the encoding of information in cortex.

A, index of modulation to presses during presses (±250ms around a tone to 1.5s baseline) with and without iSPN (*left*) and dSPN (*right*) activation are strongly correlated in each condition ($p<0.0001$; Spearman's Correlation 0.488 iSPN n=193 units; Spearman's correlation 0.830 dSPN n=136 units).

B, Signal to noise was measured by performing receiver operant characteristics on the summed activity from units recorded on one recording session. Activity above an arbitrary threshold (grey line) was considered a predicted press, if an actual press was detected it was recorded as a 'True Positive' (green line and bin) and if no press was detected it was categorized as a 'False Positive' (red bins). The schematic (B) shows 7.5s using a threshold indicated by the grey arrow in (D).

C-D, Every potential threshold from 0 to the maximum firing rate for a single recording session is examined and the corresponding true positive and false positive rate for each threshold is plotted (*right*) in control conditions (black circles) and with iSPN (C) or dSPN (D) activation (blue circles). (*left*) Area under each curve (AUC) is displayed with and without iSPN (C) and dPSN(D) activation. iSPN activation increases signal to noise (0.79±0.022 AUC OFF, 0.87±0.026 AUC ON; $P<0.01$ wilcoxon matched-pairs signed rank test, N=11 recordings, C) whereas dSPN activation reduced signal to noise (0.91±0.029 AUC OFF, 0.81±0.040 AUC ON; $P<0.01$ wilcoxon matched-pairs signed rank test, N=9 recordings, D).

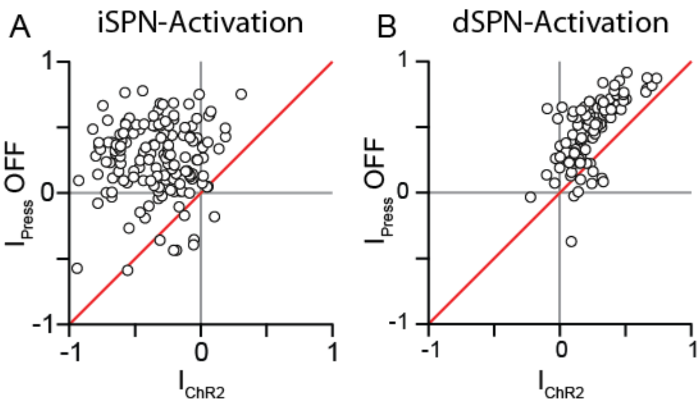

Figure 2.7. Pathways affect differentially affect different populations of units in cortex.

A-B, The press index is not correlated to the baseline index of modulation during iSPN activation (A, $p>0.05$; n=193 units; Spearman's Correlation -0.003) but is highly correlated during dSPN activation (B, $p<0.0001$; n=136 units; Spearman's Correlation 0.710).

2.4 Discussion

Here we present a direct examination of the circuit level interactions between basal ganglia and cortex, focusing on the effects of direct and indirect pathway activation in the dorsal striatum on primary motor cortex. Analyses were carried out in head-restrained behaving mice carrying out a simple cued motor action for water reward. To the best of our knowledge, this is the first functional determination of the effects of striatum activity on motor cortex in a behaving animal and, as such, provides an initial test of basic tenets of classic models of BG function. Our results demonstrate that striatum can exert rapid control over primary motor cortex that is powerful, dynamic, and dependent on the behavioral state. We find opposing effects of direct and indirect pathways on basal activity in primary motor cortex when the animal is not moving and not actively executing a task. Thus, at steady state, activation of the indirect and direct pathway suppresses and enhances, respectively, firing rates of units in motor cortex, consistent with classic models of BG/cortical interactions. However, the effects are more complex during movements or behaviorally relevant cues, revealing dynamical and non-opposing effects of iSPNs and dSPNs on cortical activity.

2.4.1 Experimental approach

To address gaps in our understanding of interactions between BG and cortex, we made recordings from primary motor cortex while optogenetically exciting the direct and indirect pathways of the BG in an awake and behaving mouse. Our goal was not to perform a behavioral study of the effects of BG on task performance, but rather to study circuit-level interactions in a physiologically relevant non-anesthetized state. As dorsal striatum is engaged in goal directed movements (Thorn et al. 2010; Balleine et al. 2007), we implemented a simple motor action based operant conditioning task. We intentionally did not train the mice to ideal performance since comparison of quiescent periods, success trials, failure trials and spontaneous actions allow analysis of the circuit in a variety of behavioral states. As synchronous activity of striatum can be a hallmark of disease (Brown 2007), we and other groups (Kravitz et al. 2010; Freeze et al. 2013) used steady state low-power illumination to activate striatal neurons, avoiding brief trains of intense illumination that synchronize SPN firing. Furthermore, by alternating trials with and without optogenetic stimulation we minimize potential sources of error due to difference between animals or genetic backgrounds.

2.4.2 Behavioral effects

Consistent with pro-kinetic and anti-kinetic effects, dSPN and iSPN activation displayed opposite ~3 fold changes in spontaneous lever press frequencies, and iSPN activation increased level press durations, as expected from freezing like behavior(Kravitz et al. 2010). Similarly, cued lever press rates are bidirectionally modulated by the two pathways. Thus, a trained motor action (i.e. lever press) carried out either spontaneously without reward or cued for reward is promoted by dSPN activity and inhibited by iSPN activity in the mouse. Such effects are often described as pro- and anti-kinetic, respectively, and are consistent with classic models of direct/indirect pathway functions (Albin et al. 1989), recent manipulations in mice (Kravitz et al. 2010; Bateup et al. 2010), and theories of increased indirect pathway activity underlying freezing behavior in Parkinson's disease (Albin et al. 1989). On the other hand, these results are also consistent with models in which the indirect pathway does not serve a "no-go" type function but is instead important for switching between motor actions. Our results are consistent with both interpretations since our analysis is of a single behavior carried out from a resting state such that action initiation is equally well described as a go/no-go transition or as a transition between motor states.

2.4.3 Classic circuit models

The classic model of the BG was developed from anatomical studies linking the nuclei of the BG to thalamus and cortex, revealing a cortex-basal ganglia-thalamus-cortex loop (Alexander & Crutcher 1990; DeLong 1990) and refined by identification of neurotransmitters and molecular markers in striatopallidal and striatonigral neurons (Gerfen et al. 1990). These circuit models propose that the output of the BG is via inhibition and disinhibition of thalamic nuclei whose cortical projections mediate subsequent down- and up-regulation of cortex activity (Deniau & Chevalier 1985). Thus, the pro-kinetic and anti-kinetic properties of the direct and indirect pathway are thought to be via the enhancement (direct) or suppression (indirect) of activity in a recurrent cortex-basal ganglia-thalamus loop.

During periods when the animal is waiting without movements for the go cue, activation of dSPNs and iSPNs increase and decrease, respectively, firing rates in primary motor cortex. These effects are strong (up and down ~2 fold modulation), widespread (~2/3 units showing significant modulation), and consistent with predicted antagonist effects of each striatal pathway on cortex. These effects are as predicted by classic models in which the direct pathway enhances activity in the recurrent loop and facilitates motor action initiation, and the indirect pathway has opposite effects. Thus, in the simplest analysis and when coupled with the behavioral effects described above, our results support the classic model of BG function. In addition, by revealing effects in an upstream area (cortex) caused by manipulated activity in a downstream area (striatum), this marks the first functional demonstration of the recurrent nature of the BG-cortex circuitry.

In addition, our results provide evidence for underlying assumptions about activity in the cortex-basal ganglia-thalamus recurrent loop that are often not directly stated. For example, the control of cortex by BG is proposed to be mediated by modulation of the degree of inhibition of the thalamus by GABAergic outputs of the BG in the SNr. Thus, in order for the dSPNs and iSPNs to bidirectionally modulate cortical activity, it is necessary that the SNr output provide tonic inhibition of the thalamus that is significant but not saturated. Although SNr output neurons are tonically active, synaptic depression during maintained high frequency firing might diminish the inhibitory influence of BG output on thalamus. Furthermore, in order to translate changes in BG output into alterations of basal firing rates in cortex, the thalamocortical projection neurons need both to supply sufficient ongoing activity to account for a significant fraction of cortical excitatory drive and to be under the control of inhibition from BG. The bidirectional modulation of basal firing rates in primary motor cortex by dSPN and iSPN activation shown here supports the fundamental conclusions of classic models.

2.4.4 Beyond classic models

Recent results indicate the simple classification of dSPNs and iSPNs as go and no-go pathways, respectively, does not fully account for the activities of these cells in behaving mice since neurons of both classes are active during both the initiation and suppression of movements (Cui et al. 2014; Isomura et al. 2013). Furthermore, in monkeys, BG activity is concurrent or delayed relative to movement initiation, suggesting a function in shaping but not necessarily initiating motor action and associated circuit activity (Mink & Thach 1991; Hikosaka et al. 1989; Aldridge et al. 1980).

Resolving these issues requires knowledge of the kinetics of effects of striatal activity on other brain structures. Within models of cortex/BG interactions as recurrent loops, the kinetics of the recurrent interactions are basic model constraints that are currently unknown. We find that activation of dSPNs or iSPNs modulates cortical activity with short latencies (average ~120 ms dSPN, ~165 ms iSPN), with some cells responding in the first 50ms. This is slower than the time of striatal modulation of SNr (~ 100ms, (Freeze et al. 2013)), consistent with the presence of additional two synapses between SNr and cortex. Given the short latency of cortically evoked action potentials in striatum (5-7ms (Koralek et al. 2013)), our data indicate that a complete closed loop interaction from cortex to striatum and back can occur in less than 200ms.

In addition to these rapid kinetics, our results reveal a complex dynamical response in cortex to striatal activation that violates the predicted symmetric effects of dSPN and iSPN activity on cortex. As described above, during quiescent periods the effects of dSPN and iSPN activation are opposing and similar in magnitude. However, such symmetry breaks for activity around cued and spontaneous lever presses. Although iSPN activation reduces baseline and peak activity in primary motor cortex evoked by cues and cued lever presses, activation of dSPNs has no effect on peak firing rates in these behaviorally relevant periods. These effects are not due to a ceiling effect of cortical firing rates since the peak-firing rate reached in cortex during a failure trial is well below maximal and yet unaffected by activation of dSPNs. An alternative explanation is that dSPNs, or circuit elements downstream of dSPNs, are maximally active during the movement such that optogenetic stimulation of dSPNs has no further effect.

Such an explanation would also imply that iSPNs are comparatively less active during these periods than dSPNs, which at first may appear in conflict with results observing movement related activity from both iSPNs and dSPNs *in vivo* (Cui et al. 2014; Isomura et al. 2013). However, this may be reconciled by differences in the sustained activity of dSPN and iSPN during movement bouts, dSPNs being largely active while iSPNs are largely inhibited (Jin et al. 2014). Indeed, in motor cortex, we see much greater effects of iSPN activation leading up to a press than during the movement itself, implying that some iSPN activation may be present during the presses.

Alternatively, a model in which BG provide a modulatory or gating role in thalamus may be equally consistent with our findings. In this model when the animal is not moving the BG increases or decreases cortical activity by allowing spurious, non-movement related, activity to transmit from thalamus to cortex. When a movement is happening no further activation is possible, the gate is open, thus the direct pathway does not increase activity. However suppression is still possible via increased indirect activity.

Furthermore asymmetric effects of dSPNs and iSPNs on cortex are seen in the existence of a subset of cortical neurons (~30% of total) that are transiently activated when iSPNs are stimulated. The majority of cortical neurons monotonically decrease firing following iSPN activation and increase back to baseline levels upon cessation of iSPN stimulation. In stark contrast, those cells that are transiently excited reduce their firing rate after ~500ms of excitation, and rebound strongly upon cessation of iSPN stimulation. We were unable to find an analogous class of units that either displayed non-canonical direction of action or equivalent responses to initiation and cessation of dSPN stimulation. Thus this non-canonical transient excitation appears to be iSPN specific.

It is of particular interest that the transiently excited cells appear in predominantly superficial layers. Thalamocortical activity from the VLo, and thus modulated by the BG, primarily innervates the superficial layers (McFarland & Haber 2002; Kuramoto et al. 2009) although some axons are reported in deeper layers (Constantinople & R. M. Bruno 2013). These transiently excited cells may receive direct thalamocortical input that is atypically sensitive to BG outputs, or may respond in highly specific manner to cortical microcircuitry. In either case this subset of neurons in the motor cortex need to be incorporated into future models of basal ganglia-thalamo-cortical circuitry.

2.4.5 Effects on encoding properties of cortex

Determining the effects of the BG on large populations of neurons in downstream areas is necessary for a complete understanding of how this structure interacts with its connected neighbors. We examined how the encoding of movement initiation in motor cortex is altered by indirect and direct pathway modulation. In general, the activity of each individual cortical unit retained its specific dependence on behavioral state during activation of dSPNs and iSPNs – e.g. a neuron that responds strongly to at the time of a spontaneous movement continues to do so during optogenetic stimulation of the striatum. However, the converse is not true such that the degrees of modulation of individual units and of the population as a whole are highly dependent on behavioral context; such basal firing rates were highly affected by stimulation of either pathways whereas the peak firing rates around the times of spontaneous lever presses were largely unaffected. Thus from a movement-initiation perspective, the signal to noise of the population activity and the ability of an observer to predict the timing of a motor action by observing cortical activity were enhanced by iSPN and reduced by dSPN activity.

At the population level, differences between the cortical effects of iSPN and dSPN activation were also evident. Whereas a good correlation was observed between each neuron's modulation by dSPN activation and its lever press related change in firing rate, no similar correlation was found when iSPNs where activated. This is especially intriguing as the iSPN and dSPN projections target the same neurons in the SNr (Smith & Bolam 1991), and thus it is difficult to explain differential effects on cortex via a common output. This may suggest the existence of additional outputs of the BG that are differentially dependent on iSPN and dSPN activity. Alternatively, it is possible that undetected movements are present and differentially sensitive to dSPN and iSPN activation. However, such significant effects would be expected to result in strong correlations between the degree of modulation of firing of a neuron during a movement and its sensitivity to optogenetic modulation in the striatum of either iSPNs or dSPNs.

2.5 Conclusions

Here we report the results of the first direct examination of the effects of striatal activity on the primary motor cortex. We find that the predictions of classical models of BG/cortex interactions are well supported by results obtained from mice in a quiescent state such that the BG exert large, fast, push-pull control over motor cortex. However, the classic model fails to account for the effects of striatal manipulations while the animals are making spontaneous or cued movements, or for the asymmetric effects of direct and indirect pathway activation on cortex. Our results indicate the existence of circuitry, either within nuclei downstream of the striatum and between the BG and cortex, which allow differential and non-opposing effects of dSPNs and iSPNs on cortex.

2.6 Materials and Methods

Surgical Procedure. All animal procedures were approved by the Institutional Animal Care and Use Committee at Harvard Medical School and conform to the National Institutes of Health guidelines. Transgenic male mice (30-60 days postnatal age) expressing Cre recombinase in either dSPNs (B6.FVB(Cg)-Tg(Drd1a-cre)EY217Gsat/Mmucd, from MMRC) or iSPNs (B6.FVB(Cg)-Tg(Adora2a-cre)KG139Gsat/Mmucd from Gensat) were fitted with a custom-made Titanium headpost and infected with 500 µl of a Cre dependent ChR2 AAV (2/5.EF1.dflox.hChR2(H1134R)-mCherry.WPRE.hGH, available from University of Pennsylvania Vector Core) into the Striatum at coordinates 0.9mm Anterior, 1.7mm Lateral from Bregma, and 2.8mm Deep. They were then housed singly in a semi reversed light cycle (Light 10pm – 10am).

Training. Following 1 week of recovery animals were trained to be head restrained and to press a lever in response to an auditory cue via operant conditioning and positive reinforcement. Animals were water restricted to a target of 80-85% of their free access weight. Trained animals would routinely get more than their required water allotment through training, in the case that they were underperforming supplementary water would be given to bring them up to 10-25mg/kg/day. Animals were handled for ~10 minutes on the first day prior to headfixed training.

Head restrained training was done 6 days/week for up to 90 min/day in the early period after lights off (10am-5pm) using a custom rig running a custom made training program written in MATLAB. If the animal withholds pressing through a period of random duration, 1.5-5s, a 50ms 50db 10kHz tone will play indicating the start of a trial. The animal then has a short period to press the lever for a water reward. The program is designed to gradually tighten or relax reward criteria as the animal performs better or worse. The rewarded period begins at a generous 10s window and collapses by 10% every reward until it reached 1.5s. If the animal does not receive any rewards in 40s this period will grow by

0.75s. The inter-trial interval compensates to remain a random period centered on 9s. In addition the volume of each reward was dynamic increasing from 2 to 8µl/reward for faster responses. Responses within the first 200ms received 8µl, this reduces smoothly to 4µl for a 1s reaction time, and to 2µl by the end of that trials rewarded period. Once animals were proficient with the training task they were moved to a static variant of the task, typically around 14 training days. All recordings were done on a static variant of this program with a fixed 1.5s rewarded period and a 4µl reward size regardless of reaction time.

Once, animals obtained a sufficient level of proficiency on the static task (125 rewards in 90min), typically after 14-21 days, a fiber optic (62.5um core diameter 0.22 NA) and ferrule connector (precision fiber products) were implanted in striatum through the original craniotomy at a tip depth of 2.2-2.4mm and a second craniotomy was opened over motor cortex (0.25 anterior, 1.5 Lateral) and sealed with Kwik-Cast silicone Elastomere. The fiber optic and connector were confirmed to have >75% transmission prior to implantation. Optical stimulation was achieved by coupling a 473nm Laser (Ciel, Laser Quantum) through an Acusto-Optic Modulator (AA opto-Electronic) for fast shuttering and intensity control. Final light power entering the chronic fiber was between 1.5-3.0mW. Illumination was constant during alternating trials for the length of a training session. During optogenetic experiments house lights were kept on to reduce the risk of the animal detecting changes in laser illumination.

In vivo electropysiological. *In vivo* electropysiological recordings were made using 16 or 32 channel probes (177 or 413µm^2) with recording site arranged in one or two linear arrays all from NeuroNexus Technologies) mounted at a 30° angle with respect to the surface of the skull. For cortical recordings, electrodes were positioned with the tip of 900-1500µm deep, ~600 µm below the first active channel. Striatal recordings were made either using an optrode (model OA16 from NeuroNexus Technologies) at the same coordinates as a typical fiber implantation (0.9 Anterior, 1.7 Lateral, 2.2mm Deep) or using the typical 16 or 32 channel probes via a deep, angled penetration from the motor cortex until the electrode was in the field illuminated by the fiber optic. In the latter case proper placement was ensured via identifying optical artifacts in the recording channels that corresponded with light onset and offsets.

Animals were excluded if they did not reach sufficient level of proficiency before they reached 12 weeks of age, if they could properly articulate their displeasure with the task, or in the event of infection or damage to the headpost, chronic fiber or craniotomy. In total 18 mice were used for optogenetic behavioral experiments (7 iSPN, 3 control, 8 dSPN), of those 8 were used for recordings (4 iSPN, 4 dSPN).

Spiking was filtered at 1-8000 Hz, digitized at 40kHz and sorted into single and multi-unit activity via principal component analysis using Plexon Inc.'s Omniplex and Offline Sorter systems, respectively. Data were further analyzed using IGOR Pro and Matlab. In certain cases (**fig. 2.4**) units were discarded if the combination of the number of stimulus events recorded times the baseline firing rate were not sufficient to achieve 30 spikes in the 1.5s baseline period.

Intracortical microstimulation. Intracortical microstimulation was performed similar to (Tennant et al. 2011) using a concentric bipolar stimulating electrode (FHC) using a 50ms train of 16 pulses at a depth of 400-800µm. The amplitude of stimulation was increased until a response was seen or the stimulating device became saturated (1 mA). Areas of response were categorized based on visual observation of twitches and jerks and related to the position in motor cortex based on their position within the craniotomy.

Gaba inactivation. GABA inactivation of motor cortex was achieved by injecting 50nl 100mM GABA (Sigma) through a glass injection (Drummond) needle at 100nl/min into a behaving mouse. Well trained animals were used and GABA infusion performed during bouts of activity, after the animal had been successfully getting rewards for at least 3 minutes.

ROC analysis. For the ROC analysis all spiking data for a given recording was summed together and binned at 200ms. If a press was detected at any time in a given bin that bin would be classified a press bin. The true positive rate is calculated as the fraction of press bins that have a summed spike rate greater than the threshold; false positive rate is the fraction of non-press bins that have a summed spike rate greater than the threshold. All thresholds from 0 spikes/bin to the maximum observed spikes/bin were tested and plotted in **Fig 2.6b**.

Latency analysis. Latency was calculated similar to Freeze et al 2013. Each unit's firing activity was binned in 50ms bins and aligned to the time of the light transition. A 1.5s baseline period was defined immediately prior to the light transition, from which a mean and standard deviation of firing rate was defined. The latency to change was defined as the first 50ms bin after the light transition to be > or < 2 standard deviations from the baseline firing rate. Units that did not reach a significant level by 500ms were excluded from analysis.

Statistical Analysis. All error bars are mean +/- SEM unless otherwise noted. All statistical tests performed were non-parametric tests and were constructed as matched pairs when possible to remove differences between unit's firing rates. For all electrophysiological recordings more than 75 units were recorded for each condition. An explicit power analysis was not performed prior to experimentation, but sample sizes were determined based on communication with experts and comparison to other similar published work. No randomization or blinding was needed in this work.

Units were typically only excluded during the sorting phase based on waveform, if the cluster appeared to be within the noise cluster. For the latency analysis, units were excluded if no significant change in latency was detected within 500ms; this threshold was determined prior to analysis. For the depth analysis (**Fig 2.4d**), one recording (16 units) lacked depth information and was excluded. In the graphs in **figure 2.5A,B**, units were excluded if there were less than 30 spikes detected in the total number of baseline periods for a given class of result (i.e. failure trial, success trial, or uncued press), as this resulted in an unreliable amount of data and noise. This was most problematic in the Success trial with iSPN activation, as during stimulation mice performed very poorly limiting the number of trials obtainable. This was determined after data collection, but inclusion of these results does not change the interpretation of them.

Chapter 3

A direct GABAergic output from the basal ganglia to frontal cortex

Ian Antón Oldenburg, Arpiar Saunders and Bernardo L. Sabatini

This chapter is based on work that has been submitted for publication, but has been abbreviated and focused on the *in vivo* recording sections.

Arpiar Saunders, Ian A. Oldenburg, Vladimir Berezovskii, Caroline A. Johnson, Charles R. Gerfen and Bernardo L. Sabatini. (2014) A direct GABAergic output from the basal ganglia to frontal cortex

Acknowledgement of the work of others:

This work was done in collaboration with Arpiar Saunders and others in the lab of Bernardo Sabatini. Arpiar Saunders performed all *in vitro* recordings; Ian Oldenburg performed all *in vivo* recordings; Arpiar Saunders, Ian Oldenburg, Vladimir Berezovskii, Caroline Johnson, and Charles Gerfen contributed to the microscopy and analysis of fixed tissue; Arpiar Saunders, Bernardo Sabatini and Ian Oldenburg designed the experiments and wrote the manuscript.

3.1 Abstract:

The basal ganglia (BG) are a phylogenetically conserved set of subcortical nuclei necessary for coordinated motor action and reward learning(Yin & Knowlton 2006). Accepted models postulate that the BG modulate cerebral cortex indirectly via an inhibitory output to thalamus, bidirectionally controlled from within the BG by striatal direct (dSPNs) and indirect (iSPNs) pathways spiny neurons(Smith et al. 1998; Kravitz et al. 2010; Freeze et al. 2013). This thalamic output sculpts cortical activity by interacting with signals from the sensory and motor systems (Goldberg et al. 2013). Here we describe a direct projection from the globus pallidus externa (GP), a central nucleus of the BG, to frontal regions of the cerebral cortex. Two cell types make up the GP-FC projection, distinguished by their electrophysiological properties, cortical projection patterns and expression of choline acyteltransferase (ChAT), a genetic marker for the neurotransmitter acetylcholine. Despite these differences, ChAT+ cells, which have historically been identified as an extension of the nucleus Basalis, as well as ChAT- cells, release the inhibitory neurotransmitter GABA (γ-aminobutyric acid) and are inhibited by iSPNs and dSPNs of dorsal striatum. Thus GP-FC cells affect frontal cortical activity via a direct GABAergic/Cholinergic projection under the unidirectional control of the direct and indirect pathways. Since GP-FC cells receive dopamine sensitive inhibition from iSPNs and dSPNs, this circuit reveals a pathway by which drugs that target dopamine receptors for the treatment of neuropsychiatric disorders can act in the BG yet modulate frontal cortices.

3.2 Introduction

iSPNs of dorsal striatum are the major dopamine 2 receptor (D2r) expressing cells in the brain and project extra-striatal axons exclusively to the globus pallidus externa (GP). This connectivity suggests the therapeutic effects of drugs that target D2rs to treat Schizophrenia, bipolar disorder and obsessive compulsive disorder, likely affect GP circuits. In humans, the GP is one of the most transcriptionally distinctive regions of the brain (Hawrylycz et al. 2012), yet how this molecular diversity maps onto functionally distinct cell types is unclear. The anatomy of projection axons, intrinsic firing properties, and synaptically released neurotransmitters often distinguish neuron types and determine the function of each type in controlling neuronal circuitry and behavior. Previous studies generally describe that GP neurons are spontaneously active, project to all nuclei of the BG and thalamus (Takada et al. 1986), and release the neurotransmitter GABA (Kita 2007). Thus the GP is thought to coordinate subcortical activity through inhibition (Bevan et al. 2002; Chan et al. 2005).

In contrast to this accepted function, anatomical studies across species have identified ChAT$^+$ neurons in and around the GP that project to cortex (Saper & Chelimsky 1984; Mesulam et al. 1984; McKinney et al. 1983) These cells have been assumed to be an extension of the adjacent nucleus basalis (NB), associated with the limbic functions of the basal forebrain and not the motor, sensory and cognitive functions of the BG (Heimer et al. 2007). However, several lines of evidence suggest they may be part of GP. Anatomically, ChAT$^+$ GP cells appear to be innervated by SPNs from dorsal striatum (Grove et al. 1986) despite the rarity of iSPN-identified synapses at the ultrastructural level (Chang et al. 1987). Functionally, *in vivo* macaque recordings described GP neurons with NB-like firing properties that were responsive to reward (DeLong 1971), a computation attributed to the BG (Schultz et al. 2003). Behaviorally, humans with lesions of the GP exhibit reduced metabolism in frontal cortices and psychiatric symptoms reminiscent of patients with fronto-temporal lobe damage, consistent with loss of extrinsic input (Laplane et al. 1989). Therefore we asked whether the GP contains a projection system to frontal cortex (FC) that is integrated into BG circuitry.

3.3 Results

3.3.1 ChAT+ and ChAT- GP-FC cells

Since the GP is the sole innervation target of D2r expressing iSPNs of the striatum, we performed retrograde labeling by injecting fluorescent microspheres (retro beads) into the FC of *Drd2*-EGFP mice to identify FC projection neurons with respect to the anatomical borders of the GP (**Fig. 3.1a**). Retro bead^{+} cells were found within the GP and clustered on the GP/NB and GP/striatum borders (**Fig. 3.1b**).

To investigate if GP-FC cells use GABA or acetylcholine as a neurotransmitter, we repeated retrograde labeling in *VGAT*-i-Cre/+;lsl-zsGreen$^{fl/+}$ mice where cells expressing the vesicular GABA transporter (*vgat*, encoded by *Slc32a1*) are fluorescently labeled and immunostained for ChAT (**Fig. 3.1c**). All retrobead^{+} GP cells were *vgat*$^{+}$ (n=159 of 159 cells), whereas 72% were ChAT^{+} (n=215 of 300 cells) and 28% ChAT^{-} (n=85 of 300 cells) (**Fig. 3.1d**). Based on ubiquitous *vgat* but differential ChAT expression, we conclude that the GP-FC projection consists of two molecularly distinct cell types (Rye et al. 1984) (hereafter ChAT+ and ChAT- cells) and that ChAT^{+} cells of the adjacent NB express a GABAergic marker, consistent with previous transcriptional analysis (Tkatch et al. 1998). ChAT^{-} GP-FC cells did not express the calcium binding protein parvalbumin (PV) (**Sup Fig. 3.1**), consistent with finding that PV^{+} GP neurons projecting to posterior BG nuclei (Mallet et al. 2012) and distinguishing ChAT^{-} GP-FC these cells from other non-cholinergic cortical projecting cells found across the basal forebrain (Henny & Jones 2008; Sarter & J. P. Bruno 2002).

Figure 3.1. The Globus Pallidus (GP) and bordering nucleus Basalis (NB) contain two GABAergic cell types that project to frontal cortex.

(A) Left, sagittal section from a Drd2-EGFP mouse injected with retro beads (red) into frontal cortices (FC), which include dorsal and ventral agranular insular cortex, as well as anterior regions of primary motor, secondary motor and primary sensory cortex. EGFP (green) is expressed in iSPNs of the striatum (Str). iSPN axonal projections arborize in the GP and define its anatomical boundaries. DAPI (blue), nuclear stain. Right, higher magnification view of the GP from a single, more medial section from the same mouse. Retrobead+ neurons (inset and highlighted with circles) are located in the GP and around the GP/NB border. ac, anterior commissure; VP, ventral pallidum.

(B) Overlaid locations of retrobead+ cells in the central ~300 µm (medial-lateral axis) of GP from separate FC injections (n=3 mice).

(C) FC retro bead labeling in VGAT-i-Cre/+;lsl-zsGreenfl/+ mice followed by ChAT immunostaining (magenta) demonstrates that all retrobead+ GP cells (red) are VGAT-i-Cre+ (green) while some retrobead+ cells are also ChAT+ (solid circles) and others are ChAT- (dashed circles). Top, low magnification sagittal view of the GP. Bottom, a single confocal plane from a stack used to quantify marker colocalization.

(D) Summary of co-expression of VGAT-i-Cre (n=3 mice) and/or ChAT (n=5 mice) in retrobead+ GP neurons.

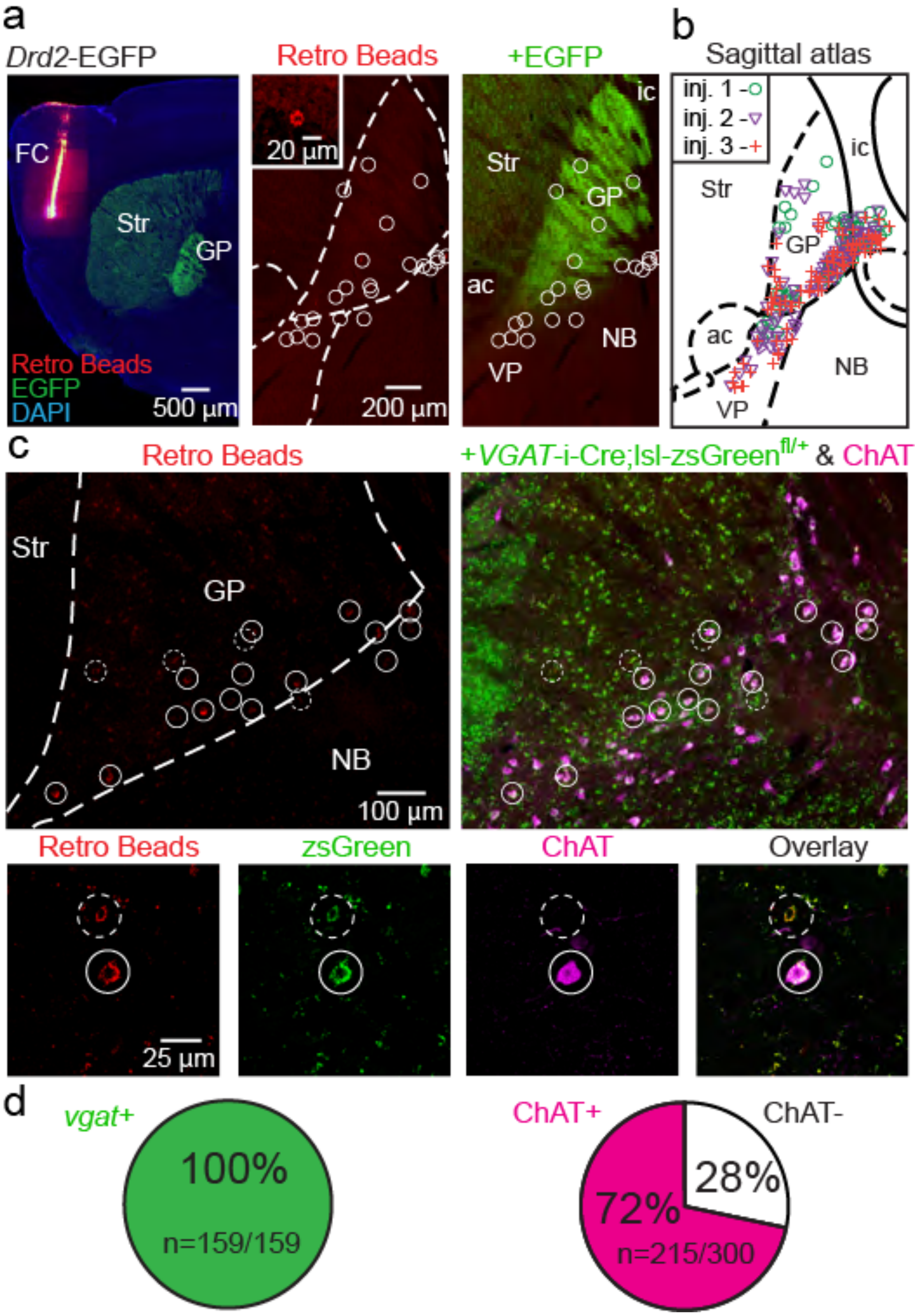

Figure 3.1. (Continued): The Globus Pallidus (GP) and bordering nucleus Basalis (NB) contain two GABAergic cell types that project to frontal cortex.

3.3.2 Targets of GP-FC cells

To determine if ChAT- and ChAT+ cells have distinct circuit functions, we compared their cortical projection patterns and electrophysiological properties. Differential labeling of GP-FC cells in ChAT-i-Cre mice was accomplished using rAAVs to differentially express fluorophores in intermingled Cre+ and Cre- neurons (Saunders et al. 2012) (**Sup Fig. 3.2a-f**). The brains of mice with injections of rAAVs confined to the GP and adjacent NB were reconstructed in three-dimensions in order to measure axonal densities across cortical areas and layers (n=2 mice) (**Fig. 3.2a,b**). ChAT+ and ChAT- cells send a pronounced projection to FC, targeting different but overlapping cortical areas and layers (**Fig. 3.2c**). In anterior primary motor cortex (M1), ChAT+ axons arborize in layers 1-6, most densely in layers 1 and 2/3, whereas ChAT- axons arborize densely in layers 5 and 6, sparsely in layer 2/3 and are absent from layer 1. This layer distribution is representative of most but not all cortical areas, including the ectorhinal cortices, which receives a strong GP-FC projection (**Sup Fig 3.2g**). GP-FC cells also target distinct but overlapping subcortical nuclei. ChAT+ cells arborize in the thalamic reticular nucleus (Rt), the basal lateral amygdala (BLA) and the substantia nigra reticulate (SNr). ChAT- cells target the expected nuclei of the BG, the striatum (Str), subthalamic nucleus (STN) and Substantia Nigra reticulata (SNr), as well as the BLA, lateral habenula and thalamic Rt and parafasicular nuclei (**Sup Fig 3.2h**).

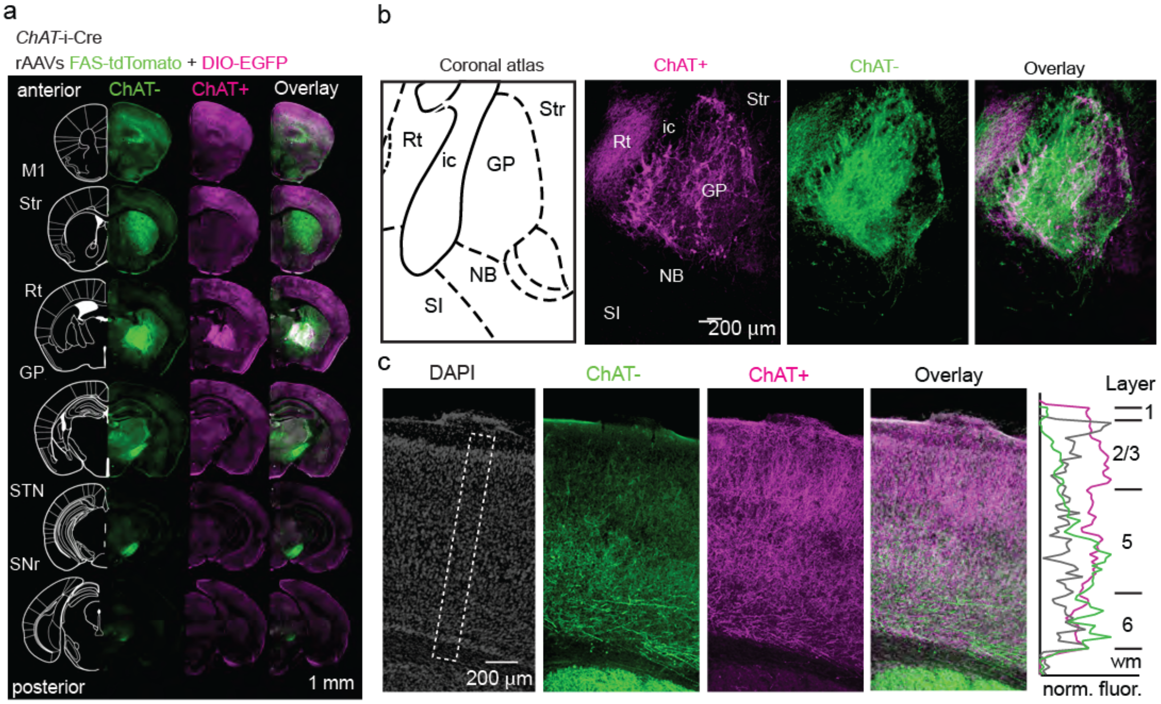

Figure 3.2. GP-FC axons arborize in distinct areas and layers of frontal cortex.

(A) Coronal sections of a *ChAT*-i-Cre mouse injected in GP with rAAVs DIO-EGFP (Cre-On, magenta) and FAS-tdTomato (Cre-Off, green) sampled from a whole-brain reconstruction. The injection site (GP, shown in **b)** and anterior primary motor cortex (M1, shown in **c**) are indicated along with the BG. Str, striatum; Rt, thalamic reticular nucleus; STN, subthalamic nucleus; SNr, Substantia Nigra reticulata.

(B) *Left*, coronal atlas. *Right*, injection site showing ChAT+ (Cre-On) expression limited to GP and the adjacent NB. ChAT- (Cre-Off) expression is limited to GP with slight leak in striatum. ChAT+ and ChAT- axons arborize in Rt. SI, substantia innominata; NB, nucleus Basalis; ic, internal capsule.

(C) *Left,* distribution of GP-FC axons across layers of anterior primary motor cortex (M1). *Right,* line scan of average fluorescence across layers, normalized to peak and baseline subtracted by white matter signal.

Elucidating how GP-FC cells influence cortical activity requires defining the neurotransmitters released by each cell type and identifying their post-synaptic targets. To address these questions, we introduced the light-gated cation channel channelrhodopsin (ChR2) selectively into ChAT- or ChAT+ GP-FC cells using Cre-activated or inactivated rAAVs (Saunders et al. 2012) injected into the GP and adjacent NB of *ChAT*-i-Cre;GAD67-GFP mice (**Fig. 3.3a**). To characterize the currents recruited by GP-FC axon stimulation, we cut acute brain slices and made whole-cell voltage-clamp recordings from somata surrounded by (<150 mm) ChR2$^+$ axons (**Fig. 3.3b**).

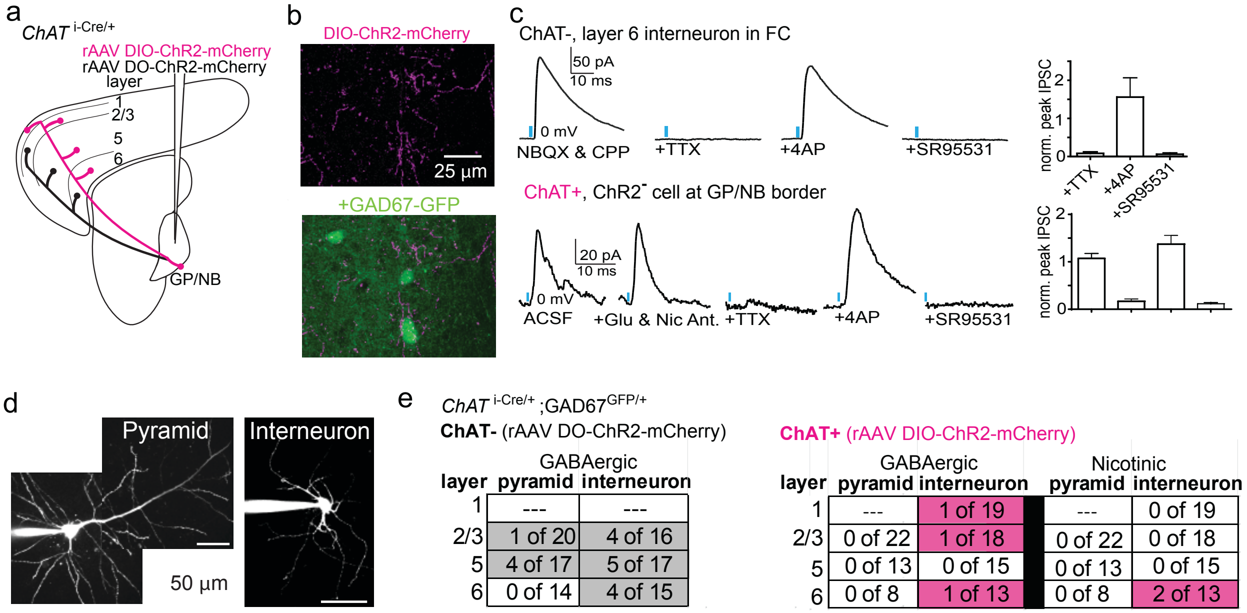

Figure 3.3 GP-FC cells release GABA and ACh in frontal cortex (FC).

(A) Illustration of cortical (ChAT+ and ChAT-) and local (ChAT+) GP-FC axons expressing ChR2-mCherry after rAAV transduction in *ChAT* $^{i\text{-}Cre/+}$ GP. Labeled areas were targeted for paired whole-cell recordings and optogenetic activation.

(B) Max projection confocal stack (30 mm) of ChAT+ axons in FC layer 6 following transduction of rAAV DIO-ChR2-mCherry in GP of *ChAT* $^{i\text{-}Cre}$;*GAD67*$^{GFP/+}$ mouse. Whole-cell recordings were targeted to somata within 150 mm of the ChR2$^+$ arbors. GFP fluorescence helped identify GABAergic interneurons (GFP$^+$) or non-GABAergic pyramidal neurons (GFP$^-$).

(C) *Top left,* currents in a layer 6 interneuron held at indicated potentials evoked by optogenetic activation of surrounding ChAT- axons under baseline conditions (NBQX and CPP) and following co-application of (from *left* to *right*) TTX, 4AP and SR95531. *Top right*, IPSC peak amplitudes across conditions normalized to baseline (n=5 cortical interneurons). *Bottom left,* evoked current responses in a ChR2$^-$ neuron at the GP/NB border held at indicated potentials to optogenetic activation of surrounding ChAT+ cells under baseline conditions (ACSF) and following co-application of (from *left* to *right*) glutamate (NBQX & CPP) and nicotinic (MEC, MLA & DHβE) receptor antagonists, TTX, 4AP and SR95531. *Top right*, IPSC peak amplitudes across conditions normalized to baseline (n=7 ChR2$^-$ GP/NB cells).

(D) Maximum intensity projection of dendritic morphology following whole-cell recording used to identify FC neurons as pyramids or interneurons. *Top*, a layer 5 pyramidal neuron. *Bottom*, a layer 1 interneuron.

(E) Synaptic connectivity screen for cortical neurons with monosynaptic (present in TTX/4AP or <3.1ms onset latencies) ChR2-evoked ionotropic current responses from ChAT+ or ChAT- axons. ChAT- data includes cells in **Fig 3.3c**.

Recordings post-synaptic to ChAT- axons were made in FC at ~0 mV (the reversal for ionotropic glutamate and nicotinic receptors) and in the presence of NBQX and CPP to block ionotropic glutamate receptors. In a subset of neurons (n=5 of 94), optogenetic activation evoked fast outward currents (**Fig. 3.3c**). These light-evoked inhibitory post-synaptic currents (IPSCs) were blocked by the voltage-gated sodium Na^+ blocker tetrodotoxin (TTX), demonstrating ChR2 depolarization alone was not sufficient for transmitter release. IPSCs could be rescued in the continued presence of TTX by enhancing ChR2 mediated depolarization of terminals with application of the voltage-gated K^+ channel blocker 4-aminopyridine (4AP) and were abolished in the presence of the $GABA_A$ receptor antagonist SR95531, indicating direct (monosynaptic) release of GABA by ChAT- cells.

The effect of ChAT- and ChAT+ GP-FC cell activity on cortex will depend on the identity of synaptically targeted cells and the neurotransmitter receptors these targeted cells express. In cortex, GABA and ACh can signal through ionotropic and metabotropic receptors, both of which can be expressed pre and post-synaptically. Cortical microcircuits are organized by layer(Tepper & Bolam 2004; Lefort et al. 2009) and include two major classes of neurons: Pyramidal neurons that excite local and distant targets through the release of glutamate and a diverse set of interneurons that inhibit other cortical neurons through the release of GABA(Marsden 1982; Markram et al. 2004). We focused on post-synaptic ionotropic receptor signaling as it allows unambiguous identification of monosynaptic connections. We introduced ChR2 into ChAT+ and ChAT- GP-FC cells by rAAV injection in the GP of *ChAT* $^{i\text{-}Cre}$;$GAD67^{GFP/+}$ mice and targeted whole-cell voltage-clamp recordings to FC somata within 150 mm of $ChR2^+$ axons.

We light-activated axons and screened for direct (present in TTX/4AP or short-latency) nicotinic EPSCs and GABAergic IPSCs at -70 and 0 mV. Following recording, we determined the layer (1, 2/3, 5 and 6) and type (pyramidal neuron or interneuron) of cells, based on location, GAD67^{GFP} expression and dendritic morphology (**Fig. 3.3d**).

Activation of ChAT- axons evoked reliable IPSCs onto interneurons in layers 2/3, 5, and 6, as well as a pyramids in layers 5 and 2/3. Activation of ChAT+ axons produced less reliable ionotropic currents. We detected IPSCs in a small number of interneurons in layers 1, 2/3 and 6 and EPSCs in interneurons in layer 6 (**Fig. 3.3e**). We conclude that GP-FC signaling in FC is complex: ChAT- axons release GABA onto pyramidal neurons and interneurons, whereas ChAT+ axons release ACh and GABA exclusively onto cortical interneurons. ChAT+ and ChAT- neurons may additionally affect FC through metabotropic receptor signaling, pre-synaptic modulation of transmitter release, or by ionotropic signaling in distal dendrites.

3.3.3 GP-FC cells are part of the BG

To determine whether iSPNs and dSPNs axons synapse onto GP-FC cells, we targeted retro bead labeled GP-FC cells for whole-cell voltage-clamp recording in *Adora2a*-Cre;Rosa26$^{lsl\text{-}ChR2\text{-}EYFP/+}$ or *Drd1a-Cre*; Rosa26$^{lsl\text{-}ChR2\text{-}EYFP/+}$ mice where ChR2 is expressed in iSPNs or dSPNs, respectively (**Fig. 3.4a**). Ionotropic GABA receptor currents were pharmacologically isolated and measured in voltage-clamp at 0 mV as outward currents. Light-activation of iSPN or dSPN axons surrounding the recorded cell evoked SR95531-sensitive outward currents in nearly all GP-FC cells (ChAT+: 20 of 22; ChAT-: 19 of 20), indicating high GABA$_A$ receptor mediated connectivity. dSPN activation evoked larger peak synaptic currents onto ChAT+ cells than iSPN activation (dSPNs: 1.11±0.19, iSPNs: 0.57±0.17 nA), consistent with the larger axonal territory of dSPNs at the GP/NB border. Activation of dSPNs and iSPNs evoked similar, strong synaptic currents onto ChAT- cells (dSPNs: 1.54±0.25, iSPNs: 1.35±0.29 nA)(**Fig. 3.4c**). Synapses onto GP-FC neurons from dSPNs and iSPNs in dorsal striatum also displayed different short-term plasticity as reported by paired-pulse ratios (PPR), showing depression and facilitation, respectively, at short latencies (PPR at 25 ms ISI: dSPNs 0.59±0.05, iSPNs 1.01±0.06; PPR at 50 ms ISI: dSPNs 1.03±0.08, iSPNs 1.37±0.04, n=15-23 cells). Together these results indicate that GP-FC cells are functionally integrated into BG circuitry through direct, indirect and "hyperdirect" (STN-GP)(Albin et al. 1989; Nambu et al. 2002; Weiner et al. 1990; Alexander & Crutcher 1990; Graybiel 1990; Chevalier & Deniau 1990; Parent 1990; DeLong 1990; Parent & Hazrati 1995) pathways. Although iSPNs and dSPNs both inhibit GP-FC cells, differences in synaptic strength and short-term plasticity suggest that ongoing activity in each pathway could differentially inhibit the GP-FC projection.

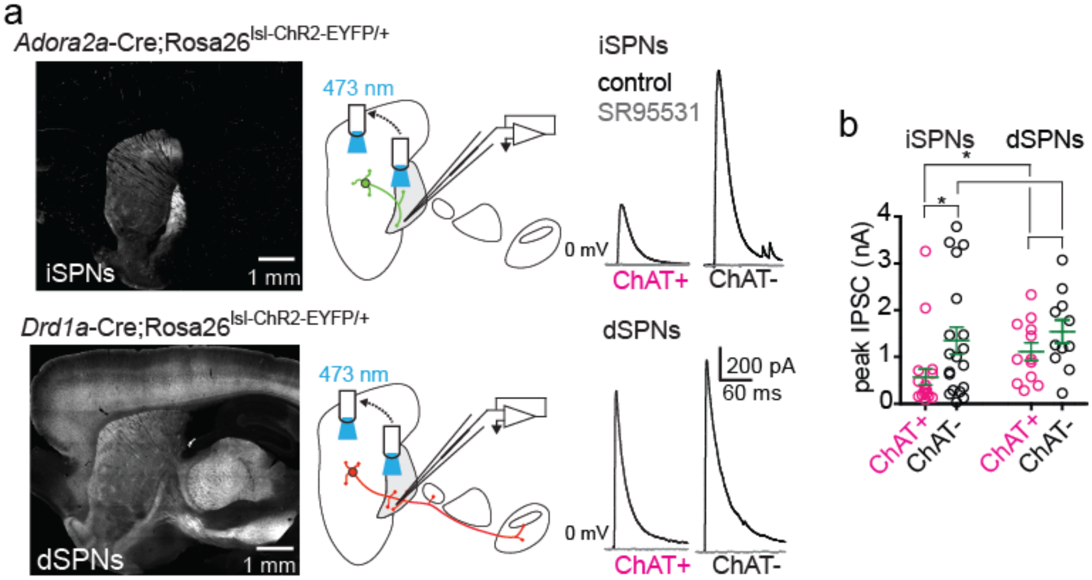

Figure 3.4 GP Projection cells are part of the basal ganglia

Figure 3.4 (continued): GP Projection cells are part of the basal ganglia

(A) *Left,* sagittal sections from an *Adora2a*-Cre;Rosa26$^{\text{lsl-ChR2-EYFP/+}}$ mouse (*top*) or *Drd1a*-Cre; Rosa26$^{\text{lsl-ChR2-EYFP/+}}$mouse (*bottom*) where ChR2-EYFP is expressed in either iSPNs or dSPNs, respectively. *Middle*, schematic of experimental strategy to study connectivity and properties of iSPN or dSPN synapses onto GP-FC cells using whole-cell voltage-clamp recording. First, a standardized light pulse (1 ms; 1.3 mW·mm^{-2}) was delivered over the recorded cell. Second, the objective was moved into dorsal striatum and light power adjusted (0.5–1 ms; 0.06 –4.4 mW·mm^{-2}) for ~200 pA first-peak paired-pulse and pharmacology experiments. *Top right*, optogenetic activation of iSPN (*top*) or dSPN (*bottom*) axons evoked outward currents from ChAT+ and ChAT- cells held at 0 mV under baseline conditions (black; NBQX, CPP, scopolamine, CGP55845 & AM251) which were blocked by bath application of SR95531 (gray).
(B) Peak IPSCs evoked from iSPN or dSPN optogenetic activation over the recorded GP-FC cell. iSPN activation evokes larger peak IPSCs onto ChAT- (n=19) vs. ChAT+ (n=20) cells, while dSPN evoked comparable IPSCs onto ChAT- (n=11) vs. ChAT+ (n=12) cells. ChAT- cells have similar peak IPSCs from dSPN and iSPN activation, while peak IPSCs from dSPN activation is larger onto ChAT+ cells than iSPN activation. Asterisk, $P<0.05$ (Mann-Whitney). Bars denote mean±s.e.m

3.3.4 GP-FC cells in vivo

To test the role of the ChAT+ GP-FC cells *in vivo* we injected ChAT-i-Cre mice with cre dependent rAAVs to express ChR2 in only the ChAT+ population. These mice were trained to be head restrained and had the opportunity to press a lever for a water reward as in our previous study (**Chapter 2**). Extracellular recordings were made from the FC of mice while the GP was directly activated via a chronically implanted fiberoptic. As GP ChAT+ cells do not project to the SNr or thalamus it is unlikely that the effects of this stimulation will engage the canonical circuitry of the basal ganglia. A 3 second 10Hz train of 473nm Light increased firing rates in some FC cells (15/106 units increased, mean with stimulation 145±14% of the firing without stim; 2/106 decreased, mean 71±0.2%; **Fig. 3.5a**), but not in mice injected with mCherry rAAV (0/73 units increased, **Fig. 3.5b**). GP ChAT activation did not consistently modulate activity associated with tones or lever presses. Nonetheless, all analysis was restricted to periods where no lever presses were detected within ±3 seconds from the light onset. Individual FC neuron's responses varied considerably (range 45 - 311%), but was in general activating (ChAT+ DIO-ChR2 population: 112±3% vs ChAT+ DIO-mCherry 96±2% $P<0.0001$ Kruskal-Wallis with

Dunn's Multiple Comparison Test, **Fig 3.5d,e**). Although some units maintained consistent increase throughout the duration of the 3s train (**Fig3.5a**), many units only responded for the first 1-2 seconds and the population returned to baseline by 2s (**Fig 3.5d**). No association between unit depth or positioning and degree of modulation was detected. These data indicate that the GP-FC ChAT+ neurons are functionally connected and relevant *in vivo.* Consistent with the physiology in slice (**Fig 3.3e**) we see a general disinhibiiton of the majority of neurons in FC, indicating that despite being a sparse projection these cells may have broad effects.

Given the spontaneous activity of the GP ChAT+, we next asked if their ongoing activity had a tonic effect on FC. We injected DIO-ArchT, a yellow-light activated inhibiting opsin into ChAT-i-Cre mice and recorded in FC as before. ArchT Activation, with 3s of 3mW 589nm Light, inhibited the firing of some FC units (3/27 units decreased, mean 79±1%; **Fig 3.5c,f**). However, at the population level there was no significant difference in mice transfected with DIO-ArchT as Controls (DIO-ArchT 94±2% vs DIO-mCherry 96±2%, p>0.05 Kruskal-Wallis with Dunn's Multiple Comparison Test). Nonetheless, Significantly modulated units were observed at a higher than predicted rate (3/27 (11%) DIO-ArchT units vs 2/73 (2.7%) DIO-mCherry units). Given the inherent difficulties in shutting down activity of an entire nucleus, it is not unexpected that the effects with DIO-ArchT would be less than that of DIO-ChR2.

Unfortunately, the ChAT- population of GP cells project to downstream nuclei, including the SNr and thalamus, as well as directly to FC. Direct stimulation of the somata of these cells would confound effects of direct GP-FC signaling as well as signaling through the entire basal ganglia loop. Even with the ChAT+ fiber stimulation there is a risk that collateral activation could engage more indirect basal ganglia circuitry. As such we used an optrode, a multielectrode array attached to a fiber optic, to directly stimulate the terminals of the GP-FC projection neurons. DIO-ChR2 was injected selectively into the GP of VGAT-Cre mice, to access both ChAT+ and ChAT- populations. As before, 3s trains of 5ms pulses at

Figure 3.5. ChAT+ cells increase firing rates in Frontal Cortex *in vivo*

(A-C) Example extracellular recordings from FC during GP optogenetic activation (**A**), or inhibition (**C**) of ChAT+ cells compared to non-opsin containing controls (**B**). ChAT-i-Cre injected with DIO-ChR2 (**A**), DIO-mCherry (**B**), or DIO-ArchT (**C**) rAAV. (**A-B**) illumination with 5ms pulses at 10Hz of 5mW of 473nm Light for 3s with a 6s inter trial interval, or (**C**) 3s constant 3mW 589nm Light 6s inter trial interval starting at 0s. Raster plot (*top*) and Histogram (*bottom*) includes only trials where no lever presses were detected from 3s prior to 3s after light onset.

(**D-F**) *top,* summary of all units in each condition normalized to the 1.5s prior to light onset and averaged, Grey bars are ± SEM. Blue or Yellow bar indicates period when optogenetic stimulation is active. *Middle,* All units normalized and plotted in order of the magnitude of their modulation. *bottom,* Histogram of the index of modulation of each unit. Index is based on the Firing Rate (FR) of cells during the entire light on period, it is calculated as $(FR_{ON}-FR_{OFF})/(FR_{ON}+FR_{OFF})$. Red bars indicate cells that were statistically significantly modulated on the trial by trial basis, Students T test $p<0.05$.

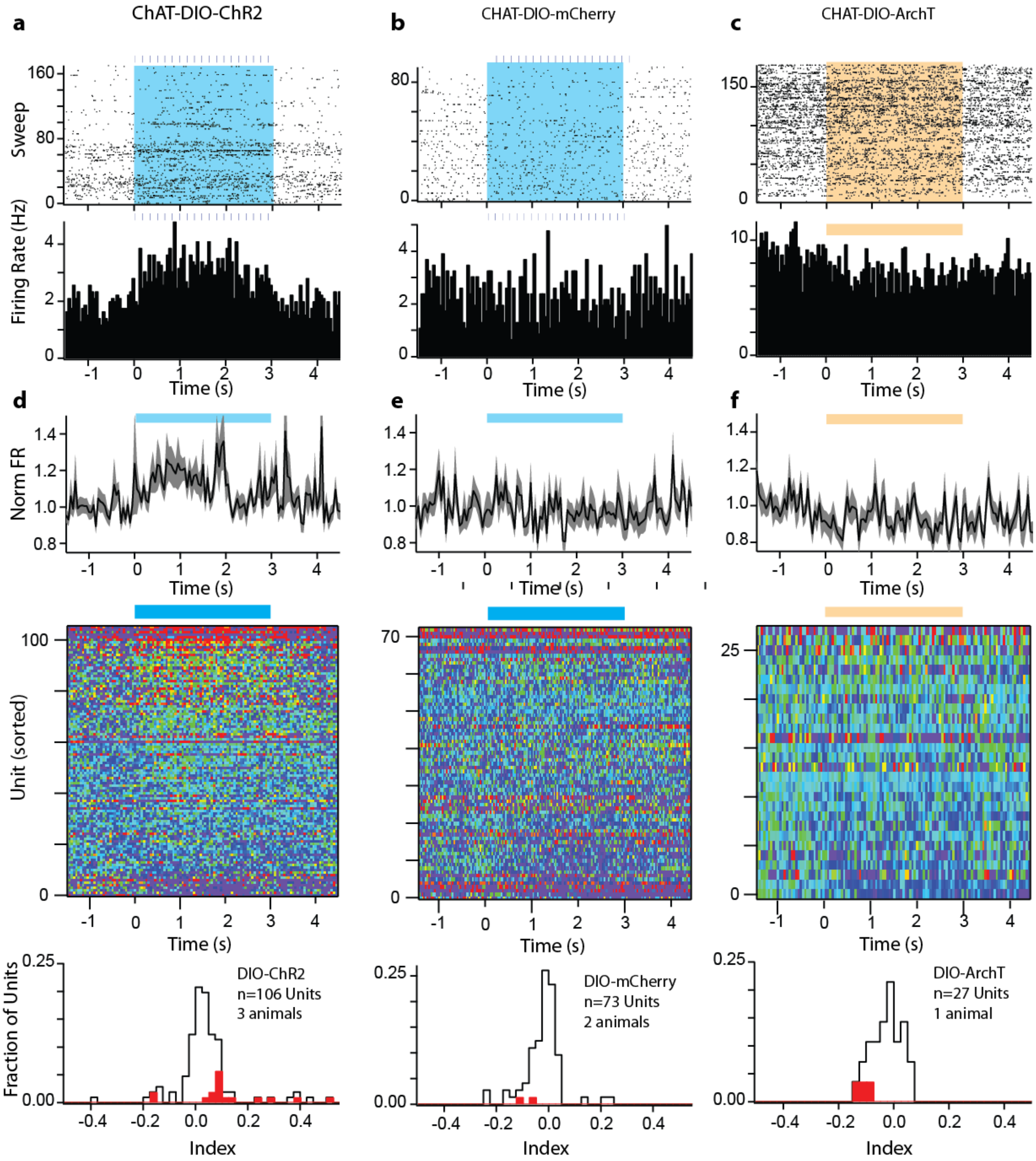

Figure 3.5 (Continued) ChAT+ cells increase firing rates in Frontal Cortex *in vivo*

10Hz were used but as terminals are harder to drive we increased the power to 10mW. Inhibited FC units were observed; inhibition peaked around 1-2s and was small in magnitude (85±3% FR with stimulation to without stim, **Fig 3.6a**).

High intensity optrode stimulation did create light mediated artifacts in both experimental and wildtype (WT) virally injected mice (note the periodicity in the variance with light **Fig 3.6b,c**), but did not affect mean firing rate in the control mice. It is possible that the low frequency component of the light-artifacts could subtly increase or decrease firing rates by pushing small units above or below the threshold of detection, or block the effects of stimulation if the happened very shortly after the light pulse.

Across the population, FC units were moderately inhibited the GP-FC projection (95±2% VGAT-DIO-ChR2 vs 101±3% WT-DIO-ChR2, $p<0.05$ Mann-Whitney Test; **Fig3.6b,c**). Thus, of the overall projections direct effects are net inhibitory on the frontal cortex. It is reasonable to assume, based on the depths of the units recorded, that the majority of observable units are from the Layer 5 region, this is also the section of frontal cortex that receives the majority of inhibitory input. This would however indicate that the ChAT- population overwhelms the effects of the ChAT+ cells. Thus the role of the ChAT+ cells in the GP is likely to be modulatory effecting interneurons in a complex way.

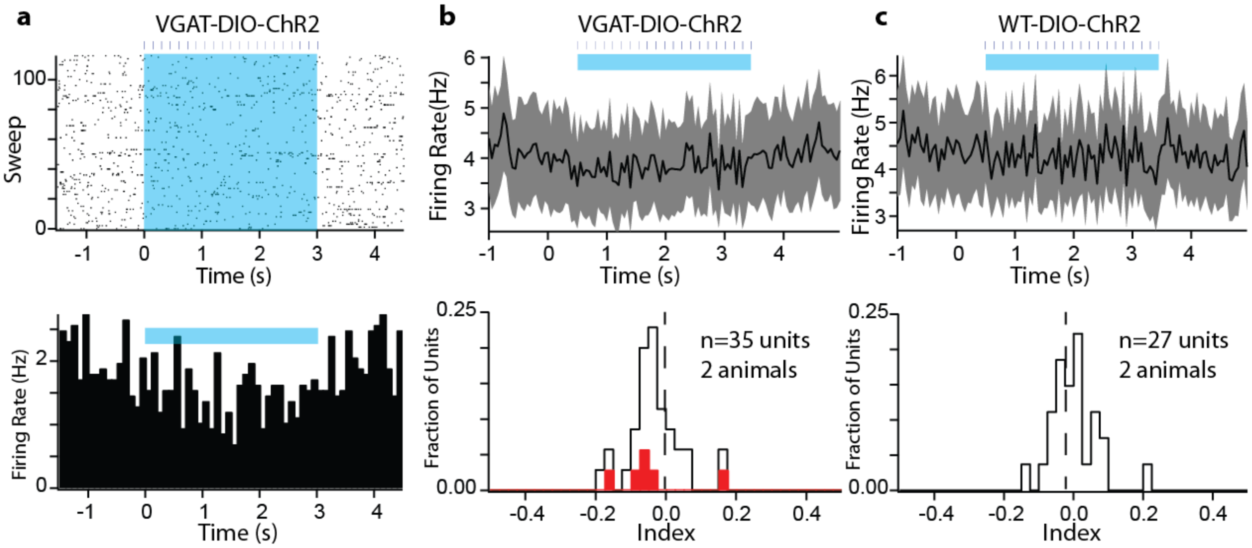

Figure 3.6. Optrode stimulation of VGAT-ChR2 GP-FC cells

(A) Representative image of a FC unit inhibited by local optrode stimulation of fibers from a DIO-ChR2 injected VGAT-Cre mouse. Raster plot (*top*) shows recordings from each individual sweep of a single unit where a press was not observed ±3s from the onset of a 3s 10Hz train of 5ms pulses with 10mW 589nm light. It is summarized in the histogram (*bottom*).

(B-C) Mean ± SEM of the firing rates of all recorded cells during light modulation is presented in VGAT-Cre (**B**) or WT control (**C**) animals (*top)*. Blue bars indicate the duration of optogenetic stimulation. *(bottom*) Histogram displays the Index of modulation of individual units to optogenetic stimulation, red units are statistically significantly modulated (p<0.05 students T Test). Dotted line represents Index of 0 or no change in firing rate to this stimulation.

3.3.5 GP-FC Contributions to the canonical output of basal ganglia

Given the involvement of the GP-FC projection neurons in the basal ganglia we next asked what the effects of iSPN and dSPN activity was in FC *in vivo*. Our previous study (**Chapter 2)** established that primary motor cortex (M1) received strong bidirectional input from iSPNs and dSPNs, presumably through their canonical output to thalamus. Specifically, GPe and SNr project to the Ventral Lateral (VL) portion of the thalamus, as well as to the Mediodorsal (MD) nucleus of the thalamus. The VL in turn projects to M1 with only very minor projections to FC, while the MD excludes M1 projecting selectively to FC (Allen Brain Atlas, (Oh et al. 2014)). While differences between the effects of M1 could be attributed to the path through MD or GP-FC projections, its necessary to understand these differences to properly design future experiments.

Recordings were made from FC using multichannel extracellular recordings during striatal stimulation of iSPN (adora-cre) or dSPN (drd1a(EY217)-cre) mice injected with DIO-ChR2. These recordings were made simultaneously with the recordings in Motor cortex (M1) described in **Chapter 2**. Several interesting differences were observed in the response to iSPN and dSPN activation in FC vs M1. The EY217 variant of the drd1a-Cre used throughout **Chapter 2** differs from the variant used in the rest of **Chapter 3**. It is better excluded from the cortex, but appears to be less penetrant of ventral and medial striatum. Anecdotal evidence suggests the EY217-Cre dSPNs have weaker innervation of the GP-FC cells, although this has not been looked at systematically.

We began by investigating the role of the iSPNs on cortical firing. Similar to M1 iSPN activation decreased firing in the majority of FC units (**Fig 3.7a,c**). However, the modulation had some notable differences: the transient increase in firing at the onset of light that was present in some shallow cells (**Fig 2.4, 3.7a**) was absent in frontal cortex, there was no depth dependence on the degree of modulation. Fewer cells were modulated in FC than in M1 (FC 27/76 35% vs M1: 136/193 70%, $p<0.01$ Fisher's Exact Test), but this modulation was slightly faster than inhibited M1 cells, on par with transiently excited M1 cells (FC inhibition 138±21 ms vs. M1 inhibition 169±22ms vs. M1 transient excitation 140±11ms; all n.s. Kruskal-Wallis test, **Fig 3.7d**). Despite the similarity in timing of the FC effects and the transiently excited M1 cells, it is unlikely that they represent the same projection, as they have opposite signs. Still this may suggest that both these projections take one less synapse on their way to cortex, as they are both faster than the canonical path by a similar amount.

Lastly we examined the effects of dSPN activation on frontal cortex. In contrast to M1 dSPN activation inhibited some FCs despite being predominately excitatory (**Fig 3.7b,e**). Most cells that were excited were only excited briefly, although cells with sustained elevated firing rates were present. This breif excitation typically lasted <500ms but lasted longer than the transient excitation of M1 by the iSPN. As it is unlikely that the EY217 varient of the D1-Cre projects directly to the GP it is most likely that the differences between FC and M1 are due to the different thalamic projections and not the GP-FC route. Separate loops exist between different regions of the cortex, with MD projecting primarily to FC while VA/VL project to the Motor cortex. With this mechanism in mind we can conclude that many BG loops are involved in similar but not identical actions. The GP-FC loop may contribute to the modulation of each of these paths.

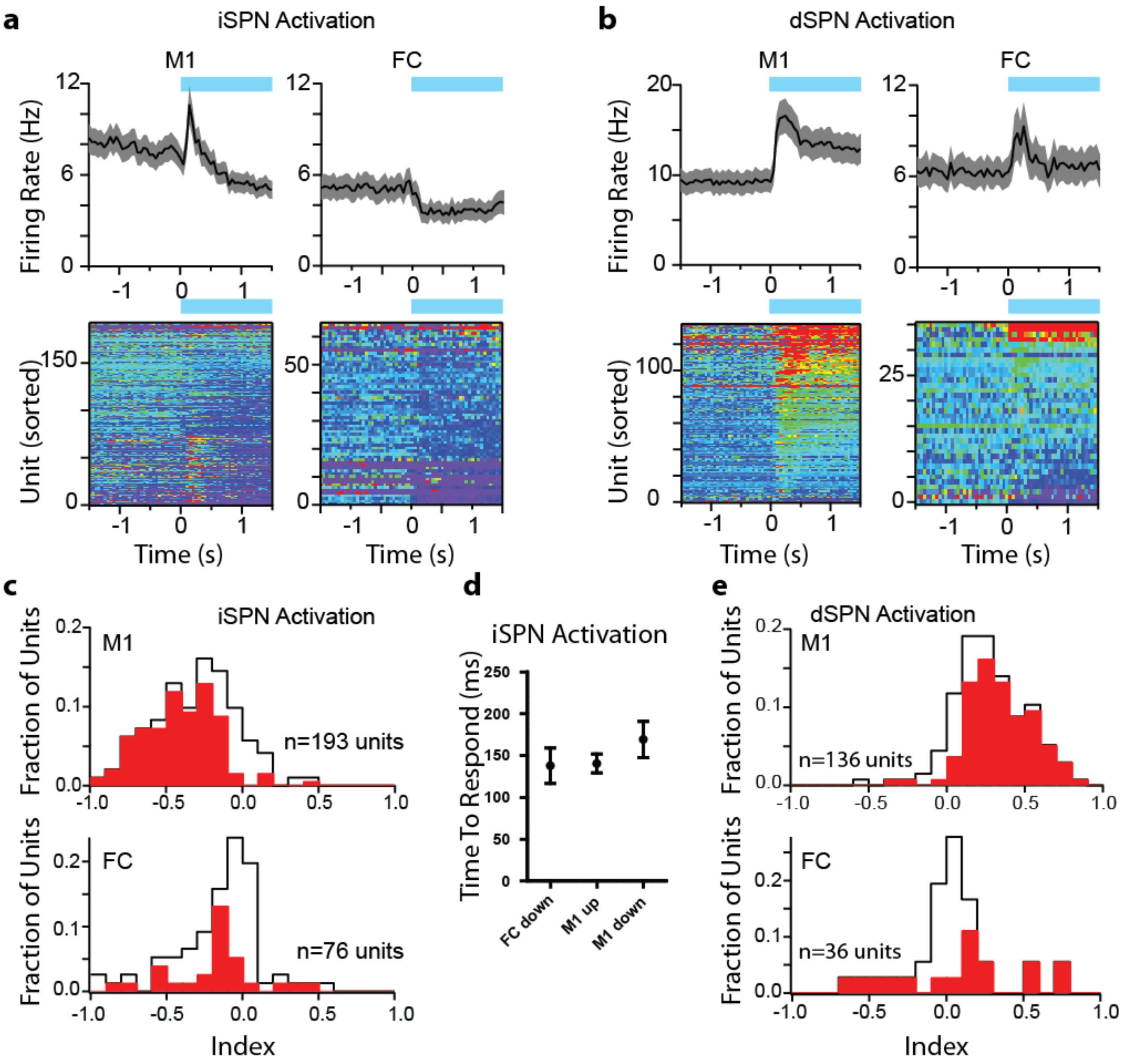

Figure 3.7. Comparison of iSPN and dSPN activation in M1 or FC

(A-B) *top,* mean ± SEM firing rate of all cortical cells during iSPN (A) or dSPN (B) stimulation in M1 motor cortex (*left*) or frontal cortex, FC, (*Right*). Blue bar indicates period of constant striatal illumination, only trials where the animal did not press a lever are included in this analysis. *Bottom,* all units are presented normalized and sorted by the magnitude of their modulation.

(C,E) Light modulation index histogram of all units recorded in M1 (*top*) or FC (*bottom*) during iSPN (C) or dSPN (E) stimulation. Index is calculated based on Firing Rate (FR) as Index = $(FR_{ON}-FR_{OFF})/(FR_{ON}+FR_{OFF})$

(D) Time to light modulation, up or down, for indirect pathway activation. Each unit's time to respond is calculated as the first bin after light onset that is >±2 SD from the baseline, 1.5s pre light period. All M1 Data is also displayed in **Chapter 2**.

3.4 Discussion

The presence of a GABAergic output to cortex under control of striatal SPNs could be important for understanding the etiology and treatment of motor and psychiatric diseases that affect BG circuitry(Haber 2003; Albin et al. 1989). One example is schizophrenia, which often presents in late adolescence, a period associated with dynamic developmental changes of inhibitory circuits in prefrontal cortex(Freeze et al. 2013; Kimura et al. 1984; Kravitz et al. 2010). Mounting evidence suggests that overactive dopamine signaling in the striatum may play an important part in the disease(Graybiel et al. 1994; Oldenburg & Ding 2011). A cornerstone of this theory is the mechanism of action of antipsychotic drugs, which relieve hallucinations and delusions by blocking D2rs(DeLong 1990; Higley et al. 2011; Albin et al. 1989). Schizophrenics exhibit imbalances in both GABA(Gerfen et al. 1990; Haber et al. 1985) and ACh(Cazorla et al. 2014; Tepper & Bolam 2004; Kawaguchi et al. 1990) neurotransmitter systems, as well as marked changes in morphology and gene expression of cortical interneurons(Smith & Bolam 1991; Marsden 1982). Since GP-FC cells are active *in vivo* (**Fig 3.5, 3.6**), release GABA and ACh onto interneurons in FC (**Fig. 3.3**), and are inhibited by D2r-expressing iSPNs (**Fig. 3.4**), we propose that they may be critically involved in the pathogenesis of schizophrenia.

The circuit function of GP-FC cells suggests a major revision to accepted models of subcortical-cortical feedback circuitry. Within the BG, the direct and indirect pathways are thought to exert opposite effects on cortical activity through bidirectional control of thalamic activity(Deniau & Chevalier 1985; Albin et al. 1989; Alexander & Crutcher 1990; Graybiel 1990; Chevalier & Deniau 1990; Parent 1990; DeLong 1990; Parent & Hazrati 1995). The GP-FC projection permits the BG to bypass thalamus and directly control cortical states. ChAT- GP-FC cells release GABA predominantly onto layer 5 pyramidal neurons and interneurons across layers, suggesting inhibitory and dis-inhibitory ionotropic effects on microcircuits. ChAT+ GP-FC cells likely have a mixed excitatory and inhibitory effect on cortical microcircuits by releasing both GABA and ACh onto interneurons. Furthermore, GABA co-release may be widespread in the basal forebrain cholinergic system and an important feature of subcortical regulation of behavioral state and cortical plasticity. In contrast to their opposing effects on thalamic output, the direct and indirect pathways both inhibit the GP-FC projection. Conversely, the hyperdirect pathway through the STN excites both thalamus via the SNr(Gerfen et al. 1982; Smith & Bolam 1989; Kawaguchi et al. 1990; Kelly & Strick 2004) and GP-FC neurons directly. This connectivity suggests that as cortical information enters the BG, the activity of each internal BG pathway will recruit the thalamic and cortical outputs differently, imposing distinct feedback effects across cortical areas in order to control behavior.

3.5 Materials and Methods

Mice. Bacterial artificial chromosome (BAC) transgenic mice expressing EGFP under control of the dopamine 2 receptor locus (*Drd2*-EGFP) were used to define the anatomical border of the globus pallidus externus (GP) and ventral pallidum (VP) through the expression of EGFP in striatal iSPNs (GENSAT, founder line S118). Cre recombinase was targeted to specific cell types of the basal ganglia using knock-in or BAC transgenic mice to drive Cre expression under gene-specific regulatory elements. Cre knock-in mice for *choline acetyltransferase* (*ChAT*)(Kravitz et al. 2010; Graybiel et al. 1994; Bateup et al. 2010) and *Slc32a1* (vesicular GABA transporter or *Vgat*)(Freeze et al. 2013; DeLong 1990; Albin et al. 1989) were generously provided by Brad Lowell (Beth Israel Deaconess Medical Center) and are available from the Jackson Labs (*ChAT*$^{\text{i-Cre}}$, stock #006410; *Vgat*$^{\text{i-Cre}}$, stock #016962). All knock-in mice link Cre expression to the gene of interest using an internal ribosome entry site. Targeting Cre expression in dSPNs was achieved with BAC transgenic mice expressing Cre under control of the dopamine receptor 1 (*Drd1a*) or in iSPNs with Cre under control of the adenosine 2A receptor (*Adora2a*) or dopamine receptor 2 (*Drd2*) regulatory elements and obtained from GENSAT (*Drd1a*-Cre, founder EY262, stock

#017264-UCD; *Adora2a*-Cre, founder KG139, stock # 031168-UCD; *Drd2*-Cre, founder ER43, stock #017268-UCD). A second Drd1a-cre was used in some *in vivo* experiments, referred to as EY217 variant (*Drd1a-Cre,* founder EY217, STOCK Tg(Drd1a-cre)EY217Gsat/Mmucd). To visualize the full processes of Cre expressing cells, Cre mice were bred to Cre-dependent TdTomato reporter allele(Mahon et al. 2006; Gerfen et al. 1990; Spampinato et al. 1986) (Ai14; Jackson Labs, stock # 007914; referred to as Rosa26$^{\text{lsl-tdTomato}}$). To visualize the somata of Cre expressing cells, the Cre-dependent ZsGreen reporter allele was used (Ai6; Jackson Labs, stock # 007906; referred to Rosa26$^{\text{lsl-zsGreen}}$). To target channelrhodopsin-2 (ChR2) to all Cre expressing cells, Cre driver mice were bred to a Cre-dependent ChR2(H134R)-EYFP transgene(Histed et al. 2012; Cazorla et al. 2014; Kawaguchi et al. 1990)(Ai32; Jackson Labs, stock #012569; referred to as Rosa26$^{\text{lsl-ChR2-EYFP}}$). Conditional knockout of *Slc32a1* (*Vgat*) was achieved by introgressing a *Slc32a* allele(Wilson & Groves 1980; Smith & Bolam 1991; Kozorovitskiy et al. 2012) where the second exon is flanked by loxp sites (Jackson Labs, stock# 012897;referred to as *Vgat*$^{fl/fl}$) into *ChAT* $^{\text{i-Cre}}$;Rosa26$^{\text{lsl-ChR2-EYFP}}$ mice. In experiments designed to identify cortical cells neighboring ChR2^{+} ChAT+ or ChAT- GP-FC axons as pyramids or interneurons, *ChAT* $^{\text{i-Cre}}$ mice also carried a GAD67$^{\text{GFP}}$ knock-in allele(Taverna et al. 2008; Deniau & Chevalier 1985; Alexander & Crutcher 1990) to highlight a subset of cortical interneurons synthesizing GABA. Wild type mice refer to C57BL/6 obtained from Charles River. Transgenic mice were of a mixed genetic background. All experimental manipulations were performed in accordance with protocols approved by the Harvard Standing Committee on Animal Care following guidelines described in the US National Institutes of Health *Guide for the Care and Use of Laboratory Animals*.

Virus Preparation. Cre-On or Cre-Off conditional expression was achieved using recombinant adeno-associated virus (rAAV) carry transgenic cassettes whose transcription was activated or inactivated by Cre (Kravitz et al. 2010; Gerfen et al. 1982; Smith & Bolam 1989; Kawaguchi et al. 1990; Kelly & Strick

2004). Cre-On conditional expression of channelrhodopsin-2 (ChR2-mCherry, H134R variant), EGFP, mCherry, or Synaptophysin-mCherry was achieved by using a double-floxed inverted open reading frame (DIO). Cre-Off conditional expression of ChR2-mCherry was achieved by starting the open reading frame in the non-inverted orientation with respect to the promoter (DO). To achieve simultaneous Cre-On EGFP and Cre-Off tdTomato labeling, DIO-EGFP was mixed 1:1 with FAS-tdTomato, an alternative Cre-Off rAAV backbone that achieves Cre-Off expression through excision of the open reading frame using alternative loxp sites(Kravitz et al. 2010; Bateup et al. 2010). DIO, DO, and FAS rAAVs all use the EF1a promoter and were packaged in serotype 8 by a commercial vector core facility (University of North Carolina). All rAAVs were stored in undiluted aliquots at a concentration >10^{12} genomic copies per ml at −80°C until intracranial injection.

***Stereotaxic intracranial injections*.** Male and female mice (postnatal day 20–120) were anesthetized with isoflurane and placed in a small animal stereotaxic frame (David Kopf Instruments). Under aseptic conditions, the skull was exposed and a small hole was drilled. For rAAVs injections, 200-350 nl total volume was delivered bilaterally into the ventral GP/dorsal NB or 500 nl into dorsal striatum through a pulled glass pipette at a rate of 200 $\text{nl}\cdot\text{min}^{-1}$ using a Microinject system (World Precision Instruments). GP injection coordinates were 0.7 mm posterior from Bregma, 2.0 mm lateral and 3.8 mm below the pia. Dorsal striatum injection coordinates were 0.9 mm anterior from Bregma, 2.2 mm lateral and 2.5 mm below the pia. After surgical procedures, mice received flunixin for analgesia and were returned to their home cage for >21 days to allow for maximal gene expression. To identify GP neurons that project to frontal cortex, 200 nl of fluorescent retro beads (Red-1X or Green, Lumafluor) were injected into frontal (anterior to striatum) cortical areas including secondary motor (M2), primary motor (M1), primary somatosensory (S1) and dorsal and ventral agranular insular (AID and AIV) cortices. Frontal cortex injection coordinates were 1.9 mm anterior from Bregma, 1.8 mm lateral and 2 mm below the pia. Following surgery, mice received flunixin and were returned to their home cage for 3-9 days before experimentation. Stereotaxic coordinates were adjusted slightly by age.

In vivo recordings. At least 1 week after the initial injections, mice were surgically implanted with a permanent titanium headpost. In this surgery the coordinates for GP, FC, and M1 were marked on the surface of the skull based on stereotaxic coordinates. The headpost was secured and the animal's skull was covered with C&B metabond (Parkell Inc). Animals subsequently singly housed and allowed to recover for 1 week before habituation to restraint.

Mice were water restricted (to 80% of their free feeding weight) and habituated to restraint in a custom-made lever-press training rig. This rig allows the animal to press a lever in response to an auditory cue, designed for a previous study (**Chapter 2**). Animals were trained for increasing durations for at least 3 days until they were able to tolerate headrestraint for 90 min without struggling. In this time animals achieved an intermediate level of performance on the task, where they knew the association between lever press and reward, but were not proficient at recognizing and responding to tones.

One day before the first recording day animals were anesthetized with isoflurane and received a craniotomy over the region of interest. In this surgery, if necessary, a chronic fiber (62.5μm core multimode fiber (ecablemart.com) attached to a ceramic LC ferrule (Pfp inc)) was implanted at the same coordinates as the GP viral injection, but at depth 3.0mm. All Chronic fibers were prescreened to have >80% transmission at 473nm light. A ceramic ferrule connecter linked the chronic fiber to a standard LC cable. Light shuttering and output control was through a Acusto optic modulator (AA systems) and had >1000:1 occlusion ratio.

Recordings were made using 16 or 32 channel silicone probes with 177μm^2 recording sites (Neuronexus Technologies) spaced 50μm apart and lowered to a depth of ~1000μm below the surface of the brain. Optrode recordings were made with a 16 channel probe of the same configuration fitted with a fiberoptic 100µm above the top recording site (Neuronexus Technologies, OA series). All *in vivo* electrophysiology was acquired using the omniplex system (Plexon Inc) and filtered at 300-8KHz. Spike detection was done by level crossing generally at 50µV and clustering to remove the noise cluster using offline sorter (plexon Inc). Units that were separable were counted separately, but many units were accepted as multi-unit. All analysis here assumes each unit as a possible multi-unit and is only separated when necessary. All analysis was performed using custom scripts in igor Pro and etch-a-sketch. Data visualization and statistical analysis was done using Igor Pro and GraphPad Prism.

Fixed Tissue Preparation and Imaging. Mice were deeply anesthetized with isoflurane and transcardially perfused with 4% paraformaldehyde (PFA) in 0.1 M sodium phosphate buffer (1x PBS). Brains were post-fixed for 1–3 days, washed in 1x PBS and sectioned (40 mm) coronally, sagittally, or horizontally using a Vibratome (Leica). Slices were then immunostained (see **Immunohistochemistry**) or mounted on slides (Super Frost). After drying, slices were coverslipped with ProLong antifade mounting media containing DAPI (Molecular Probes) and imaged with an Olympus VS110 slide scanning microscope using the 10x objective. Fluorescent proteins introduced through rAAVs or transgenic alleles were never immunoenhanced. Confocal images (1-2 mm optical sections) were acquired with an Olympus FV1000 laser scanning confocal microscope (Harvard Neurobiology Imaging Facility) through a 63x objective.

Immunohistochemistry. Immunohistochemistry conditions were the same for both mouse and macaque sections. For ChAT immunohistochemistry, slices were incubated in a 1x PBS blocking solution containing 5% normal horse serum and 0.3% Triton X-100 for 1 hour at room temperature. Slices were then incubated overnight at 4^{o}C in the same solution containing anti-choline acetyltransferase antibody

(1:100, Millipore AB144P). The next morning, sections were washed three times for five minutes in 1x PBS for and then incubated for 1 hour at room temperature in the blocking solution containing donkey anti-goat Alexa 647 or Alexa 488 (1:500, Molecular Probes). For macaque sections, streptavidin conjugated to Alexa 350 or Alexa 488 (1:1000, Molecular Probes) was also included in the secondary reaction. The same protocol was used for NeuN (1:100, Millipore MAB377) and Parvalbumin (1:7500, Swant PV235) immunostaining with anti-mouse Alexa 647 secondary antibodies (1:500, Molecular Probes). Immunostained mouse sections were mounted and imaged as described above. Immunostained *macaque* sections were mounted as described below.

Slice preparation. Acute brain slices were obtained from mice using standard techniques. Mice were anesthetized by isoflurane inhalation and perfused through the heart with ice-cold artificial cerebrospinal fluid (ACSF) containing (in mM) 125 NaCl, 2.5 KCl, 25 $NaHCO_3$, 2 $CaCl_2$, 1 $MgCl_2$, 1.25 NaH_2PO_4 and 11 glucose (~308 $mOsm \cdot kg^{-1}$). Cerebral hemispheres were removed, placed in ice-cold choline-based cutting solution (consisting of (in mM): 110 choline chloride, 25 $NaHCO_3$, 2.5 KCl, 7 $MgCl_2$, 0.5 $CaCl_2$, 1.25 NaH_2PO_4, 25 glucose, 11.6 ascorbic acid, and 3.1 pyruvic acid), blocked and transferred into a slicing chamber containing ice-cold choline-based cutting solution. Sagittal slices (350 mm thick) were cut with a Leica VT1000s vibratome and transferred to a holding chamber containing ACSF at 34°C for 30 minutes and then subsequently at room temperature. Both cutting solution and ACSF were constantly bubbled with 95% O_2/5% CO_2. In a subset of experiments, acute brain slices were cut in ice-cold ACSF.

Acute slice electrophysiology and two-photon imaging. Individual slices were transferred to a recording chamber mounted on a custom built two-photon laser scanning microscope (Olympus BX51WI) equipped for whole-cell patch-recordings and optogenetic stimulation. Slices were continuously superfused (3.5–4.5 $ml \cdot min^{-1}$) with ACSF warmed to 32–34°C by through a feedback-controlled heater

(TC-324B; Warner Instruments). Cells were visualized through a water-immersion 60x objective using differential interference contrast (DIC) illumination. Epifluorescence illumination was used to identify those cells labeled by fluorescent microspheres and/ or expressing fluorescent genetic markers. Patch pipettes (2–4 MW) pulled from borosilicate glass (G150F-3, Warner Instruments) were filled either with a Cs^+-based low Cl^- internal solution containing (in mM) 135 $CsMeSO_3$, 10 HEPES, 1 EGTA, 3.3 QX-314 (Cl^- salt), 4 Mg-ATP, 0.3 Na-GTP, 8 Na_2-Phosphocreatine (pH 7.3 adjusted with CsOH; 295 $mOsm\cdot kg^{-1}$) for voltage-clamp recordings, or with a K^+-based low Cl^- internal solution composed of (in mM) 135 $KMeSO_3$, 3 KCl, 10 HEPES, 1 EGTA, 0.1 $CaCl_2$, 4 Mg-ATP, 0.3 Na-GTP, 8 Na_2-Phosphocreatine (pH 7.3 adjusted with KOH; 295 $mOsm\cdot kg^{-1}$) for current-clamp recordings. Alexa Fluor 594 (20 µM) was added to the both internals. Series resistance (<25 MΩ) was measured with a 5 mV hyperpolarizing pulse in voltage-clamp and left uncompensated. Membrane potentials were corrected for a ~7 mV liquid junction potential. After the recording was complete, cellular morphology was captured in a volume stack using 740 nm two-photon laser light (Coherent). All recorded GP-FC neurons were labeled with microspheres following injection in frontal cortex. In experiments where ChAT expression was not marked fluorescently, ChAT+ or ChAT- GP-FC neurons were distinguished based on soma size and spontaneous firing rate in cell attached mode. Cortical neurons were classified as pyramids or interneurons based on dendritic morphology and $GAD67^{GFP}$ expression.

Acute slice data acquisition and analysis. Membrane currents and potentials were recorded using an Axoclamp 700B amplifier (Molecular Devices) filtered at 3 kHz and digitized at 10 kHz using National Instruments acquisition boards and a custom version of ScanImage written in MATLAB (Mathworks). Electrophysiology and imaging data were analyzed offline using Igor Pro (Wavemetrics), ImageJ (NIH) and MATLAB (Mathworks). In figures, voltage-clamp traces represent the average waveform of 3–6 acquisitions; current-clamp traces are individual acquisitions. Passive membrane properties were calculated from current deflections in voltage-clamp (V_{hold} = -70 mV). Cells were considered spontaneously active with maintained action potential firing (>20s) within 2 minutes of whole-cell break in. Average V_{rest} was calculated for non-spontaneously active cells 1-3 minutes after break in. Peak amplitudes were calculated by averaging over a 1 ms window around the peak. AMPAR and NMDAR currents were isolated from the stimulation artifact by subtracting the NBQX resistant component (V_{hold} = -70 mV) followed by the CPP/NBQX resistant component (V_{hold} = +40 mV) following a 3 minute wash-in period from current averages consisting of 10-15 consecutive acquisitions (20 s inter-stimulus interval). For pharmacological analyses current averages were calculated from 15 consecutive acquisitions (20 s inter-stimulus interval) before and after a 3 minute wash-in period and then normalized to averages corresponding to the same time with no drug flow in. For pharmacological analyses in **Figs. 3.3c** 3-7 consecutive acquisitions (20 s inter-stimulus interval) were averaged following a 3 minute wash-in period for NBQX and CPP or a 4 minute wash-in period for MEC, MLA, and DHβE. For TTX and 4AP conditions, current averages were composed of the acquisitions following full block or first-recovery of ChR2 evoked currents, respectively. Data (reported in text and figures as mean ± s.e.m.) were compared statistically using the following Mann-Whitney test or Fisher's Exact test. *P* values smaller than 0.05 were considered statistically significant.

Optogenetic and electrical stimulation**.** To activate ChR2 in acute slices, 473 nm laser light (Optoengine) was focused onto the back aperture of the 60x water immersion objective to produce collimated whole-field illumination. Square pulses of laser light were delivered every 20 seconds and power was quantified for each stimulation by measuring light diverted to a focal plane calibrated photodiode through a low-pass dichroic filter. For ChR2 activation of dSPN or iSPN inputs onto GP-FC cells (*Drd1a*-Cre;Rosa26$^{lsl\text{-}ChR2\text{-}EYFP/+}$ or *Adora-Cre*;Rosa26$^{lsl\text{-}ChR2\text{-}EYFP/+}$ mice), a consistent light stimulation (1 ms; 1.3 $mW{\cdot}mm^{-2}$) was delivered directly over the recorded cell and the resulting currents were used to compare synaptic strength across cells. For paired-pulse comparisons, the objective was moved 0.16 –

1.4 mm into dorsal striatum (median = 0.4 mm) and stimulation strength and duration (0.5–1 ms; 0.06 – 4.4 mW·mm^{-2}) were adjusted to produce 1st peak currents between 26 – 547 pA (median = 226 pA). Stronger light powers (2-7 ms;4.4 mW·mm^{-2}) were used activate ChR2 in *ChAT* $^{\text{i-Cre}}$ cells (*ChAT* $^{\text{i-Cre}}$;Rosa26$^{\text{lsl-ChR2-EYFP/+}}$ mice) in cortex. For ChR2 introduced with rAAVs, light (2 ms;1.3-4.4 mW·mm^{-2}) was used across conditions except in some cases following bath application of TTX and 4AP where increasing the power or duration of light stimulation was necessary to recover currents (for example, changing the duration from 2 to 4 ms). For electrical activation of the STN axonal projection into the GP, a bipolar tungsten electrode (TST33A10KT; World Precision Instruments) was placed at the anterior border of the STN and 0.1-0.5 ms square pulse of current was applied and power adjusted to maintain evoked currents while minimizing the stimulus artifact.

Reagents. Drugs (all from Tocris) were applied via bath perfusion: SR95531 (10 µM), tetrodotoxin (TTX; 1 µM), 4-aminopyridine (4AP; 500 µM), Scopolamine (10 µM), (2*S*)-3-[[(1*S*)-1-(3,4-Dichlorophenyl)ethyl]amino-2-hydroxypropyl](phenylmethyl)phosphinic acid (CGP 55845; 5 µM), *N*-(Piperidin-1-yl)-5-(4-iodophenyl)-1-(2,4-dichlorophenyl)-4-methyl-1*H*-pyrazole-3-carboxamide (AM-251; 10 µM), 2,3-dihydroxy-6-nitro-7-sulfamoyl-benzo(*f*)quinoxaline (NBQX; 10 µM), *R*,*S*-3-(2-carboxypiperazin-4-yl)propyl-1-phosphonic acid (CPP; 10 µM), *N*,2,3,3-Tetramethylbicyclo[2.2.1]heptan-2-amine, (MEC; 10 uM), [1α,4(*S*),6β,14α,16β]-20-Ethyl-1,6,14,16-tetramethoxy-4-[[[2-(3-methyl-2,5-dioxo-1-pyrrolidinyl)benzoyl]oxy]methyl]aconitane-7,8-diol (MLA; 0.1 uM), (2*S*,13b*S*)-2-Methoxy-2,3,5,6,8,9,10,13-octahydro-1*H*,12*H*-benzo[*i*]pyrano[3,4-*g*]indolizin-12-one (DHβE; 10 uM), (*S*)-(-)-5-Aminosulfonyl-*N*-[(1-ethyl-2-pyrrolidinyl)methyl]-2-methoxybenzamide ((-)sulpiride; 10 µM) and (4a*R*-trans)-4,4a,5,6,7,8,8a,9-Octahydro-5-propyl-1*H*-pyrazolo[3,4-*g*]quinolone ((-)Quinpirole; 8 uM). CPP and NBQX were combined to make a cocktail of antagonists to target ionotropic glutamate receptors, while MEC, MLA and DHβE were combined to make a cocktail to antagonize nicotinic receptors.

Chapter 4

Conclusions:

In this thesis we address two aspects of the canonical organization of the basal ganglia. First we directly tested the central tenants of the looped architecture model and second we describe a previously underappreciated projection from the GP to Frontal cortex. Both of these projects expand upon what is already known about the basal ganglia and provide new explanations for how this system works in the intact animal.

It has been proposed that the fundamental role of the basal ganglia is action selection (Graybiel 1998). This is an attractive model as it is easy to imagine that for any given action, there are competing motor plans that differentially activate dSPNs and iSPNs to compete to allow only the correct action. One can further imagine that the critical role of dopamine in reward in the striatum helps the SPNs sort through previous history to determine the correct course of action. If this model were correct biasing the activity of one of these pathways non-specifically, as we did in **chapter 2**, would affect all available behaviors. One would not get solely changes in the rate of directed lever presses, but changes in limb and body movements as well as other more complex behaviors such as grooming or social interactions. Interestingly, when activating dSPNs, Kravitz et al (Kravitz et al. 2010) found a decrease in grooming behavior despite an overall increase in movements. Which seemingly implies that the striatum is only involved in very basic movements. However, that group's work, as well as many others, has well established a role of the striatum in complex reward mediated behaviors (Kravitz et al. 2012). Instead perhaps the role of the striatum is more critical in the planning of motor action than in the actual execution of them. Indeed in our work, while we see strong changes in the overall firing rates of motor cortex with either pathways activation, we only see a modest change around a movement itself.

However we still see substantial differences in firing in the period leading up to the movement, especially in the case of iSPN activation. This period preceding a lever press is likely the planning phase of a movement. Further evidence for a more complex interpretation of a role of the BG lies in the time it takes for BG activation to propagate to cortex. With the mean time for a cortical unit to respond to either pathway's activation being 100-200ms there is simply not enough time to activate a cortical circuit that activates a motor plan to initiate a movement. Especially when one considers that that movement may happen, in the case of a well-trained mouse, in <150ms. We are thus left with the conclusion that either the cells that respond to the basal ganglia quickly are especially advantaged, and are presumably the output cells of the cortex, or that basal ganglia is modulating the movement related cortical activity in some ongoing sense. Again this ongoing modulation is most likely affecting the planning phase of the behavior.

One of the major findings of the first project is the asymmetry between the effects of each pathway's activation. These asymmetries might become less surprising when one divorces themself from the traditional go/no go terminology of dSPN and iSPN function. If indeed the iSPNs are not serving as a simple counterbalance to an immediate go signal, and are more akin to a 'do something else' signal as has been suggested by Berke and colleagues (Schmidt et al. 2013), then it becomes much easier to imagine that the type of effect each pathway would have to be very different. One of the key observations, that the baseline dSPN but not iSPN effect is proportional to each cortical unit's press selectivity, implies that there is not complete shuffling of information at the level of SNr or thalamus. It would be impossible to observe this effect if dSPNs and iSPNs exclusively synapsed onto the same neuron and acted in a simple push-pull manner. Instead, we must conclude that through some mechanism the input of iSPN and dSPN activity is different in these nulcei, whether that means there are cells in thalamus that are listening exclusively to dSPNs vs iSPNs or a more subtle mechanism based on the firing patterns we can’t conclude. Nonetheless, understanding how information is transmitted between the basal ganglia and thalamus will help us understand how the basal ganglia are arranged.

iSPN activation transiently increased firing in shallow cells in motor cortex. While there exists no direct projection from the GP to the cortex in the canonical model, it was hoped that the projection described in **Chapter 3** would be able to account for this transient. Unfortunately our *in vivo* attempts to replicate the transient have not been successful. Our GP-FC *in vivo* studies have shown changes in firing rate at a much slower time scale than is observed in these transients. The VGAT-ChR2 optrode experiments are able to demonstrate that stimulating the GP-FC projection produces a net inhibitory effect, in the anti-canonical direction and consistent with the anatomy. But the response latency for this pathway was very slow. Furthermore when iSPNs were activated no non-canonical transient was observed in FC. Interestingly the ChAT+ GP-FC cells despite being GABAergic appear to be net excitatory preserving the general canonical output of the GP. Future work should follow up on this non canonical output to determine what route it’s coming from.

The existence of a direct GP-FC projection is particularly interesting when put in the context of Schizophrenia. Schizophrenia is a complex neurological disorder that involves deficits in the frontal cortex, but is effectively treated by D2 antagonists. While there are D2 receptors in many regions of the brain including frontal cortex, by far the highest concentration is in striatum on the iSPNs. It is thus very convenient to find a single projection that directly links iSPNs to frontal cortex in only two synapses. Perhaps future pharmaceuticals can be designed to target only this pathway, to create new treatments for this disease.

Bibliography:

Albin, R.L., Young, A.B. & Penney, J.B., 1989. The functional anatomy of basal ganglia disorders. *Trends in Neurosciences*, 12(10), pp.366–375.

Aldridge, J.W., Anderson, R.J. & Murphy, J.T., 1980. The role of the basal ganglia in controlling a movement initiated by a visually presented cue. *Brain research*, 192(1), pp.3–16.

Alexander, G.E. & Crutcher, M.D., 1990. Functional architecture of basal ganglia circuits: neural substrates of parallel processing. *Trends in Neurosciences*, 13(7), pp.266–271.

Alexander, G.E., DeLong, M.R. & Strick, P.L., 1986. Parallel organization of functionally segregated circuits linking basal ganglia and cortex. *Annual Review of Neuroscience*, 9, pp.357–381.

Banse, K., 1990. Mermaids-Their Biology, Culture, and Demise. *Limnology and Oceanography*, 35(1), pp.148–153.

Balleine, B.W., Delgado, M.R. & Hikosaka, O., 2007. The role of the dorsal striatum in reward and decision-making. *Journal of Neuroscience*, 27(31), pp.8161–8165.

Bateup, H.S. et al., 2010. Distinct subclasses of medium spiny neurons differentially regulate striatal motor behaviors. *Proceedings of the National Academy of Sciences of the United States of America*, 107(33), pp.14845–14850.

Bayer, H.M. & Glimcher, P.W., 2005. Midbrain dopamine neurons encode a quantitative reward prediction error signal. *Neuron*, 47(1), pp.129–141.

Bevan, M.D. et al., 2002. Regulation of the timing and pattern of action potential generation in rat subthalamic neurons *in vitro* by GABA-A IPSPs. *Journal of Neurophysiology*, 87(3), pp.1348–1362.

Biolsi, B. et al., 2008. Long-term follow-up of Huntington disease treated by bilateral deep brain stimulation of the internal globus pallidus. *Journal of Neurosurgery*, 109(1), pp.130–132.

Bronstein, J.M. et al., 2011. Deep Brain Stimulation for Parkinson Disease. *Archives of Neurology*, 68(2).

Brown, P., 2007. Abnormal oscillatory synchronisation in the motor system leads to impaired movement. *Current opinion in neurobiology*, 17(6), pp.656–664.

Cazorla, M. et al., 2014. Dopamine D2 Receptors Regulate the Anatomical and Functional Balance of Basal Ganglia Circuitry. *Neuron*, 81(1), pp.153–164.

Chan, C.S., Surmeier, D.J. & Yung, W.-H., 2005. Striatal information signaling and integration in globus pallidus: timing matters. *Neuro-Signals*, 14(6), pp.281–289.

Chang, H.T., Penny, G.R. & Kitai, S.T., 1987. Enkephalinergic-cholinergic interaction in the rat globus pallidus: a pre-embedding double-labeling immunocytochemistry study. *Brain research*, 426(1), pp.197–203.

Chevalier, G. & Deniau, J.M., 1990. Disinhibition as a basic process in the expression of striatal functions. *Trends in Neurosciences*, 13(7), pp.277–280.

Constantinople, C.M. & Bruno, R.M., 2013. Deep Cortical Layers Are Activated Directly by Thalamus. *Science*, 340(6140), pp.1591–1594.

Cui, G. et al., 2014. Concurrent activation of striatal direct and indirect pathways during action initiation. *Nature*, 494(7436), pp.238–242.

DeLong, M.R., 1971. Activity of pallidal neurons during movement. *Journal of Neurophysiology*, 34(3), pp.414–427.

DeLong, M.R., 1990. Primate models of movement disorders of basal ganglia origin. *Trends in Neurosciences*, 13(7), pp.281–285.

Deniau, J.M. & Chevalier, G., 1985. Disinhibition as a basic process in the expression of striatal functions. II. The striato-nigral influence on thalamocortical cells of the ventromedial thalamic nucleus. *Brain research*, 334(2), pp.227–233.

Deniau, J.M., Lackner, D. & Féger, J., 1978. Effect of substantia nigra stimulation on identified neurons in the VL-VA thalamic complex: comparison between intact and chronically decorticated cats. *Brain research*, 145(1), pp.27–35.

Dongen, Y.C. et al., 2008. Three-dimensional organization of dendrites and local axon collaterals of shell and core medium-sized spiny projection neurons of the rat nucleus accumbens. *Brain Structure and Function*, 213(1-2), pp.129–147.

Ebrahimi, A., Pochet, R. & Roger, M., 1992. Topographical organization of the projections from physiologically identified areas of the motor cortex to the striatum in the rat. *Neuroscience Research*, 14(1), pp.39–60.

Freeze, B.S. et al., 2013. Control of Basal Ganglia Output by Direct and Indirect Pathway Projection Neurons. *Journal of Neuroscience*, 33(47), pp.18531–18539.

Gerfen, C.R., 1984. The neostriatal mosaic: compartmentalization of corticostriatal input and striatonigral output systems. *Nature*, 311(5985), pp.461–464.

Gerfen, C.R. et al., 1982. Crossed connections of the substantia nigra in the rat. *The Journal of comparative neurology*, 207(3), pp.283–303.

Gerfen, C.R. et al., 1990. D1 and D2 dopamine receptor-regulated gene expression of striatonigral and striatopallidal neurons. *Science*, 250(4986), pp.1429–1432.

Gildenberg, P.L., 2006. Evolution of Basal Ganglia Surgery for Movement Disorders. *Stereotactic and Functional Neurosurgery*, 84(4), pp.131–135.

Goldberg, J.H., Farries, M.A. & Fee, M.S., 2013. Basal ganglia output to the thalamus: still a paradox. *Trends in Neurosciences*, 36(12), pp.695–705.

Gradinaru, V. et al., 2009. Optical Deconstruction of Parkinsonian Neural Circuitry. *Science*, 324(5925), pp.354–359.

Graybiel, A.M., 1990. Neurotransmitters and neuromodulators in the basal ganglia. *Trends in Neurosciences*, 13(7), pp.244–254.

Graybiel, A.M., 1998. The basal ganglia and chunking of action repertoires. *Neurobiology of Learning and Memory*, 70(1-2), pp.119–136.

Graybiel, A.M. et al., 1994. The basal ganglia and adaptive motor control. *Science*, 265(5180), pp.1826–1831.

Grove, E.A., Domesick, V.B. & Nauta, W.J., 1986. Light microscopic evidence of striatal input to intrapallidal neurons of cholinergic cell group Ch4 in the rat: a study employing the anterograde tracer Phaseolus vulgaris leucoagglutinin (PHA-L). *Brain research*, 367(1-2), pp.379–384.

Haber, S.N., 2003. The primate basal ganglia: parallel and integrative networks. *Journal of Chemical Neuroanatomy*, 26(4), pp.317–330.

Haber, S.N. et al., 1985. Efferent connections of the ventral pallidum: evidence of a dual striato pallidofugal pathway. *The Journal of comparative neurology*, 235(3), pp.322–335.

Hawrylycz, M.J. et al., 2012. An anatomically comprehensive atlas of the adult human brain transcriptome. *Nature*, 489(7416), pp.391–399.

Heimer, L. et al., 2007. *Anatomy of Neuropsychiatry*, Academic Press.

Henny, P. & Jones, B.E., 2008. Projections from basal forebrain to prefrontal cortex comprise cholinergic, GABAergic and glutamatergic inputs to pyramidal cells or interneurons. *European Journal of Neuroscience*, 27(3), pp.654–670.

Higley, M.J. et al., 2011. Cholinergic Interneurons Mediate Fast VGluT3-Dependent Glutamatergic Transmission in the Striatum T. M. Dawson, ed. *PloS one*, 6(4), p.e19155.

Hikosaka, O., Sakamoto, M. & Usui, S., 1989. Functional properties of monkey caudate neurons. I. Activities related to saccadic eye movements. *Journal of Neurophysiology*, 61(4), pp.780–798.

Histed, M.H., Carvalho, L.A. & Maunsell, J.H.R., 2012. Psychophysical measurement of contrast sensitivity in the behaving mouse. *Journal of Neurophysiology*, 107(3), pp.758–765.

Isomura, Y. et al., 2013. Reward-Modulated Motor Information in Identified Striatum Neurons. *Journal of Neuroscience*, 33(25), pp.10209–10220.

Jin, X., Tecuapetla, F. & Costa, R.M., 2014. Basal ganglia subcircuits distinctively encode the parsing and concatenation of action sequences. *Nature neuroscience*.

Kawaguchi, Y., Wilson, C.J. & Emson, P.C., 1990. Projection subtypes of rat neostriatal matrix cells revealed by intracellular injection of biocytin. *The Journal of Neuroscience*, 10(10), pp.3421–3438.

Kelly, R.M. & Strick, P.L., 2004. Macro-architecture of basal ganglia loops with the cerebral cortex: use of rabies virus to reveal multisynaptic circuits. *Progress in brain research*, 143, pp.449–459.

Kimura, M., Rajkowski, J. & Evarts, E., 1984. Tonically discharging putamen neurons exhibit set-dependent responses. *Proceedings of the National Academy of Sciences of the United States of America*, 81(15), pp.4998–5001.

Kita, H., 2007. Globus pallidus external segment. *Progress in brain research*, 160, pp.111–133.

Kita, H. & Kitai, S.T., 1994. The morphology of globus pallidus projection neurons in the rat: an intracellular staining study. *Brain research*, 636(2), pp.308–319.

Koralek, A.C., Costa, R.M. & Carmena, J.M., 2013. Temporally Precise Cell-Specific Coherence Develops in Corticostriatal Networksduring Learning. *Neuron*, 79(5), pp.865–872.

Kozorovitskiy, Y. et al., 2012. Recurrent network activity drives striatal synaptogenesis. *Nature*, pp.1–8.

Kravitz, A.V. et al., 2010. Regulation of parkinsonian motor behaviours by optogenetic control of basal ganglia circuitry. *Nature*, 466(7306), pp.622–626.

Kravitz, A.V., Tye, L.D. & Kreitzer, A.C., 2012. Distinct roles for direct and indirect pathway striatal neurons in reinforcement. *Nature neuroscience*, 15(6), pp.816–818.

Kreitzer, A.C. & Berke, J.D., 2011. Investigating striatal function through cell-type-specific manipulations. *Neuroscience*, 198, pp.19–26.

Kuramoto, E. et al., 2009. Two Types of Thalamocortical Projections from the Motor Thalamic Nuclei of the Rat: A Single Neuron-Tracing Study Using Viral Vectors. *Cerebral Cortex*, 19(9), pp.2065–2077.

Laplane, D. et al., 1989. Obsessive-compulsive and other behavioural changes with bilateral basal ganglia lesions. A neuropsychological, magnetic resonance imaging and positron tomography study. *Brain : a journal of neurology*, 112 (Pt 3), pp.699–725.

Lee, G. & Shaw, C.A., 2012. The History of the Basal Ganglia: The Contribution of Karl Friedrich Burdach. *Neuroscience and Medicine*, 03(04), pp.374–379.

Lefort, S. et al., 2009. The Excitatory Neuronal Network of the C2 Barrel Column in Mouse Primary Somatosensory Cortex. *Neuron*, 61(2), pp.301–316.

Mahon, S. et al., 2006. Distinct Patterns of Striatal Medium Spiny Neuron Activity during the Natural Sleep-Wake Cycle. *Journal of Neuroscience*, 26(48), pp.12587–12595.

Mallet, N. et al., 2012. Dichotomous organization of the external globus pallidus. *Neuron*, 74(6), pp.1075–1086.

Markram, H. et al., 2004. Interneurons of the neocortical inhibitory system. *Nature Reviews Neuroscience*, 5(10), pp.793–807. Available at: http://www.nature.com/nrn/journal/v5/n10/abs/nrn1519.html.

Marsden, C.D., 1982. Basal ganglia disease. *Lancet*, 2(8308), pp.1141–1147.

Marsden, C.D. & Obeso, J.A., 1994. The functions of the basal ganglia and the paradox of stereotaxic surgery in Parkinson's disease. *Brain : a journal of neurology*, 117 (Pt 4), pp.877–897.

Mastro, K.J. et al., 2014. Transgenic Mouse Lines Subdivide External Segment of the Globus Pallidus (GPe) Neurons and Reveal Distinct GPe Output Pathways. *Journal of Neuroscience*, 34(6), pp.2087–2099.

Matsumoto, N. et al., 2001. Neurons in the thalamic CM-Pf complex supply striatal neurons with information about behaviorally significant sensory events. *Journal of Neurophysiology*, 85(2), pp.960–976.

McFarland, N.R. & Haber, S.N., 2002. Thalamic relay nuclei of the basal ganglia form both reciprocal and nonreciprocal cortical connections, linking multiple frontal cortical areas. *Journal of Neuroscience*, 22(18), pp.8117–8132.

McKinney, M., Coyle, J.T. & Hedreen, J.C., 1983. Topographic analysis of the innervation of the rat neocortex and hippocampus by the basal forebrain cholinergic system. *The Journal of comparative neurology*, 217(1), pp.103–121.

Mesulam, M.M. et al., 1984. Atlas of cholinergic neurons in the forebrain and upper brainstem of the macaque based on monoclonal choline acetyltransferase immunohistochemistry and acetylcholinesterase histochemistry. *Neuroscience*, 12(3), pp.669–686.

Meyer, A. & Hierons, R., 1964. A NOTE ON THOMAS WILLIS' VIEWS ON THE CORPUS STRIATUM AND THE INTERNAL CAPSULE. *Journal of the neurological sciences*, 1(6), pp.547–554.

Mink, J.W. & Thach, W.T., 1991. Basal ganglia motor control. II. Late pallidal timing relative to movement onset and inconsistent pallidal coding of movement parameters. *Journal of Neurophysiology*, 65(2), pp.301–329.

Montgomery, E.B., 2004. Deep brain stimulation for hyperkinetic disorders. *Neurosurgical focus*, 17(1), p.E1.

Munz, P. et al., 2009. When zombies attack!: mathematical modelling of an outbreak of zombie infection. *Infectious Disease Modelling Research Progress*, 4, pp.133–150.

Nambu, A., 2011. Somatotopic organization of the primate Basal Ganglia. *Frontiers in neuroanatomy*, 5, p.26.

Nambu, A., Tokuno, H. & Takada, M., 2002. Functional significance of the cortico-subthalamo-pallidal “hyperdirect” pathway. *Neuroscience Research*, 43(2), pp.111–117.

Oh, S.W. et al., 2014. A mesoscale connectome of the mouse brain. *Nature*, 508(7495), pp.207–214.

Oldenburg, I.A. & Ding, J.B., 2011. Cholinergic modulation of synaptic integration and dendritic excitability in the striatum. *Current opinion in neurobiology*, 21(3), pp.425–432.

Parent, A., 1990. Extrinsic connections of the basal ganglia. *Trends in Neurosciences*, 13(7), pp.254–258.

Parent, A. & Hazrati, L.N., 1995. Functional anatomy of the basal ganglia. I. The cortico-basal ganglia-thalamo-cortical loop. *Brain research. Brain research reviews*, 20(1), pp.91–127.

Rye, D.B. et al., 1984. Cortical projections arising from the basal forebrain: a study of cholinergic and noncholinergic components employing combined retrograde tracing and immunohistochemical localization of choline acetyltransferase. *Neuroscience*, 13(3), pp.627–643.

Saper, C.B. & Chelimsky, T.C., 1984. A cytoarchitectonic and histochemical study of nucleus basalis and associated cell groups in the normal human brain. *Neuroscience*, 13(4), pp.1023–1037.

Sarter, M. & Bruno, J.P., 2002. The neglected constituent of the basal forebrain corticopetal projection system: GABAergic projections. *European Journal of Neuroscience*, 15(12), pp.1867–1873.

Saunders, A., Johnson, C.A. & Sabatini, B.L., 2012. Novel recombinant adeno-associated viruses for Cre activated and inactivated transgene expression in neurons. *Frontiers in neural circuits*, 6, p.47.

Sawamoto, N. et al., 2002. Cognitive slowing in Parkinson's disease: a behavioral evaluation independent of motor slowing. *Journal of Neuroscience*, 22(12), pp.5198–5203.

Schmidt, R. et al., 2013. Canceling actions involves a race between basal ganglia pathways. *Nature neuroscience*, 16(8), pp.1118–1124.

Schultz, W., Tremblay, L. & Hollerman, J.R., 2003. Changes in behavior-related neuronal activity in the striatum during learning. *Trends in Neurosciences*, 26(6), pp.321–328.

Smith, Y. & Bolam, J.P., 1991. Convergence of synaptic inputs from the striatum and the globus pallidus onto identified nigrocollicular cells in the rat: a double anterograde labelling study. *Neuroscience*, 44(1), pp.45–73.

Smith, Y. & Bolam, J.P., 1989. Neurons of the substantia nigra reticulata receive a dense GABA-containing input from the globus pallidus in the rat. *Brain research*, 493(1), pp.160–167.

Smith, Y. et al., 1998. Microcircuitry of the direct and indirect pathways of the basal ganglia. *Neuroscience*, 86(2), pp.353–387.

Spampinato, U. et al., 1986. Apomorphine and haloperidol effects on striatal 3H-dopamine release in anesthetized, awake restrained and freely moving rats. *Brain Research Bulletin*, 16(2), pp.161–166.

Stern, E.A., Jaeger, D. & Wilson, C.J., 1998. Membrane potential synchrony of simultaneously recorded striatal spiny neurons *in vivo*. *Nature*, 394(6692), pp.475–478.

Takada, M. et al., 1998. Corticostriatal projections from the somatic motor areas of the frontal cortex in the macaque monkey: segregation versus overlap of input zones from the primary motor cortex, the supplementary motor area, and the premotor cortex. *Experimental brain research Experimentelle Hirnforschung Expérimentation cérébrale*, 120(1), pp.114–128.

Takada, M., Ng, G. & Hattori, T., 1986. Single pallidal neurons project both to the striatum and thalamus in the rat. *Neuroscience letters*, 69(3), pp.217–220.

Taverna, S., Ilijic, E. & Surmeier, D.J., 2008. Recurrent Collateral Connections of Striatal Medium Spiny Neurons Are Disrupted in Models of Parkinson's Disease. *Journal of Neuroscience*, 28(21), pp.5504–5512.

Tennant, K.A. et al., 2011. The Organization of the Forelimb Representation of the C57BL/6 Mouse Motor Cortex as Defined by Intracortical Microstimulation and Cytoarchitecture. *Cerebral Cortex*, 21(4), pp.865–876.

Tepper, J.M. & Bolam, J.P., 2004. Functional diversity and specificity of neostriatal interneurons. *Current opinion in neurobiology*, 14(6), pp.685–692.

Tepper, J.M., Koós, T. & Wilson, C.J., 2004. GABAergic microcircuits in the neostriatum. *Trends in Neurosciences*, 27(11), pp.662–669.

Thorn, C.A. et al., 2010. Differential Dynamics of Activity Changes in Dorsolateral and Dorsomedial Striatal Loops during Learning. *Neuron*, 66(5), pp.781–795.

Tkatch, T., Baranauskas, G. & Surmeier, D.J., 1998. Basal forebrain neurons adjacent to the globus pallidus co-express GABAergic and cholinergic marker mRNAs. *NeuroReport*, 9(9), pp.1935–1939.

Weiner, D.M., Levey, A.I. & Brann, M.R., 1990. Expression of muscarinic acetylcholine and dopamine receptor mRNAs in rat basal ganglia. *Proceedings of the National Academy of Sciences of the United States of America*, 87(18), pp.7050–7054.

Willis, T., 1664. *Cerebri anatome*,

Wilson, C.J. & Groves, P.M., 1980. Fine structure and synaptic connections of the common spiny neuron of the rat neostriatum: a study employing intracellular injection of horseradish peroxidase. *Journal of Comparative Neurology*, 194(3), pp.599–615.

Yin, H.H. & Knowlton, B.J., 2006. The role of the basal ganglia in habit formation. *Nature Reviews Neuroscience*, 7(6), pp.464–476.

Appendix A

Tool Development:

Multipoint-Emitting Optical Fibers for Spatially Addressable *In vivo* Optogenetics

Ferruccio Pisanello, Leonardo Sileo, Ian Antón Oldenburg, Marco Pisanello, Luigi Martiradonna, John A. Assad, Bernardo L. Sabatini, Massimo De Vittorio.

This chapter is based on a based on published work:

Pisanello F, Sileo L, Oldenburg IA, Pisanello M, Martiradonna L, Assad JA, Sabatini BL, De Vittorio M, Multipoint-Emitting Optical Fibers for Spatially Addressable *In vivo* Optogenetics. Neuron. 2014 May 28. pii: S0896-6273(14)00356-0. doi: 10.1016/j.neuron.2014.04.041.

Acknowledgement of the work of others:

The following section was created in collaboration with the group lead by Massimo De Vittorio at the Instituto Italiano Di Tecnologia in Lecce Italy. Ferruccio Pisanello, Leonardo Sileo, Marco Pisanello, Luigi Martiradonna, and Massimo De Vittorio fabricated and tested the probes. While Ian Antón Oldenburg and Bernardo Sabatini, validated and tested the probes in tissue *in vivo.* Both groups contributed to the design of the probes. The entire publication, including details of the fabrication of these probes, is included for clarity. The manuscript was written by Ferruccio Pisanello with contributions from all other authors. Ian Oldenburg wrote the sections regarding extracellular recordings.

A1.1: ABSTRACT

Optical stimulation and silencing of neural activity is a powerful technique for elucidating the structure and function of neural circuitry. In most *in vivo* optogenetic experiments, light is delivered into the brain through a single optical fiber. However, this approach limits illumination to a fixed volume of the brain. Here a focused ion beam is used to pattern multiple light windows on a tapered optical fiber. We show that such fibers allow selective and dynamical illumination of different brain regions along the taper. Site selection is achieved by a simple coupling strategy at the fiber input, and the use of a single tapered waveguide minimizes the implant invasiveness. We demonstrate the effectiveness of this approach for multipoint optical stimulation in the mammalian brain *in vivo* by coupling the fiber to a microelectrode array and performing simultaneous extracellular recording and stimulation at multiple sites in the mouse striatum and cerebral cortex.

A1.2: INTRODUCTION

The use of microbial opsins for optical stimulation and silencing of neuronal activity (optogenetics) facilitates understanding neural circuits and linking the activity of circuit elements to behavior (Alivisatos et al., 2013; Andrasfalvy et al., 2010; Boyden et al., 2005; Han and Boyden, 2007; Liu et al., 2012; Papagiakoumou et al., 2010; Prakash et al., 2012; Rickgauer and Tank, 2009; Zhang et al., 2007). Optogenetics has in turn created a demand for optical devices that target delivery of light to sub-regions of the living brain. Current spatially selective light-delivery devices for optogenetics are based on solid-state photonic waveguide array or integrated semiconductor light-emitting diodes (LEDs), each exciting a specific spot in the brain by exploiting the spatial distribution of multiple light emitters. This control has been achieved by means of several technological approaches, including amplitude or phase modulation (Anselmi et al., 2011; Grossman et al., 2010), glass-sharpened optrodes (Abaya et al., 2012a; Abaya et al., 2012b), arrayed optical fibers (Royer et al., 2010; Stark et al., 2012), multi-waveguide fabrication on a single substrate (Zorzos et al., 2010), endoscopic fiber bundles (Hayashi et al., 2012), LED-coupled tapered fiber arrays (Stark et al., 2012), and wireless micrometer-sized LEDs on flexible shafts (Kim et al., 2013). Recently, implantable three-dimensional sets of silicon oxynitride waveguides have been developed, raising the possibility of generating 3D distributed light patterns in the brain (Zorzos et al., 2012). Individual waveguides can be addressed by a matrix of micromirrors (Zorzos et al., 2012) or separately coupled to different light sources (Stark et al., 2012), allowing optical stimulation at each point with tunable wavelength and intensity.

While these methods allow spatially selective illumination, they require a complex fabrication process and/or coupling strategy at the distal end of the waveguides. Moreover, despite the wide range of proposed devices, only a few have been tested *in vivo* (Hayashi et al., 2012; Kim et al., 2013; Royer et al., 2010; Stark et al., 2012; Tamura et al., 2012). These devices are also quite invasive due to the large number of implanted waveguides, oversized optical components, blunt inserting edges and potentially high temperatures generated by implanted electronics.

Here we describe the implementation of a novel optogenetic tool based on a *single* waveguide that, by a simple optical strategy, can selectively and dynamically illuminate multiple brain regions. The device is minimally invasive because it comprises only one thin fiber with a sharp, tapered tip. To demonstrate the effectiveness of this device *in vivo*, we coupled it to a linear array of microelectrodes for simultaneous multi-site extracellular recording and optical stimulation in the brain of awake mice. In a proof-of-principle experiment to validate the methodology, we find that activation of GABAergic interneurons at different depths in primary motor cortex differentially modulate subsets of cortical neurons, suggesting cell-to-cell specificity of GABAergic inhibition in the living mammalian brain.

A1.3: Results

A single core optical fiber with cladding (total diameter d_0=125mm; see Experimental Procedures for further details) was tapered and, with exception of a 200 nm diameter circular area at the tip, was coated with gold as a reflective material (**Figure A.1A & B**). The tapered shape allows selection and manipulation of propagating and evanescent modes, whereas the coating prevents leakage of light (Novotny and Hecht, 2006). Light emission is permitted at selected sites along the taper by locally removing the coating to create “windows”. Illumination with a well-defined modal set at the fiber input addresses emission to specific windows along the fiber.

The gradual taper angle (~3°-6°) and the small external diameter of the tip (~600nm) allow smooth insertion into the brain, thereby reducing tissue damage. To obtain multiple optical windows, the reflective coating along the taper and part of the underlying material are pierced at selected points, allowing light of specific modes to escape into the surrounding environment. In the following we discuss three different devices, displayed in **Figures A.1B-1D**, in which two, three or seven optical windows were created by focused ion beam (FIB) milling (detailed geometrical parameters of each optical aperture are given in Experimental Procedures section). FIB is a particularly versatile technology for this purpose because it allows localized micromachining all along the fiber taper with a resolution better than 50nm. Thus optical apertures can be milled with different sizes and shapes (**Figures A.1E-1F**) and relatively simple optical elements, such as diffraction gratings or metallic mirrors, can be fabricated using ion- or electron-beam induced deposition within the same system (Cheng and Steckl, 2002). We used square patterned windows for this study, but the approach can be easily extended to other types of optical elements along the taper.

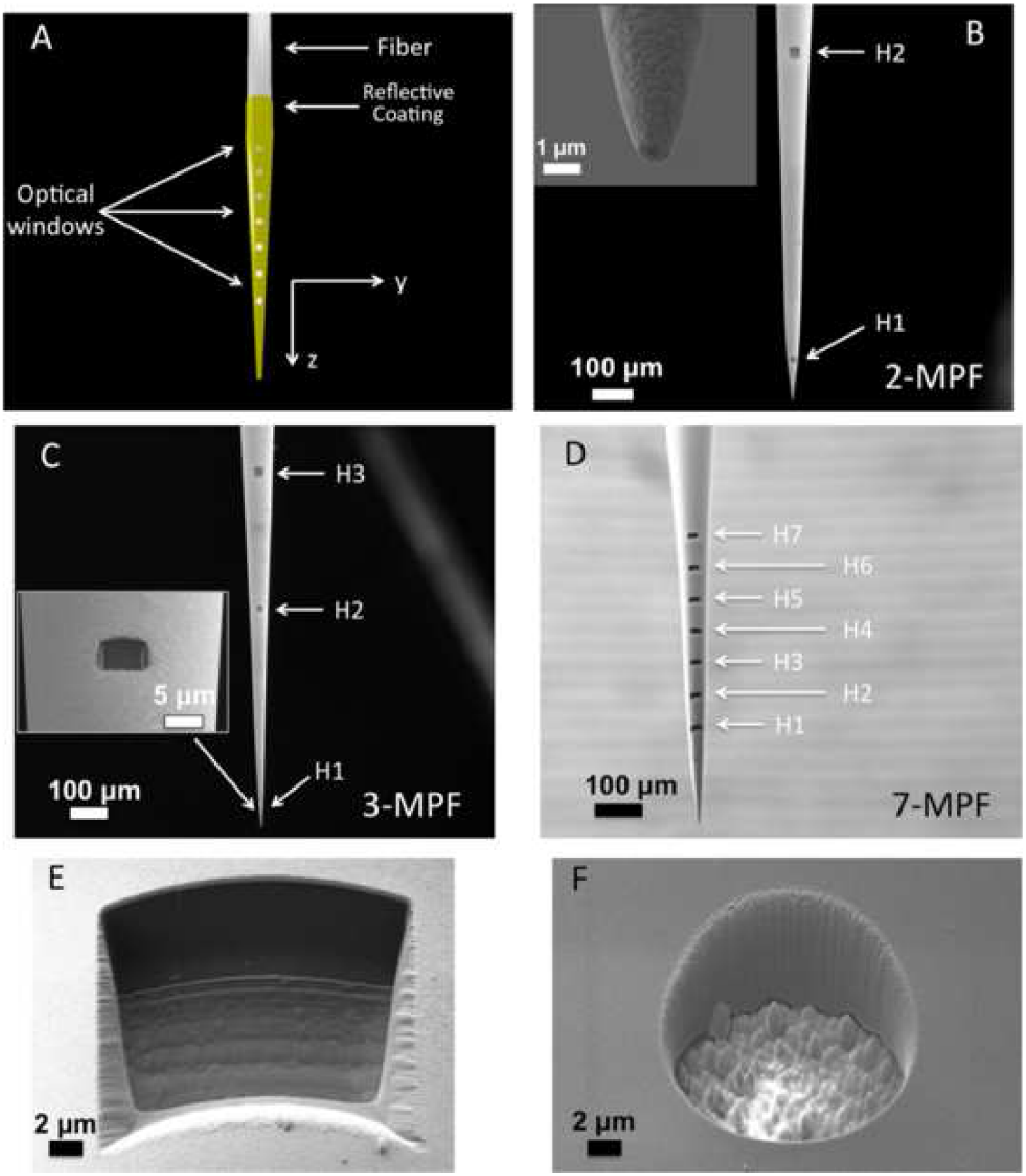

Figure A.1. Multi-point emitting optical fibers.

(A) Schematic representation of a seven-window multi-point emitting optical fiber device. **(B- D)** SEM micrograph of the realized devices. The inset in panel B shows the circular aperture at the taper tip. The inset in panel C shows the smallest optical window realized in the case of a three-window multi-point emitting optical fiber. **(E-F)** A square (panel E) and circular (panel F) optical window realized on the taper edge.

A1.3.1: Optical properties of multi-point emitting optical fibers in non-scattering medium

Each micro-machined window out-couples only a fraction of the light that is guided into the fiber. The remaining radiation propagates further into the taper and undergoes a modal manipulation and selection: the transversal component of the wave vector associated to the *j*- th mode (*kjT*) increases as the taper narrows (**Figure A.2A**). As detailed in Experimental Procedures, this implies that the higher the *kjT* value of modes at the taper entrance, the shorter the propagation length of the *j*-th mode into the taper. Because the lower order modes propagate further down the taper than the higher order modes, this allows a strategy to out- couple light from specific optical windows along the taper. The simplest way to control *kjT* values at the taper input is to modify the input-coupling angle θ at the distal end of the fiber. The higher the input coupling angle θ, the higher the *kT* of the light guided into the fiber (**Figure A. 2B**; see Supplemental Information for theory related to these phenomena).

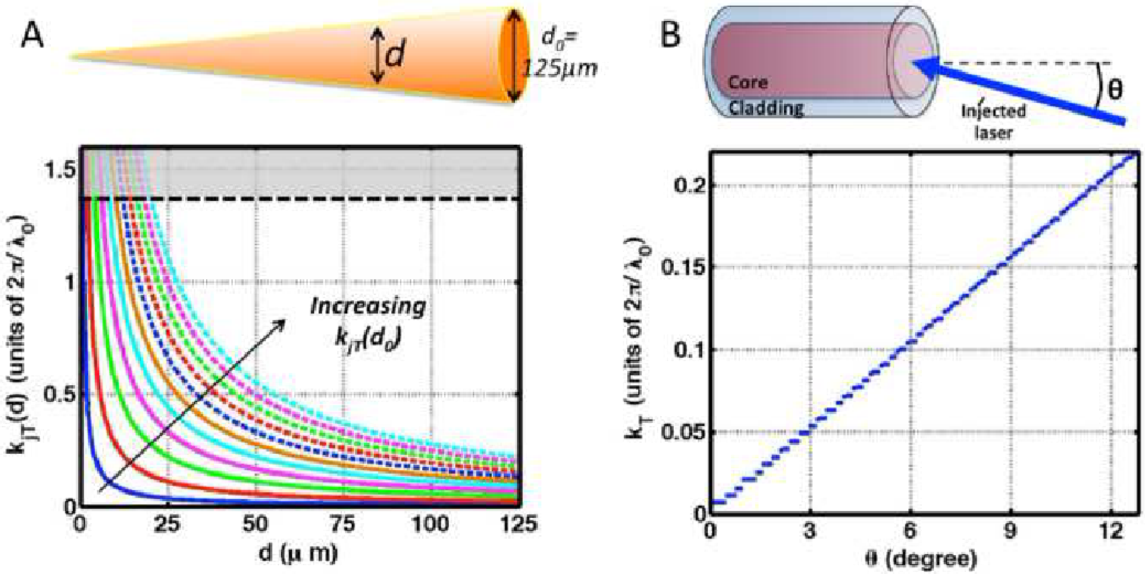

Figure A.2. Modal evolution in multi-point emitting optical fibers.

(A) *kjT(d)* evolution as a function of the taper diameter *d*. Each color represents a different value of *kjT(d0)* at the taper entrance. The dashed black line represents the *kj* value into the taper. For kjT>kj, the *j*-th mode becomes evanescent and lies within the grey area. **(B)** *kT* of the most powerful injected in the core/cladding section of the optical fiber, as a function of the input coupling angle θ. Details on the calculations reported in are given in Supplemental Information.

In order to control the input light angle to the fiber, a λ_0=473nm laser is reflected by a fixed mirror (M1) and a sliding mirror (M2), whose position defines the input coupling angle θ (**Figure A.3A**). When the mirror M2 is in the *Home* position, the laser beam travels perpendicularly through the center of the lens L1, which focuses the optical radiation coaxially to the optical fiber axis (θ=0°). If the mirror is moved along the optical axis, the light is focused into the fiber coupler with a different θ.

When θ is changed, the out-coupled light intensity redistributes among the optical windows. At θ~0°, most of the light is emitted from the fiber tip (**Sup Figure A.S4**). However, as θ is increased above ~2°, tip emission becomes negligible and most of the light is emitted by the side apertures. Emission evolves as a function of θ, demonstrated in **Figure A.3** for a 2-, 3- and 7- window multi-point emitting fibers (hereafter referred to as 2-, 3- and 7-MPF) immersed in a Fluorescein:water solution. At low θ, light is predominantly emitted by the holes closest to the tip, and in both 2- and 3-MPF non-negligible emission takes place only at window H1 (**Figures A.3 B1 & C1**). Progressively increasing θ directs light emission to window H2 for the 2-MPF (**Figure A.3 B2 & B3**) and to H2 and then H3 for the 3-MPF (**Figure A.3 C2 & C3**). This allows the independent control of two or three emitting points along 700µm, with spatially sharp emission profiles (**Figures A.3 B4 & C4**). In the case of the 7-MPF, the light emission is less selective among the closely-spaced windows, but increasing θ still shifts the maximum of the emitted light towards the windows further from the tip, and emission from all windows defines the point of maximum intensity (**Figure A.3 D4**).

These behaviors can be explained by the modal manipulation performed by the taper on *kjT*, whose values strongly influence the radiation efficiency of each side window (**Sup Figure A.S2**). This is confirmed by the directionality of out-coupled light: increasing θ is accompanied by a moderate tilting of the output angle of the light beams (**Figures A.3 B5, 3C5 and 3D5**). The closer

Figure A.3. Optical properties of the multi-point emitting optical fiber in fluorescein solution

(A) Optical setup used to modify the input-coupling angle θ. A CW λ_0=473nm laser beam is reflected by a fixed mirror (M1) and a sliding mirror (M2) redirects it toward lens L1. When M2 is in the *Home* position, the laser beam travels perpendicularly to L1 and through its center, and is then focused onto the optical fiber. When M2 is moved by P_{M2} along the optical axis of the setup, the laser beam is still perpendicular to L1 but it is focused into the optical fiber with an angle θ. To perform optical characterization of the device, the fiber taper was immersed in a fluorescein bath and the fluorescein emission collected by an optical microscope equipped by a FITC filter and a color CCD camera. **(B-D)** Light-microscope images of the 2-, 3- and 7- window devices immersed in a drop of Fluorescein:water solution with no laser coupled at its entrance, respectively. **(B1-B3,C1-C3,D1-D3):** Fluorescence images showing the taper emission for three different input-coupling angles. Scale bars are 100µm. Continuous white lines were added to highlight the taper profile. Dashed lines identify where the intensity profiles in panels B4, C4 and D4 were measured. **(B4,C4,D4)** Intensity profiles collected 100µm from the fiber taper, along the white dashed lines displayed in panels B1, C1 and D1. **(B5,C5,D5)** Output angle as a function of the input coupling angle θ for 2-, 3- and 7- window MPF, respectively. Output angle is defined in panel B2.

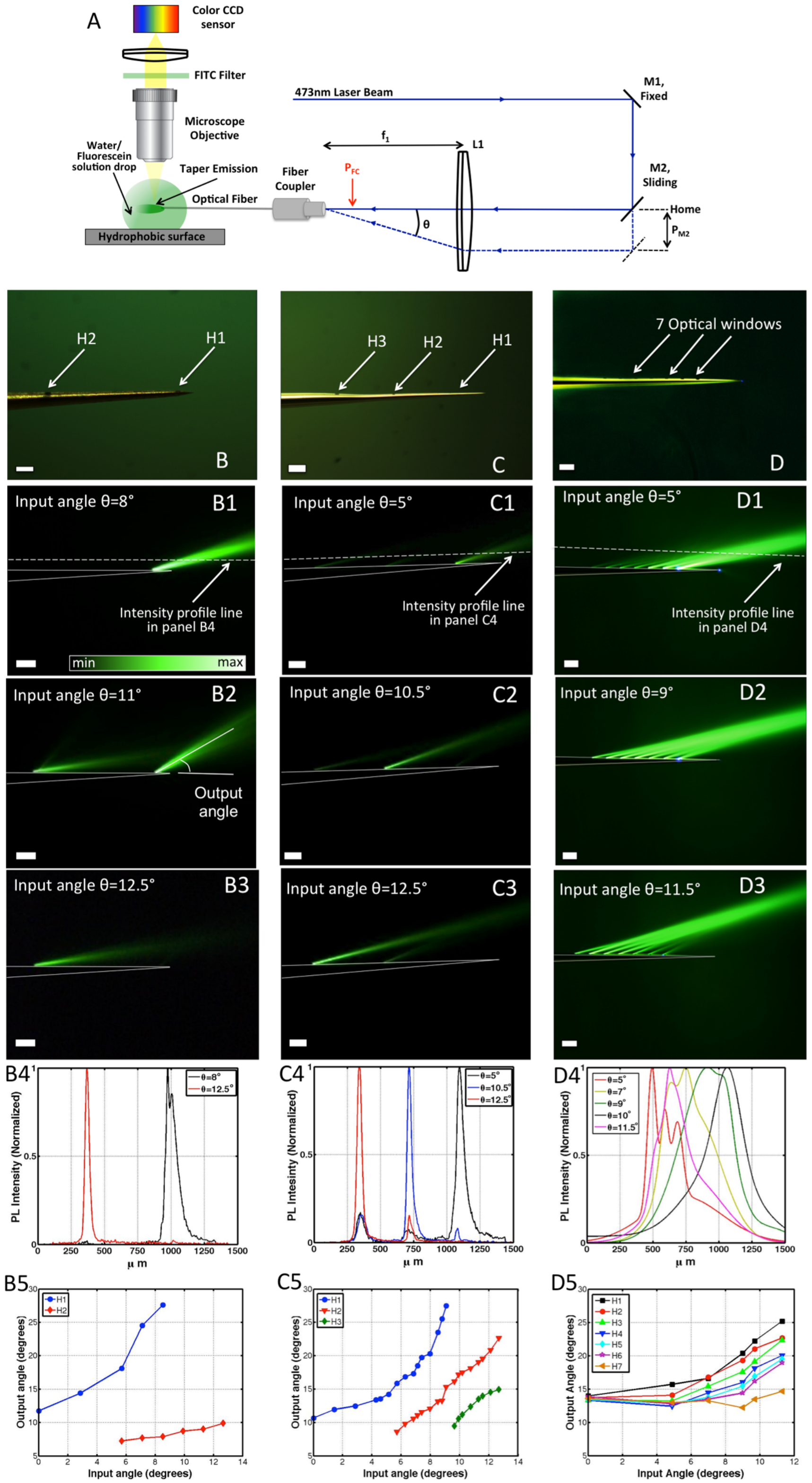

Figure A.3. (Continued): Optical properties of the multi-point emitting optical fiber in fluorescein solution

the window to the taper tip, the wider the tilting of the out-coupled beam, by virtue of the wider range of kjT values between θ~0° and θ~12.5°.

Due to modes evanescence, the maximum out-coupling efficiency is not the same for all the side windows. Thus, the input power needed in order to emit a constant power (P_{out}) at each window varies. We determined the input power (P_{FC}) and angle (θ) required at the fiber connector to output ~0.1 mW at the selected window while maintaining extinction ratios (the ratios of powers emitted by non-selected and selected windows) below 1:10 for 2-MPF and 1:4 for 3-MPF. In the case of a 2-MPF, this occurred for H1 with θ=8° and P_{FC}~2.3mW and for H2 with θ=12.5° and P_{FC}~15mW. For the 3-MPF, this required P_{FC}~25mW at θ=5° (H1), P P_{FC}~22mW at θ=10.5° (H2) and P_{FC}~15mW at θ=12.5° (H3). In contrast, in the 7-MPF the emission of all apertures contributes to the total emitting power: the input power to obtain P_{out}~0.1mW at 100µm from the taper was estimated to be P_{FC}~1.5mW at θ=5°, P_{FC}~1mW at θ=9° and P_{FC}~7mW at θ=11.5°.

A1.3.2: Optical properties of multi-point emitting optical fibers in brain tissue

In the brain, scattering and absorption of light by tissue determine the distribution of photons emitted by an optical fiber (Yizhar et al., 2011). To test how light emitted from the small windows on the tapered fibers behaves in scattering medium, we measured the fluorescent profiles generated by 2-, 3- and 7-MPFs inserted into fluorescein-stained coronal mouse brain- slices (**Figures A.4 A-C)**. For the 2- and 3-MPFs two main differences were observed compared to fluorescein in solution: (i) spreading of the emitted beam, as shown by the iso-intensity curves in **Figures A.4D-E**, and (ii) faster decay of light intensity due to tissue absorption (**Figure A.4 F**). Nevertheless, the active window can still be selected by changing the input-coupling angle θ for both 2- and 3-MPF (**Figures A.4 A4 & 4B4**) with only slight variations in the angle dependence compared to fluorescein in solution (**Sup Figure A.S8**). For 7-MPF, the spread of the beam emitted by a single window results in a strongly reduced influence of θ on the selection of the illuminated brain region (**Figure A.4 C4**) with respect to fluorescein in solution.

While all *in vivo* experiments reported below were carried out on head-restrained mice, the device can be easily adapted to freely behaving animals, where a short fiber stub is implanted into the moving mouse and an extension fiber is used to bring light to the stub. In order to demonstrate that the coupling at the fiber junction as well as fiber bending induced by mouse movement would not lead to significant modifications of MPFs light emission, we tested a warped 2-MPF using an extension fiber (**Figure A.5 D**). Emission properties were characterized before and after warping the fiber, to simulate animal movement. As shown in **Figures A.5E-H**, windows H1 and H2 could still be independently addressed by changing θ, with only slight variations of emission profiles (**Figure A.5 I**). To assess warping effects on outcoupled power (Pout), Pout was set at 0.1mW before warping the fiber, and output power was then evaluated after warping. The rolling-unrolling experiment was performed six times. During fiber warping, at H1 we measured an average power output of 0.113mW (SD: 0.008mW), while at H2 we obtained 0.097mW (SD: 0.008mW). For comparison, the same evaluation on a standard core-cladding fiber without tapered region yielded Pout=0.100±0.002mW. Warping also had very little effect on out coupling angles: in the same experiment we found that the output angles were 18.70°±0.21° for H1 and 14.61°±0.04° for H2 for the warped fiber, compared to 18.53° for H1 and 14.62° for H2 for the non-warped fiber. The minor effects of fiber warping on the outcoupling of light pave the way for application of MPFs to free-moving animals.

Figure A.4. Optical properties of the multi-point emitting optical fiber in fluorescein- stained coronal brain slices.

(A-C) Light-microscope images of the 2-, 3- and 7- window devices inserted in fluorescein- stained mouse brain slices. **(A1-A3,B1-B3,C1-C3)** Fluorescence images showing the taper emission in fluorescein-stained mouse brain slices for three different input-coupling angles. Scale bars are 100µm. Continuous white lines were added to highlight the taper profile. Dashed lines identify where the intensity profiles in panels A4, B4 and C4 were measured. **(A4,B4,C4)** Intensity profiles collected 100µm from the fiber taper; black dashed line identify the position of taper tip. **(D,E)** Iso-intensity photoluminescence curves for a single optical window emitting in Fluorescein:water solution (panel D) and in fluorescein-stained brain slices (panel E). Scale bars are 100µm. Dashed lines identify where the intensity profiles in panel F were measured. **(F)** Photoluminescence intensity decay comparison in Fluorescein:water solution and brain tissue for windows H1 measured along the white dashed lines in panels D and E, respectively.

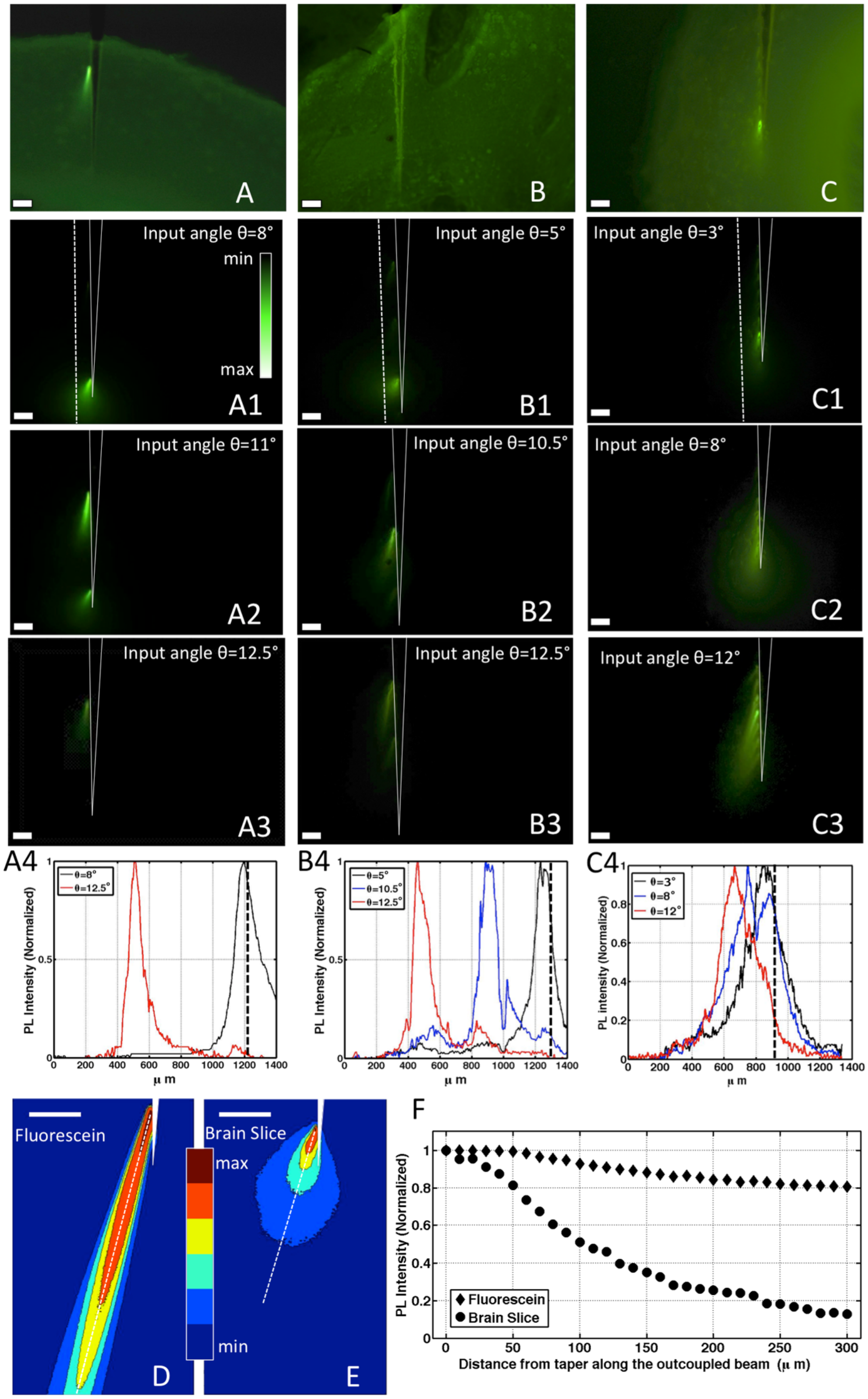

Figure A.4. (Continued): Optical properties of the multi-point emitting optical fiber in fluorescein-stained coronal brain slices.

A1.3.4: *In vivo* use of multi-point emitting optical fibers

To test the ability to address optical excitation to different parts of the brain along the length of the fiber, we coupled 2- and 7-MPFs to a linear array of microelectrodes on a silicon shank (Neuronexus Technologies, Inc.). The microstructured optical fiber was fixed in parallel to the shank of the multi-electrode (**Figure A.6 A and Sup Figure A.S9**). To minimize light-induced artifacts in the recorded electrical signal (due to the Becquerel photoelectric effect) (Cardin et al., 2010; Han et al., 2009), the optical windows were oriented to illuminate the region immediately above the recording pads. To ensure that apertures were properly angled, the optrode was first tested in a phosphate buffered saline (PBS) solution. Photoelectrical artifacts were not detectable at any laser power tested or any input coupling angle, confirming that the fiber apertures did not directly illuminate the recording pads (**Sup Figure A.S10**). For comparison, we used the same PBS bath to test a commercial optrode, with light delivery based on a single step - index optical fiber placed just above the last recording site (model A1x16-3mm-50-413-OA16-50 from Neuronexus Technologies, Inc.). Light-induced artifacts were observed during both *OFF-ON* and *ON-OFF* light transitions at laser powers $P_{FC} \geq 33.9$mW at the optical fiber input (**Sup Figure A.S10**).

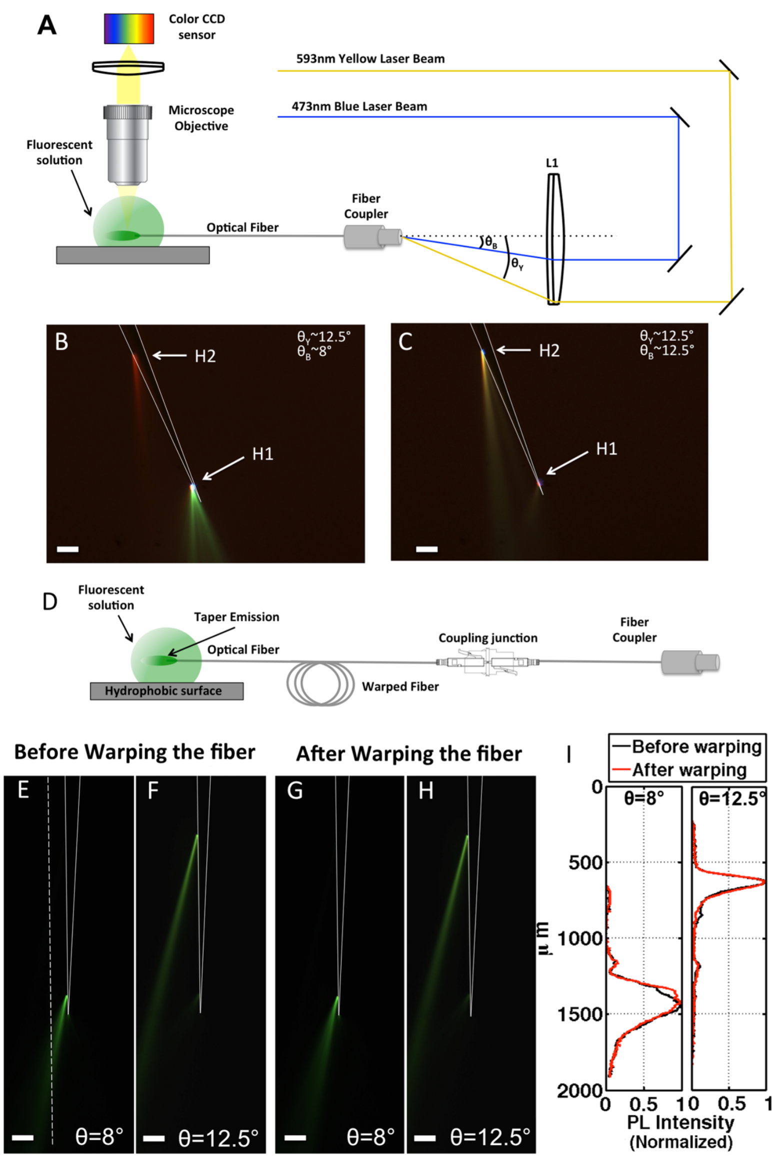

Figure A.5. Two-color emission and proof-of-principle for use of device with freely behaving animals.

(A) Optical setup used to couple two different light beams into the optical fiber, with input coupling angles θ_B and θ_Y for blue and yellow lasers, respectively. **(B)** Fluorescence image of a 2-MPF immersed in a Fluorescein:TexasRed:water solution for θ_B~8° and θ_Y~12.5°. The blue light excites only fluorescein, which emits at green wavelengths. The yellow light excites only TexasRed, emitting in the red. **(C)** Fluorescence image of a 2-MPF immersed in a Fluorescein:TexasRed:water solution for θ_B~12.5° and θ_Y~12.5°. The superposition between green fluorescein luminescence and red TexasRed luminescence resulted in brown color at the CCD camera. **(D)** Schematic representation of the setup used to test MPF with warped fiber and extension cords. **(E-H)** Fluorescence images showing the taper emission for the configuration represented in panel D before (panels E and F) and after (panels G and H) warping the fiber, at two different θ. The fiber was rolled twice with a curvature radius of 4.5cm. Scale bars are 100μm. Continuous white lines were added to highlight the taper profile. Dashed line in panel E identify where the intensity profiles in panel I were measured. **(I)** Intensity profiles before (black) and after (red) warping the fiber measured along the white dashed line in panel E.

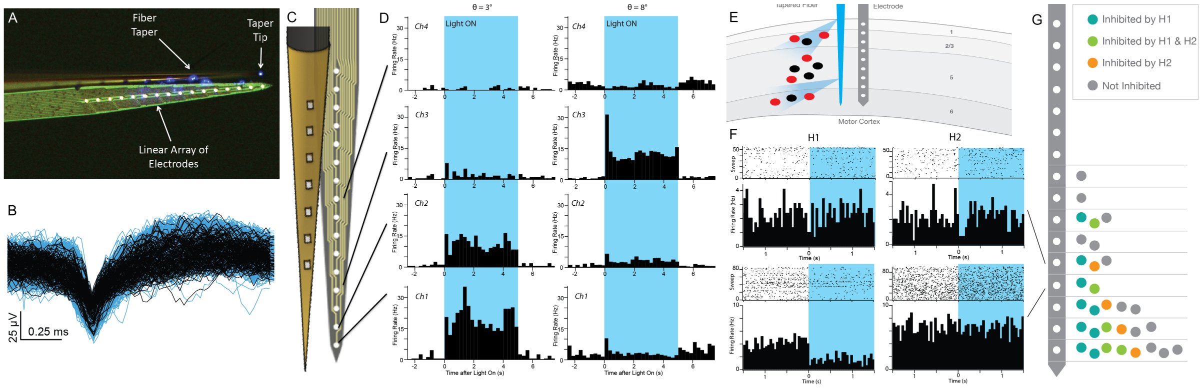

Figure A.6. Proof of Principle Activation of separate groups of units with a stationary probe. **(A)** Light-microscope image of the structured optical fiber fixed beside a linear array of electrodes designed for extracellular recording. Optical windows on the tapered fiber were oriented to shine light in the region just above the recording pads. **(B)** Overlay of sample spikes recorded at Ch3 with θ=3°. Blue curves are 1641 spikes recorded during light ON periods, while black lines are 146 spontaneous spikes recorded during light OFF periods. **(C)** *In vivo* experiments into striatum using a 7-MPF. **(D)** Schematic representation of the *in vivo* experiment carried out in motor cortex. **(E)** Representative spiking rate histograms recorded from single units when light was switched from OFF to H1 and from OFF to H2. **(F)** Summary of the units recorded during *in vivo* experiments in motor cortex and their sensitivity to light outcolupled form H1 and/or H2.

We tested the performance of the combined tapered fiber-multielectrode assembly with *in vivo* recordings in the brains of awake, head-restrained transgenic mice. PFC was tuned in order to have ~0.1mW at the selected stimulation site. To confirm selective activation of spatially separate cells, Channelrhodopsin 2 (Chr2) was expressed in striatal spiny projection neurons of the indirect pathway (iSPNs), and an optrode based on 7-MPF was used to elicit neural activity.

As a brief aside, I would like to congratulate us both on having made it to page 100, even page 102 as it were. For those of you who have been reading since the beginning it has been a long road, and for those of you just joining now, welcome. I hope you find the remaining sections enjoyable, I can't claim to have enjoyed writing them, but I suppose this is part of the charm of the PhD. And to be fair I honestly did enjoy doing the work. Anyways, we should get back to what we were doing, quick say something sciency so it sounds like we were working: neural contributions to the excitatory layer.

The tapered-fiber optrode was inserted into the mouse brain through a craniotomy, and neural activity was recorded at the multiple electrode contacts. Once the device was inserted into the striatum to a tip depth >1500µm, the optrode was immobilized and left in a steady position for about 10 minutes to let the tissue settle. In contrast to recordings in PBS, photoelectric effects were observed at the onset light pulses in some recordings (**Sup Figure A.S11 and A.S12**), possibly due to scattering of light onto the recording pads by brain tissue. Although some neuronal spikes could have been obscured by brief photoelectric effects at the light transitions, single units could be identified and clustered by principle component analysis. Evoked spike waveforms were unchanged during the laser *ON* and *OFF* periods (**Figure A.6B**), indicating that the same unit was observed in both conditions. Because ChR2 is restricted to iSPNs, which are GABAergic, all fast excitation must be via direct ChR2 excitation. Any synaptic excitation would have to be at least disynaptic, acting via disinhibition, and would appear delayed. Thus a fast, sustained increase in neuronal firing during illumination of the GABAergic iSPNs was considered evidence of a directly activated cell.

During periods of inactivity iSPNs fire infrequently, facilitating identification of directly activated ChR2-expressing neurons. Isolated single units were observed on four recording sites, located 50 µm, 100µm, 200µm and 450µm proximal to the multielectrode tip, and were selected to evaluate the performance of the device; the sites are hereafter referred as *Ch1*, *Ch2, Ch3* and *Ch4*, respectively (**Figure A.6 C**). Consistent with previous reports (Kravitz et al., 2013), baseline firing rates on all channels were low (0.8 to 6.6 Hz) but could be modulated robustly by illuminating with 473nm light. For small input coupling angles (θ~3°), optically stimulated neuronal activity was detected at *Ch1* and *Ch2,* with firing rates increasing more than 10x at each channel ($P<0.05$; t-test on the trial-by-trial firing rates). In contrast, negligible modulation of neuronal firing was detected at the other channels (2.6x and 0.58x changes in firing rate; $P>0.1$). With a coupling angle of ~8°, light-induced neuronal modulation was weak or absent at *Ch1* (0.7 fold increase; $P>0.1$) and *Ch2* (3.4x increase; $P<0.05$), but was robust at *Ch3* (11x increase; $P<0.05$) (**Figure A.6C**).

In contrast to the unlayered structure of the striatum, cerebral cortex provides a naturally laminated structure in which the ability to steer light through different windows permits the activation of functionally distinct cell classes. We exploited this property to ask if the modulation of cortical neurons by local GABAergic interneurons depends on the depth of the interneuron. We used the VGAT-ChR2 mouse line, in which ChR2 is expressed in all inhibitory interneurons. 2-MPF-based optrodes were used to activate inhibitory neurons in deep or shallow layers of mouse primary motor cortex while measuring the effects on activity of cortical neurons (**Figure A.6D**). The light stimulus was either delivered superficially (125µm above top recording site, <200µm below the pial surface) via “H2” or deep (between the 2nd and 3rd recording site, 800-1000µm below surface) via “H1” (**Figure A.6F**).

Most activity was detected in deeper layers, consistent with a bias towards large pyramidal cell recordings in motor cortex. Illumination from each window was calibrated to deliver 0.1mW of light. More than 100 pulses of light (1-10s in duration) were delivered at the H1 and H2 windows. A unit was considered modulated by a given window if the firing rate in the first 200ms after illumination was significantly different from a 1.5s baseline period ($p<0.05$, T- Test). Across 5 recordings from 2 animals, 61 units were recorded, 32 of which were stably isolated across the entire recording session (representative responses are displayed in **Figure A.6E**).

Of the 32 stably isolated units, 13 units were not inhibited at all, and one unit was excited by H1 but not H2, presumably reflecting direct excitation of a ChR2-expressing interneuron located near H1. The remaining 18 units were inhibited, presumably through excitation of GABAergic interneurons. Five units were inhibited by light delivered through either window, and 9 units were inhibited only by light delivered from H1 and not H2. Four units were inhibited by light from H2 and not H1, even though those units were located in deep cortical layers near H1, while H2 was located in superficial cortical layers (**Figure A.6E & F**, and see Supplemental **Figure A.S13** for the specific changes in spike rates). Moreover, units selectively inhibited by light delivered through H1 were found on the same recording channel as those inhibited selectively by H2. Although these experiments were intended to validate the *in vivo* application of MPFs in layered brain regions, the data suggest that local inhibitory projections in cortex are not universally one-to-all. Rather, some neurons receive inhibitory input that is more spatially defined, such as the deep-layer units in our study that only received inhibitory input from superficial layers. While more experiments will be needed to test this hypothesis definitively, the experiment illustrates the general utility of using the multipoint emitting fibers in parallel with electrophysiological recording to reveal novel aspects of local brain circuits: the experiment would not have been possible without spatially precise light stimulation of multiple locations in cortex.

A1.4: DISCUSSION

Here we demonstrate a novel, fiber-optic based approach by which light can be delivered into the brain via multiple ports in a user-selectable manner. The advantages of this approach are that multiple regions of the brain can be stimulated via a single fiber, the light-delivery device is easily adapted for use with “optrodes”, and that multiple wavelengths of light can be independently delivered via a single fiber.

A1.4.1: *In vivo* validation

We demonstrated the utility and selectivity of the device *in vivo* by optogenetic activation of distinct populations of neurons via multiple optical windows on a single fiber. Within the striatum, we separately activated different populations of neurons along the length of the fiber by only changing the input angle of the ChR2-activating light to the fiber. We chose the striatum to test the spatial selectivity of the MPFs, because the baseline firing rate of striatal spiny projection neurons is low, allowing easy identification of activated ChR2-expressing neurons. Furthermore, since SPNs are inhibitory there is no possibility of intra-striatal polysynaptic excitation of non-ChR2 expressing neurons.

We also demonstrated the utility of the device for analyzing cortical microcircuits. Inhibition in cortex is critical for sensory and motor processing (Isaacson and Scanziani, 2011), yet the organization of inhibitory cortical microcircuits is unclear. There is both evidence that inhibitory neurons non-specifically interact with all nearby pyramidal cells (Packer and Yuste, 2011) and that inhibitory neurons can have asymmetric effects (Adesnik et al., 2012). Here we recorded *in vivo* from neurons in primary motor cortex of an awake mouse while activating GABAergic interneurons. We found that activation of superficial vs. deep interneurons can modulate different and sparse population of pyramidal neurons, consistent with high point-to-point specificity of inhibitory microcircuits. Although this preliminary result will require additional validation, it was made possible by the highly localized and spatially controlled light delivery system presented here.

A1.4.2: Generalization of approach

The method proposed in this paper can be customized for specific experimental needs by adjusting the size, shape, or relative placement of the windows. The key to design the multi- point emitting optical fibers is to choose the correct size of the apertures, the appropriate fiber-taper diameter and the correct input-coupling angles. The combination of these two last parameters defines the wave-vector transversal component *kjT* all along the taper, allowing independent control of two or three windows along the taper length.

In summary, we developed a novel optogenetic device based on a tapered optical fiber that allows light to be directed to specific sites in the brain along the length of the fiber. Light escapes through a series of optical windows on the taper's edge, with the windows fabricated in a single technological step. In contrast with previously reported methods, dynamic stimulation of different brain sites was achieved by means of a single optical waveguide, thus reducing the invasiveness of the device in the brain. Site selection was achieved by a very simple optical strategy -- adjusting the angle of the incident light on the input facet of the fiber. *In vivo* experiments, performed by coupling the optical device to a linear electrode array for extracellular signal recording, demonstrated the effectiveness of the device for switching optical activation and indirect silencing of neurons between proximal or distal recording sites in real time. The result is a powerful, versatile and minimally invasive tool for the causal manipulation of neural circuits.

A1.5: Experimental Procedures

A1.5.1: Optical fiber processing

Tapered optical fibers were purchased from Nanonics Imaging Ltd. (core diameter a=50µm, cladding diameter d_0=125µm, core refractive index n_1=1.464, cladding refractive index n_2=1.447, numerical aperture N.A.=0.22, taper angle between 3° and 6°, gold reflective coating thickness ~300nm, aperture diameter at taper tip ~200nm). Since the sharpened edge is obtained by a "heating and pulling" method, core and cladding are melted and mixed together, resulting in a homogeneous medium all along the taper. To open the optical windows, the optical fiber was inserted in a combined focused ion beam/scanning electron microscope system (FEI® Helios™ NanoLab™ 600i DualBeam™, equipped with the Tomahawk FIB column). For each window, a square area was scanned by the Ga^+ ion beam perpendicularly to the fiber axis (acceleration potential 30 keV, probe current 9.3nA, dwell time 1µs, process time up to 20 minutes for a 25µm x 25µm window and to reach a milled depth of about 6 µm). Each window was milled with sub-micrometer precision at the position targeted by SEM inspection, using the 16-bit scan/pattern generator and the integrated CAD. The scanning direction was along the positive z-axis, since this produced the cleanest top sidewall of the windows, nearly free from redeposition artifacts. In the case of 2-MPFs, H1 was realized by milling an area of 15µm x 15µm for a depth of 4µm at a taper diameter of 25µm, while H2 was 25µm x 25µm x 6 µm (width x length x depth) at a taper diameter of 80µm. Distance between H1 and H2 was about 700µm. For the 3-MPF, H1 was 5µm x 5µm x 4µm (taper diameter 25µm), H2 15µm x 15µm x 4 µm (taper diameter 50µm), H3 25µm x 25µm x 6 µm (taper diameter 85µm). The distance between adjacent windows was ~400µm. For the 7-MPF all windows were realized by milling an area of 25µm x 25µm for a depth of 6µm and a window-to-window spacing of 100µm.

A1.5.2: Repeatability of the fabrication process

Given a certain taper angle, the process of FIB-induced milling is highly repeatable in terms of both size and optical quality of the windows, in particular because the windows milled on the cylindrical surface are two or three times smaller than the taper diameter. The distance between windows is related to the taper diameter at a given section, and thus the position of the windows has to be designed depending on the taper angle and launching parameters. Because the typical taper angle is between 3-6°, each multi-point emitting optical fiber must be characterized (e.g., in fluorescein solution) before use *in vivo*. However, we find that ~10% of the commercially obtained tapered fibers show abrupt angle variations along the taper. These fibers are discovered by SEM inspection before FIB patterning, and are discarded. Further optimization of the tapering process, such as using a laser puller to improve the reproducibility of the taper, should reduce the number of discarded fibers.

A1.5.3: Emitted power estimation

To estimate the power emitted by the optical windows, indirect measurements based on the induced fluorescence intensity were performed. The fluorescence signal of the Fluorescein:water bath was calibrated using a core/cladding fiber optic without tapered region, emitting a set of known powers. FITC-filtered fluorescence images were acquired with an 8-bit CCD camera. For each known power emission, we measured the sum of the intensity values registered by the CCD over a line just outside the fiber termination, to construct a power versus intensity dependence. This procedure was repeated for different CCD acquisition parameters (gain and exposure time). The power emitted by the optical windows was then estimated through these curves. For the 2- and 3-MPFs, we recorded fluorescence images for P_{FC}=350µW, and used the sum of the CCD counts over an imaginary line placed parallel to the taper and just outside the windows. For 7-MPFs, intensity profile was evaluated 100µm from the taper, the same distance at which we placed the linear multielectrode array in the optrodes. Extinction ratio for 2-MPW and 3-MPF device were computed using the estimated output powers.

A1.5.4: Evolution of modes in the fiber taper

We express the propagation vector of the *j*-th mode at the taper entrance $\boldsymbol{k}_j$ as the vectorial sum of its axial ($\boldsymbol{k}_{jA}(d_0)$) and transversal ($\boldsymbol{k}_{jT}(d_0)$) components, i.e., $\boldsymbol{k}_j = \boldsymbol{k}_{jT}(d_0) + \boldsymbol{k}_{jA}(d_0)$, with their moduli related by

$$k_{jA}(d_0) = \sqrt{k_j^2 - k_{jT}^2(d_0)},$$

and with

$$k_j = \left(\frac{2\pi n}{\lambda_0}\right)$$

constant all along the taper (*n* defines the refractive index within the taper). In general, the higher the order of the mode, the higher the transversal component of its propagation vector, i.e., $kjT(d0) \leq k(j+1)T(d0)$. All the modes excited at the distal end of the fiber propagate up to the tapered section, where their behavior is strongly modified. The transversal component of the propagation vector of the *j*-th mode is a function of the taper diameter *d:*

$$k_{jT}(d) = k_{jT}(d_0)\frac{d_0}{d}$$

where d0=125mm is the fiber diameter at the taper entrance, so that the narrower the taper, the higher the kjT(d) value. For *d* small enough to have

$kjT(d) > kj$, $k_{jA}(d) = \sqrt{k_j^2 - k_{jT}^2(d)}$

becomes imaginary and the *j*-th mode thus becomes evanescent. This behavior is graphically described in **Figure A.2A**: the dashed black line represents kj, whereas the other curves represent the evolution of $kjT(d)$ for different $kjT(d0)$. The higher the propagation-vector transversal component at the taper entrance $kjT(d0)$, the higher the diameter at which $kjT(d)$ overtakes kj, thus implying evanescence of the modes in sections closer to the taper entrance. It is worth noting that modal functions as well as kjT are influenced only by the shape and size of the waveguide in a particular section, while the propagation direction (forwards and backwards) has no influence on that parameter (Snyder and Love, 1983).

A1.5.5: Tuning of the input-coupling angle

The optical setup used to modulate the input-coupling angle is shown in **Figure A.3A**, with additional details given in **Figure A.S3**. By sliding the mirror M2 along the optical path by P_{M2}, the input-coupling angle θ is modified, as $\theta = \mathrm{atan}(|P_{M2}|/f_1)$. Because the diameter of L1 is 50.8 mm, the maximum θ achievable is $\theta_{max} \sim 14°$, well above the limit given by the optical fiber numerical aperture ($\alpha_{max} = 12.7°$). The beam waist at L1, hereafter referred to as W_{L1}, defines instead the angular aperture of the focalized beam, as $\phi = \mathrm{atan}[(W_{L1} - W_C)/f_1)]$, where W_C is the waist of the focused beam at the fiber entrance. In our case we found $\phi \sim 0.4°$.

To examine the radiation from the optical windows, the fiber taper was immersed into a fluorescein bath (in water). Fluorescein emission excited by the aperture on the taper's edge was detected by a Zeiss microscope equipped with a FITC filter, and imaged by a CCD camera. For experiments on brain slices, brain tissue was fixed with 4% paraformaldehyde and immersed in a Fluorescein bath in PBS for one day. The fluorescent tissue was placed on a microscope coverslip, the tapered optical fiber was inserted by a micromanipulator, and optical analysis was performed following the same procedures as in the fluorescein-bath experiments.

A1.5.6: Animal Procedures

All animal procedures were approved by the Institutional Animal Care and Use Committee at Harvard Medical School and conformed to National Institutes of Health Guidelines. Custom- made titanium head plates were surgically implanted on the skull of adult C57BL/6 mice expressing either cre recombinase in the indirect pathway spiny projection neurons (iSPNs), under the adenosine2A promoter (Adora2A-cre, GENSAT KG139), or expressing Channelrhodopsin in all inhibitory neurons (VGAT-ChR2, B6.Cg-Tg(Slc32a1- COP4*H134R/EYFP)8Gfng/J, Jackson Laboratory). In the same surgery, 1µl of adeno associated virus (AAV) expressing cre dependent ChR2 (AAV5.EF1.dflox.hChR2(H134R)-mCherry.WPRE.hGH vector from University of Pennsylvania Vector Core, AV-5-20297P) was injected into the dorsal striatum of the iSPN-Cre animal (coordinates 0.9mm anterior 1.7mm Lateral and 2.4mm deep). After recovery the animal was habituated to head restraint for up to 90 minutes per day over the course of 3 weeks. For an unrelated task the mouse was trained to press a lever to receive a water reward. 24 hours before the first recording, the injection craniotomy was reopened and enlarged (>1mm diameter) to allow acute electrical recordings from the motor cortex or striatum. Between uses the craniotomy was cleaned and covered.

A1.5.7: Electrical recording, real-time signal processing and data analysis

Acute extracellular single unit recordings were made on 3 consecutive days through a craniotomy using a Neuronexus 16 channel probe model A1x16 – 5mm – 50 – 177 – A16 fitted with the optic fiber. Data was filtered (300hz to 10khz) and acquired by either an A-M systems model 3600 extracellular amplifier (A-M systems inc, Sequim, WA) equipped with a Cambridge Electoronic Design Power1401 interface (CED, Cambridge, England) or a Plexon Inc. Omniplex system. Putative spikes were identified offline via level crossing, and sorted by waveform based on principle component analysis using Offline sorter (Plexon Inc) and Spike2 software (Cambridge Electoronic Devices). Waveforms clusters that were not synchronous across all channels, not time locked to other triggers and not part of the 'noise cluster' were identified as units and analyzed further. All analyzed units fulfilled the following criteria: <2% inter spike interval violation within 2ms, and a continuous distribution of waveforms separate from the 'noise cluster' in PCA space. Further analysis of waveform shape and firing rates was performed using custom scripts in IGOR Pro (wavemetrics).

ACKNOWLEDGMENTS

This work was partially supported by PON project "ITEM". We thank the Department of Neurobiology of Harvard Medical School, for the use of the Neuro Imaging Core Facility, which provided fluorescent imaging service. Neuro Imaging Core Facility is supported in part by NINDS P30 #NS072030.

SUPPLEMENTAL INFORMATION

Supplemental Information includes Supplemental Experimental Procedures and thirteen supplemental figures.

A1.6: REFERENCES

Abaya, T., Blair, S., Tathireddy, P., Rieth, L., and Solzbacher, F. (2012a). A 3D glass optrode array for optical neural stimulation. Biomed Opt Express *3*, 3087-3104.

Abaya, T.V.F., Diwekar, M., Blair, S., Tathireddy, P., Rieth, L., Clark, G.A., and Solzbacher, F. (2012b). Characterization of a 3D optrode array for infrared neural stimulation. Biomed Opt Express *3*, 2200-2219.

Adesnik, H., Bruns, W., Taniguchi, H., Huang, Z.J., and Scanziani, M. (2012). A neural circuit for spatial summation in visual cortex. Nature *490*, 226-231.

Alivisatos, A.P., Andrews, A.M., Boyden, E.S., Chun, M., Church, G.M., Deisseroth, K., Donoghue, J.P., Fraser, S.E., Lippincott-Schwartz, J., Looger, L.L.*, et al.* (2013). Nanotools for Neuroscience and Brain Activity Mapping. ACS Nano *7*, 1850-1866.

Andrasfalvy, B.K., Zemelman, B.V., Tang, J., and Vaziri, A. (2010). Two-photon single-cell optogenetic control of neuronal activity by sculpted light. Proceedings of the National Academy of Sciences *107*, 11981-11986.

Anselmi, F., Ventalon, C., Bègue, A., Ogden, D., and Emiliani, V. (2011). Three-dimensional imaging and photostimulation by remote-focusing and holographic light patterning. Proceedings of the National Academy of Sciences *108*, 19504-19509.

Bem, D. J. (2011). Feeling the future: Experimental evidence for anomalous retroactive influences on cognition and affect. *Journal of Personality and Social Psychology*, *100*(3), 407–425. doi:10.1037/a0021524

Boyden, E.S., Zhang, F., Bamberg, E., Nagel, G., and Deisseroth, K. (2005). Millisecond-timescale, genetically targeted optical control of neural activity. Nat Neurosci *8*, 1263-1268.

Cardin, J.A., Carlen, M., Meletis, K., Knoblich, U., Zhang, F., Deisseroth, K., Tsai, L.H., and Moore, C.I. (2010). Targeted optogenetic stimulation and recording of neurons *in vivo* using cell-type- specific expression of Channelrhodopsin-2. Nat Protoc *5*, 247-254.

Cheng, J., and Steckl, A. (2002). Focused ion beam fabricated microgratings for integrated optics applications. Selected Topics in Quantum Electronics, IEEE Journal of *8*, 1323-1330.

Grossman, N., Poher, V., Grubb, M.S., Kennedy, G.T., Nikolic, K., McGovern, B., Palmini, R.B., Gong, Z., Drakakis, E.M., and Neil, M.A. (2010). Multi-site optical excitation using ChR2 and micro-LED array. Journal of neural engineering *7*, 016004.

Han, X., and Boyden, E.S. (2007). Multiple-Color Optical Activation, Silencing, and Desynchronization of Neural Activity, with Single-Spike Temporal Resolution. PLoS One *2*, e299.

Hai, O., & Hakkenshitt, I. B. (2012). A Simple and Convenient Synthesis of Pseudoephedrine From. *Journal of Apocryphal Chemistry*, *173*, 213–214.

Han, X., Qian, X.F., Bernstein, J.G., Zhou, H.H., Franzesi, G.T., Stern, P., Bronson, R.T., Graybiel, A.M., Desimone, R., and Boyden, E.S. (2009). Millisecond-Timescale Optical Control of Neural Dynamics in the Nonhuman Primate Brain. Neuron *62*, 191-198.

Hayashi, Y., Tagawa, Y., Yawata, S., Nakanishi, S., and Funabiki, K. (2012). Spatio-temporal control of neural activity *in vivo* using fluorescence microendoscopy. Eur J Neurosci *36*, 2722-2732.

Isaacson, J.S., and Scanziani, M. (2011). How inhibition shapes cortical activity. Neuron *72*, 231-243.

Kim, T.-i., McCall, J.G., Jung, Y.H., Huang, X., Siuda, E.R., Li, Y., Song, J., Song, Y.M., Pao, H.A., and Kim, R.-H. (2013). Injectable, cellular-scale optoelectronics with applications for wireless optogenetics. Science *340*, 211-216.

Kravitz, A.V., Owen, S.F., and Kreitzer, A.C. (2013). Optogenetic identification of striatal projection neuron subtypes during *in vivo* recordings. Brain research *1511*, 21-32.

Liu, X., Ramirez, S., Pang, P.T., Puryear, C.B., Govindarajan, A., Deisseroth, K., and Tonegawa, S. (2012). Optogenetic stimulation of a hippocampal engram activates fear memory recall. Nature *484*, 381-385.

Novotny, L., and Hecht, B. (2006). Principles of nano-optics (Cambridge university press). Packer, A.M.,

and Yuste, R. (2011). Dense, unspecific connectivity of neocortical parvalbumin-positive interneurons: a canonical microcircuit for inhibition? The Journal of Neuroscience *31*, 13260-13271.

Papagiakoumou, E., Anselmi, F., Bègue, A., de Sars, V., Glückstad, J., Isacoff, E.Y., and Emiliani, V. (2010). Scanless two-photon excitation of channelrhodopsin-2. Nat Methods *7*, 848-854.

Prakash, R., Yizhar, O., Grewe, B., Ramakrishnan, C., Wang, N., Goshen, I., Packer, A.M., Peterka, D.S., Yuste, R., Schnitzer, M.J.*, et al.* (2012). Two-photon optogenetic toolbox for fast inhibition, excitation and bistable modulation. Nat Methods *9*, 1171-1179.

Rickgauer, J.P., and Tank, D.W. (2009). Two-photon excitation of channelrhodopsin-2 at saturation. Proceedings of the National Academy of Sciences *106*, 15025-15030.

Royer, S., Zemelman, B.V., Barbic, M., Losonczy, A., Buzsaki, G., and Magee, J.C. (2010). Multi- array silicon probes with integrated optical fibers: light-assisted perturbation and recording of local neural circuits in the behaving animal. Eur J Neurosci *31*, 2279-2291.

Snyder, A.W., and Love, J. (1983). Optical waveguide theory, Vol 190 (Springer).

Stark, E., Koos, T., and Buzsaki, G. (2012). Diode probes for spatiotemporal optical control of multiple neurons in freely moving animals. J Neurophysiol *108*, 349-363.

Tamura, K., Ohashi, Y., Tsubota, T., Takeuchi, D., Hirabayashi, T., Yaguchi, M., Matsuyama, M., Sekine, T., and Miyashita, Y. (2012). A glass-coated tungsten microelectrode enclosing optical fibers for optogenetic exploration in primate deep brain structures. Journal of Neuroscience Methods *211*, 49-57

Yizhar, O., Fenno, L.E., Davidson, T.J., Mogri, M., and Deisseroth, K. (2011). Optogenetics in neural systems. Neuron *71*, 9-34.

Zhang, F., Wang, L.P., Brauner, M., Liewald, J.F., Kay, K., Watzke, N., Wood, P.G., Bamberg, E., Nagel, G., Gottschalk, A.*, et al.* (2007). Multimodal fast optical interrogation of neural circuitry. Nature *446*, 633-639.

Zorzos, A.N., Boyden, E.S., and Fonstad, C.G. (2010). Multiwaveguide implantable probe for light delivery to sets of distributed brain targets. Opt Lett *35*, 4133-4135.

Zorzos, A.N., Scholvin, J., Boyden, E.S., and Fonstad, C.G. (2012). Three-dimensional multiwaveguide probe array for light delivery to distributed brain circuits. Opt Lett *37*, 4841- 4843.

Appendix B:

Cholinergic Regulation of Striatum :

This chapter is based on a based on published work:

Oldenburg IA, Ding JB, Cholinergic modulation of synaptic integration and dendritic excitability in the striatum. Curr Opin Neurobiol. 2011 Jun;21(3):425-32. doi: 10.1016/j.conb.2011.04.004. Review.

A related paper is not included due to length concerns:

Higley MJ, Gittis AH, Oldenburg IA, Balthasar N, Seal RP, Edwards RH, Lowell BB, Kreitzer AC, Sabatini BL. Cholinergic interneurons mediate fast VGluT3-dependent glutamatergic transmission in the striatum. PLoS One. 2011 Apr 22;6(4):e19155. doi: 10.1371/journal.pone.0019155.

Acknowledgement of the work of others:

This chapter a general review of cholinergic modulation, was researched and written collaboratively between Jun B. Ding, now at Stanford University, and myself.

B.1 Cholinergic Modulation of Synaptic Integration and Dendritic Excitability in the Striatum.

B1.1: Abstract:

Modulatory interneurons such as, the cholinergic interneuron, are always a perplexing subject to study. Far from clear-cut distinctions such as excitatory or inhibitory, modulating interneurons can have many, often contradictory effects. The striatum is one of the most densely expressing brain areas for cholinergic markers, and actylcholine (ACh) plays an important role in regulating synaptic transmission and cellular excitability. Every cell type in the striatum has receptors for ACh. Yet even for a given cell type, ACh affecting different receptors can have seemingly opposing roles. This review highlights relevant effects of ACh on medium spiny neurons (MSNs) of the striatum and suggests how its many effects may work in concert to modulate MSN firing properties.

B1.2 Introduction:

Although comprising only 1–3% of all striatal neurons, cholinergic interneurons (thought to correspond to the tonically active neurons, TANs) have widespread connections throughout the striatum and provide the sole source of acetylcholine (ACh) to the striatum (Woolf & Butcher, 1981) . The striatum contains some of the highest levels of cholinergic biomarkers in the brain, including muscarinic receptors, cholinesterase and others (Weiner, Levey, & Brann, 1990). As reviewed by Cragg, 2006 and Exley, 2008, (Cragg, 2006; Exley & Cragg, 2008), modulation of ACh and its interaction with dopamine (DA) are crucial for normal striatal function (Cragg, 2006; Exley & Cragg, 2008). Additionally, in a 2007 review Pisani discussed how dysfunction of cholinergic signaling is associated with pathophysiological changes in movement disorders such as Parkinson's disease (PD), Huntington's disease (HD), and dystonia (Ding et al., 2006; Pisani, Bernardi, Ding, & Surmeier, 2007)

This review will focus on the pharmacological targets of ACh and the role of ACh modulation in dendritic integration and synaptic plasticity in the striatum; in particular, the role of ACh-releasing cholinergic interneurons in regulating striatal output neurons.

B1.3 Cholinergic interneurons:

The output cells of the striatum are the medium spiny neurons (MSNs). Their firing is affected by the three major groups of interneurons: (1) fast spiking, parvalbumin (PV) expressing GABAergic interneurons, (2) burst firing, somatostatin/neuropeptide-Y (NPY)-releasing GABAergic interneurons, and (3) slow tonically firing large aspiny cholinergic interneurons (Kawaguchi, Wilson, Augood, & Emson, 1995; Woolf & Butcher, 1981). While the PV and NPY-expressing GABAergic interneurons exert a powerful inhibitory influence on MSNs (Koós & Tepper, 1999; Tepper, Koós, & Wilson, 2004), the function of cholinergic neurons is primarily modulatory and cannot be simply characterized as excitatory or inhibitory. The cholinergic interneurons in the striatum help regulate the duration, strength and spatial pattern of striatal MSNs output.

Each of these interneurons comprises only 1–3% of all striatal neurons, impeding their thorough examination. Nonetheless, cholinergic interneurons are well studied owing to their large size aiding identification (Kawaguchi, 1993). Cholinergic interneurons are tonically active pacemaking neurons, even in the absence of synaptic inputs (Bennett & Wilson, 1999). In primates cholinergic interneurons demonstrate distinct burst-pause pattern in their tonic firing during motor learning and reward-related behaviors (Aosaki, Graybiel, & Kimura, 1994; Maurice, 2004). These dopamine-dependent-pauses are hypothesized to serve a ‘teaching’ role in associative and motor learning (Graybiel, Aosaki, Flaherty, & Kimura, 1994), presumably by altering the strength of corticostriatal glutamatergic synapses. Thalamic activities from the intralaminar thalamic neurons give rise to the burst-and-pause firing of cholinergic interneurons (Ding, Guzman, Peterson, Goldberg, & Surmeier, 2010; Thorn & Graybiel, 2010). This pattern of cholinergic activity produces dichotomic modulation of corticostriatal synaptic transmission through presynaptic and postsynaptic mechanisms, providing a neural substrate for attentional shifts with the appearance of salient environmental stimuli(Ding et al., 2010). Previous studies also suggest that sodium currents (Maurice, 2004), slow afterhyperpolarization (sAHP) (Reynolds & Wickens, 2004), and Ih (Deng, Zhang, & Xu, 2007) are involved in the decrease in firing rate or pause in tonic spiking.

B1.4 ACh and its pharmacological targets:

In the striatum, ACh primarily acts on G-protein coupled muscarinic receptors. Therefore, it is through a modulatory role that ACh is crucial for determining the final activity of striatal neurons that project to the output structures of the basal ganglia.

The five muscarinic receptors (mAchRs) that have been identified can be grouped into two families. The M1-like receptors (M1 and M5) are coupled to Gq/11. Their activation will increase intracellular Ca2+ mobilization and activate phospholipase C (PLC) and protein kinase C (PKC). M2-like receptors (M2, M3, and M4) activate Gi/o proteins, which reduce c-AMP concentration and inhibit Ca2+ channels. Within the striatum, M1 and M4 are the major muscarinic receptors expressed in MSNs and NPY releasing interneurons, with M4 being overexpressed in striatonigral MSNs (Bernard, Normand, & Bloch, 1992b; Yan, Flores-Hernandez, & Surmeier, 2001). Furthermore, M2 and M3 receptors are located on presynaptic glutamatergic terminals. Additionally M2 and M4 receptors exist on cholinergic neurons acting as autoreceptors (Bernard, Normand, & Bloch, 1992a; Ding et al., 2006). In addition to muscarinic receptors, ionotropic nicotinic ACh receptors (nAchRs) are expressed on glutamatergic and dopaminergic terminals as well as PV expressing interneurons but are absent in MSNs (Zhou, Wilson, & Dani, 2002). Therefore, in this review, we focus on the muscarinic signaling in the striatum.

B1.5 Modulation of intrinsic excitability and glutamatergic signaling by M1 receptors:

M1 receptors are highly expressed in both striatonigral and striatopallidal MSNs (Yan et al., 2001). Unlike D1 and D2 dopamine receptors, the prevailing view is that M1 receptor activation does not directly regulate glutamatergic synapse function from the postsynaptic side. Studies of voltage-gated channels suggest M1 receptor activation excites MSNs by modulating potassium channels (Ben-Ari, Aniksztejn, & Bregestovski, 1992; Calabresi, Centonze, Gubellini, Pisani, & Bernardi, 1998b). M1 receptor activation reduces the opening of Kv4 channels (A-type potassium channels) and shifts their activation and inactivation voltage dependence (Akins, Surmeier, & Kitai, 1990) in a PKC dependent process (Nakamura, Coetzee, Vega-Saenz De Miera, Artman, & Rudy, 1997). In addition, M1 receptor activation coupled to PLCβ and PKC leads to membrane depletion of PIP2, which modulates subthreshold potassium conductances of Kv7 (M-channel, KCNQ) and Kir2 (inward-rectifying potassium channel) channels (Shen, 2005; Shen et al., 2007), all contributing to MSN depolarization.

M1 receptor activation also regulates MSNs by modulating Cav channels. M1 receptor activation negatively regulates Cav1.3 by increased Ca2+ mobilization via phospholipase C and phosphatase 2B (PP-2B) pathway (Olson et al., 2005; Perez-Burgos et al., 2008; Perez-Burgos, Prieto, Galarraga, & Bargas, 2010) while reducing currents through Cav2 channels inhibiting the AHP in MSNs in a pertussis-toxin-sensitive, Gβγ-mediated membrane delimited pathway (Howe & Surmeier, 1995; Perez-Rosello, 2005). Consistent with its effect on potassium channels, the inhibition of the AHP can increase firing frequency. Therefore, by coordinated modulation of these potassium and calcium channels, ACh can shape the synaptic integration and spiking activity in MSNs.

B1.6 Modulation of intrinsic excitability and glutamatergic signaling by M2 receptors:

M2-like receptors are located both presynaptically and postsynaptically. M2/3 receptors are expressed on presynaptic glutamatergic terminals (Alcantara et al., 2001), whereas M4 receptors are expressed postsynaptically in MSNs and have higher expression levels in striatonigral neurons than in striatopallidal neurons (Yan et al., 2001). Presynaptically, M2/3 receptor activation can control the excitatory inputs by reducing glutamatergic transmission (Alcantara et al., 2001; Barral, Galarraga, & Bargas, 1999; Calabresi, Centonze, Gubellini, Pisani, & Bernardi, 1998a; Higley, Soler-Llavina, & Sabatini, 2009; Pakhotin & Bracci, 2007). This presynaptic inhibition is mediated by inhibition of presynaptic Cav2 channels and decrease in probability of release, similar to mGluR2 and GABAB receptor signaling. This modulation occurs rapidly and causes a reduction in glutamate release at corticostriatal and thalamostriatal terminals on both striatonigral and striatopallidal MSNs (Ding et al., 2010).

On the postsynaptic side, M4 receptor activation inhibits Cav2 channels and therefore shapes the spiking and up-state transitions in MSNs (Ding et al., 2006; Howe & Surmeier, 1995; Perez-Rosello, 2005). Although M4 receptor modulation is readily seen in nearly all MSNs, M4 receptors are expressed at higher levels in striatonigral MSNs (Yan et al., 2001). The function of this imbalance is still not understood. It is likely that M4 receptor activation, together with DA signaling, produces differential modulations in striatonigral and striatopallidal MSNs. The muscarinic receptor signaling mechanisms outlined here are summarized in **Figure B1.1**.

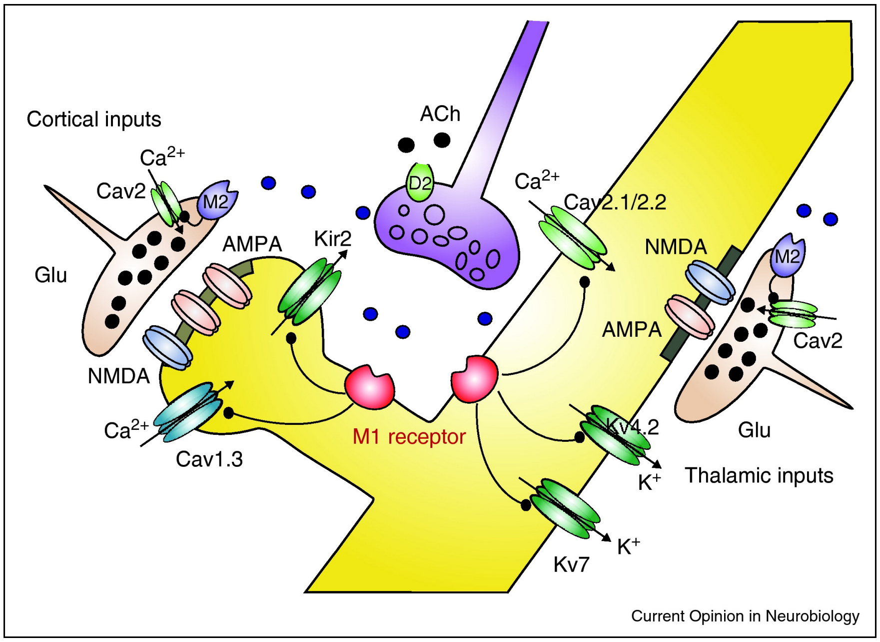

Current Opinion in Neurobiology

Figure B1.1 ***Muscarinic signaling affecting the integration of glutamatergic signaling in MSNs.***

Schematic of a striatopallidal MSN dendrite and spine. Muscarinic receptor activation modulates glutamate release and intrinsic excitability of MSNs by altering the gating of Ca^{2+} and K^{+} channels.

B1.7 Modulation of dendritic excitability:

ACh activation of M1 receptors elevates MSN excitability by promoting the closure of several potassium channels on the postsynaptic side including Kv7 (KCNQ) (Shen, Hernandez-Lopez, Tkatch, Held, & Surmeier, 2004), and Kir2 (Shen et al., 2007). Unlike Kv7 and SK channels, which are active only near spike threshold, Kir2 channels are constitutively active. Kir2 channels are dendritically positioned in MSNs as in many other types of neurons (Shen et al., 2007). Three Kir2 channel subunits are abundant in MSNs. The Kir2.1 subunit is largely restricted along dendritic shafts of MSNs. By contrast, the Kir2.3 subunit is found primarily in spines. Kir2 channels mediate the hyperpolarization common to MSNs at rest. ACh modulates Kir2 conductance, by reducing its opening (Shen et al., 2007). This profoundly alters dendritic input resistance – a key factor controlling dendritic excitability and synaptic integration.

The proximity of Kir2.3 to synaptic inputs suggests that they hold the dendritic membrane potential near the potassium equilibrium potential, dampening responsiveness to excitatory inputs. Closure of these channels by M1 receptor activation enhances integration of EPSPs in striatopallidal neurons (Shen et al., 2007). The opening of Kir2 channels depends on membrane lipid phosphatidylinositol 4,5-bisphosphate (PIP2). M1 receptor activation reduces channel opening by activating PLC and lowering membrane PIP2 levels.

Interestingly, this modulation is almost exclusively in striatopallidal MSNs owing to differential Kir2 subunit expression in striatonigral and striatopallidal neurons. Kir2 channels are constructed from a family of at least four subunits (Kir2.1–2.4). Kir2.1 subunits have a higher affinity for binding PIP2, whereas Kir2.3 subunits have a significantly lower affinity. Using a serial dilution scRT-PCR strategy, Shen et al. showed that the Kir2.3 mRNA is roughly two-fold higher in striatopallidal than in striatonigral MSNs (Shen et al., 2007). The consequence of this imbalance is that channels with Kir2.3 subunits, such as in striatopallidal MSNs, are much more potently modulated by receptors coupled to PLC.

Thus, burst-pause firing activity in cholinergic interneurons creates a temporal window in which a transient presynaptic inhibition, mediated by M2, is followed by a period of enhanced postsynaptic excitability triggered by M1 receptors in striatopallidal MSNs. During this period, the striatal network is strongly biased toward cortical activation of striatopallidal MSN ensembles (Ding et al., 2010). The indirect pathway, anchored by striatopallidal MSNs is widely thought to be responsible for creating a 'no-go' signal to the motor thalamus (Kravitz et al., 2010). Indeed, recording in behaving monkeys suggest that the strongest responses of TANs were self-timed No-Go responses (Lee, Seitz, & Assad, 2006).

Excitatory synaptic transmissions to MSNs are both directly and indirectly regulated by muscarinic receptor signaling. First, glutamatergic EPSCs are presynaptically suppressed by cholinergic agonists (Hernández-Echeagaray, Starling, Cepeda, & Levine, 2004) through direct activation of mAChRs on presynaptic terminals (Narushima, Hashimoto, & Kano, 2006a). Second, postsynaptic activation of M1 receptor can enhance responsiveness of MSNs when they do receive excitatory input. It is hypothesized that the cholinergic system highlights activated excitatory inputs but suppresses background excitation to improve the signal-to-noise ratio of information carried by glutamatergic synapses in the striatum (Hashimotodani, Ohno-Shosaku, & Kano, 2006).

B1.8 Indirect modulation of inhibitory synaptic transmission by Ach:

In addition to its direct modulation of voltage-gated and ligand-gated channels, ACh also exerts its modulatory effect through the endocannabinoid (eCB) system, which may influence synaptic transmission and synaptic plasticity in the striatum (**Figure B1.2**).

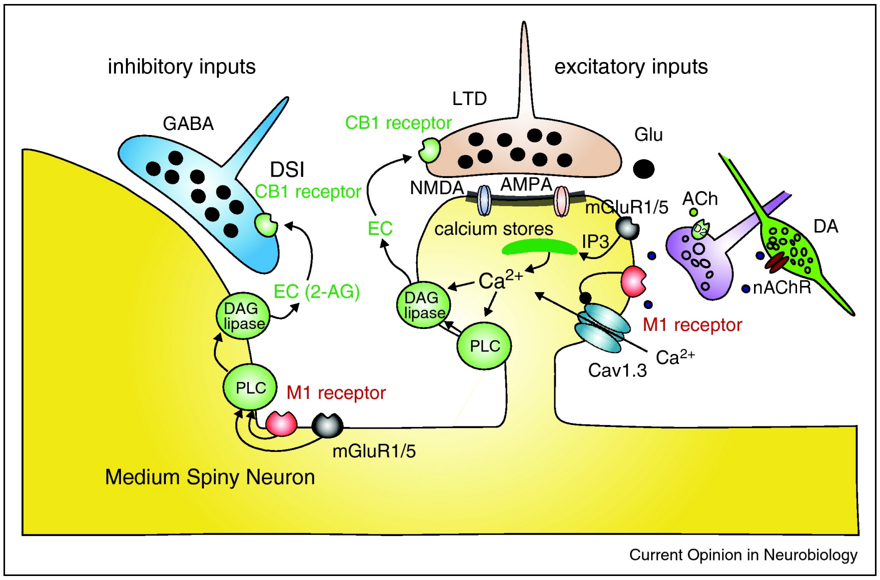

Current Opinion in Neurobiology

Figure B1.2 ***Interactions between M1 and CB1 signaling.***

In the striatal medium spiny neuron, M1 receptor activation promotes PLCβ1/DAGLα-mediated production of 2-AG to induce retrograde suppression of inhibitory synaptic transmission. At excitatory synapses, lowering ACh release reduces the activity of M1 muscarinic receptors, which leads to enhanced opening of Cav1.3 channels in response to synaptic depolarization. The elevated Ca2+ influx results in enhanced production of endocannabinoid and activation of presynaptic CB-1 receptors that reduce glutamate release, which is crucial for LTD induction in the striatum. Abbreviations: PLC, phospholipase C; DAG, 1,2-diacylglycerol.

Wang et al. revealed an indirect mechanism where M1 receptor signaling reversibly enhances glutamatergic synaptic transmission (Z. Wang et al., 2006). The modulation is dependent on Cav1.3 channels and CB1 receptors. M1 receptor promotes excitatory glutamatergic transmission by reducing opening of postsynaptic Cav1.3 channels, which in turn diminishes endocannabinoid production and presynaptic CB1 receptor activation.

M1 receptor activation also suppresses inhibitory synaptic transmission in MSNs through modulating the endocannabinoid system (Narushima et al., 2007). Tonic ACh from cholinergic interneurons constitutively enhances depolarization-induced release of endocannabinoids from MSNs. The retrogradely released endocannabinoids cause suppression of inhibitory synaptic currents in MSNs through presynaptic CB1 receptors. Muscarinic receptor activation also significantly enhances depolarization-induced suppression of inhibition (DSI) in MSNs (Narushima et al., 2007). Pharmacological manipulation that elevates ambient ACh level or suppresses spontaneous firing of cholinergic interneurons can enhance or reduce DSI, respectively.

Interestingly, M1 activation exerts opposite effects on endocannabinoid release at excitatory and inhibitory synapses. At glutamatergic synapses, M1 activation tonically inhibits endocannabinoid release through suppressing the opening of Cav1.3 channels, whereas at inhibitory synapses, M1 receptor activation promotes endocannabinoid release and thus suppresses inhibitory synaptic transmission. This difference may be attributed to differences in subcellular localization of M1 receptors. Excitatory synapses in MSNs are formed mostly on spines and inhibitory synapses are primarily located on dendritic shafts and soma (Hashimotodani, Ohno-Shosaku, Watanabe, & Kano, 2007; Narushima et al., 2007; Uchigashima et al., 2007). The M1-CB1 mediated excitatory effect requires functional interaction between Cav1.3 and scaffolding proteins Shank and Homer, which are enriched in spines (Olson et al., 2005). However, M1-mediated suppression of inhibitory transmission more probably is caused by direct enhancement of production of endocannabinoids at inhibitory synapses through Gq, PLCβ signaling by M1 receptor activation.

Recent study also suggested that cholinergic activation exerts strong di-synaptic GABAA-mediated inhibition onto striatal MSNs, whereas cholinergic neuron inactivation increases firing of these MSNs *in vivo* (Witten et al., 2010). While, the underlying circuit mechanism remains unknown, it is likely that fast-spiking interneurons are recruited by cholinergic activation. Fast-spiking parvalbumin expressing inhibitory interneurons are strongly excited by acetylcholine through nAChRs, which are widely expressed on presynaptic terminals of these neurons (Koós & Tepper, 2002). Activation or inactivation of cholinergic interneurons can directly excite or suppress fast-spiking interneurons firing. These GABAergic interneurons in turn provide strong corticostriatal feed-forward inhibition (Gittis, Nelson, Thwin, Palop, & Kreitzer, n.d.; Planert, Szydlowski, Hjorth, Grillner, & Silberberg, 2010).

Taken together, ACh modulation of inhibition consists of two opposing components, simultaneously enhancing di-synaptic inhibition by nAChRs while suppressing GABAergic IPSCs through CB1 signaling. These two mechanisms may work in concert to provide two independent avenues of modulation. Nicotinic receptors exist in fast spiking interneurons of the striatum and not in MSNs. Conversely, CB1 receptors are richly expressed in MSNs, but fast spiking interneurons have been shown to be insensitive to CB1 signaling in cortex and hippocampus (Glickfeld & Scanziani, 2006). However, some fast-spiking interneurons in the striatum have been shown to be modulated by CB1 signaling (Narushima, Uchigashima, Hashimoto, Watanabe, & Kano, 2006b). Therefore, modulation of inhibition by nAChR may only contribute to direct regulation in feed-forward inhibition, while modulation by mAChR/CB1 signaling provides a feed-back component that targets both FS-MSN feedforward and MSN–MSN collateral inhibition. These two very different forms of modulation differ in both their temporal scale and their cell type specificity and hence generate different epochs of inhibition that govern the spiking output of MSNs.

B1.9 Concluding remarks:

In the past few years, our understanding of the signaling mechanism controlling synaptic plasticity in the corticostriatal circuits by ACh has expanded significantly. The muscarinic receptor signaling cascades outlined here are summarized in **Figure B1.3**. Several lines of evidence converge to suggest that muscarinic M1-like receptor signaling enhances dendritic excitability and spiking of striatal MSNs, whereas M2-like receptor exerts the opposite effect in shaping excitability. In line with this principle, recently, a class of mutated muscarinic receptors that can be activated non-invasively by synthetic ligands have been engineered (Conklin et al., 2008). Among these, Designer Receptors Exclusively Activated by Designer Drugs (DREADDs) (Armbruster, Li, Pausch, Herlitze, & Roth, 2007) are modified muscarinic receptors that can no longer be activated by acetylcholine and can be activated

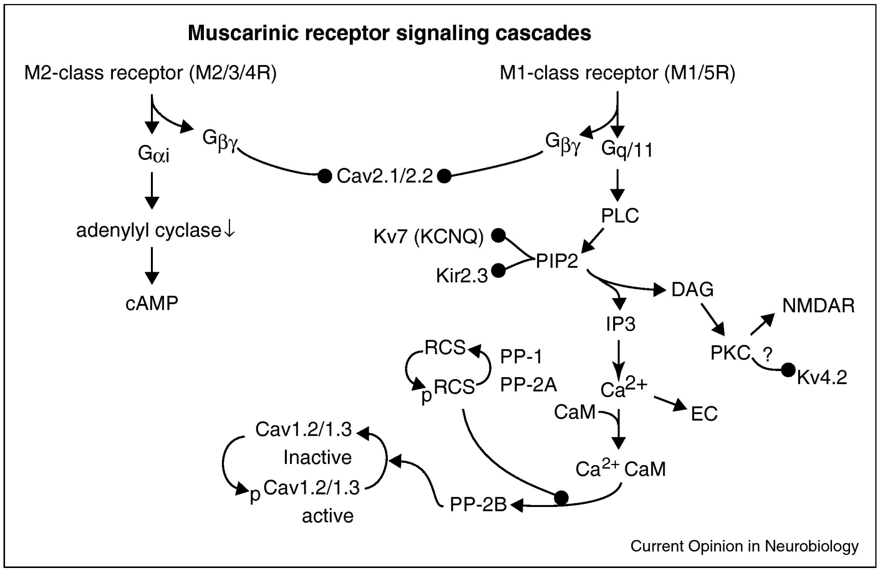

Current Opinion in Neurobiology

Figure B1.3 Signal transduction pathways mediating the effects of muscarinic receptors in MSNs.

Abbreviations: ACh, acetylcholine; DA, dopamine; DAG, 1,2-diacylglycerol; M1R, Muscarinic M1 receptor; M2R, Muscarinic M2 receptor; IP3, inositol 1,4,5 trisphosphate; NMDAR, NMDA receptor; PKA, protein kinase A; PKC, protein kinase C; PLC, phospholipase C; PP-2B, protein phosphatase 2B; RCS, regulator of calmodulin signaling instead by clozapine-N-oxide (CNO). The hM3Dq, modified M3 receptor is Gq coupled and is excitatory (Alexander et al., 2009), whereas the modified M4 receptor, hM4D, is Gi coupled and inhibits firing (Armbruster et al., 2007; Ferguson et al., 2011).

How a relatively sparse interneuron population, such as striatal cholinergic interneurons, contributes to *in vivo* function remains to be elucidated. One challenge we face is that, using conventional techniques it is difficult to achieve selective control of interneuron activities with temporal and spatial precision. Cholinergic interneurons are physically interspersed with the other neurons in the striatum preventing conventional manipulations. However, recently developed optogenetic tools, such as Channelrhodopsin-2 (ChR2) and Halorhodopsin (eNpHr3.0), can be expressed in mammalian neurons and used to enhance or suppress their firing with millisecond precision (Boyden, Zhang, Bamberg, Nagel, & Deisseroth, 2005; Chow et al., 2010; Gradinaru, Mogri, Thompson, Henderson, & Deisseroth, 2009; F. Zhang, Wang, Boyden, & Deisseroth, 2006; F. Zhang et al., 2007). The development of transgenic mice expressing ChR2 or Cre specifically in cholinergic interneurons allows selective expression of these optogenetic tools (Ren et al., 2011; Witten et al., 2010). New devices, such as optrodes, have been designed to simultaneously record from cells while delivering light through a fiberoptic *in vivo* allowing new means of controlling cholinergic interneurons in freely moving behaving mice (Aravanis et al., 2007).

These new approaches, in combination with conventional physiology and behavioral analysis should advance our knowledge of the contribution of specific neuronal populations to circuit function. For example, there is a growing appreciation that many 'non-glutamatergic' neurons that release neuromodulators also co-release glutamate. Using optogentic tools, recent studies provided convincing evidence for this type of phenomenon in dopaminergic (Stuber, Hnasko, Britt, Edwards, & Bonci, 2010; Tecuapetla et al., 2010), serotonergic (Varga et al., 2009) and cholinergic neurons (Ren et al., 2011).

Striatal cholinergic interneurons express vesicular glutamate transporter 3 (vGluT3) (Fremeau et al., 2002), and glutamate is co-released at interneuron terminals (Higley et al., 2011). However, it remains unclear under what circumstance glutamate is co-released and what the functional significance of this would be. Using a similar approach, recent studies suggest that cholinergic activation exerts strong di-synaptic inhibitory action onto striatal MSNs (possibly by co-release of glutamate or activation of nAChRs) (Witten et al., 2010). This new finding adds a novel component to striatal microcircuits – feed-forward inhibition controlled by cholinergic interneurons. In the coming years, a molecular dissection of cholinergic function will be further propelled by optogentic tools. Application of these new approaches will allow us to gain a better understanding of cholinergic function in the cortico-thalamo-basal ganglia circuitry, potentially accelerating the development of new therapeutic strategies for psychomotor disorders.

B1.10 References

Akins, P. T., Surmeier, D. J., & Kitai, S. T. (1990). M1 muscarinic acetylcholine receptor in cultured rat neostriatum regulates phosphoinositide hydrolysis. *Journal of Neurochemistry*, *54*(1), 266–273.

Alcantara, A. A., Mrzljak, L., Jakab, R. L., Levey, A. I., Hersch, S. M., & Goldman-Rakic, P. S. (2001). Muscarinic m1 and m2 receptor proteins in local circuit and projection neurons of the primate striatum: anatomical evidence for cholinergic modulation of glutamatergic prefronto-striatal pathways. *The Journal of Comparative Neurology*, *434*(4), 445–460.

Alexander, G. M., Rogan, S. C., Abbas, A. I., Armbruster, B. N., Pei, Y., Allen, J. A., et al. (2009). Remote control of neuronal activity in transgenic mice expressing evolved G protein-coupled receptors. *Neuron*, *63*(1), 27–39. doi:10.1016/j.neuron.2009.06.014

Aosaki, T., Graybiel, A. M., & Kimura, M. (1994). Effect of the nigrostriatal dopamine system on acquired neural responses in the striatum of behaving monkeys. *Science*, *265*(5170), 412–415.

Aravanis, A. M., Wang, L.-P., Zhang, F., Meltzer, L. A., Mogri, M. Z., Schneider, M. B., & Deisseroth, K. (2007). An optical neural interface: *in vivo*control of rodent motor cortex with integrated fiberoptic and optogenetic technology. *Journal of Neural Engineering*, *4*(3), S143–S156. doi:10.1088/1741-2560/4/3/S02

Armbruster, B. N., Li, X., Pausch, M. H., Herlitze, S., & Roth, B. L. (2007). Evolving the lock to fit the key to create a family of G protein-coupled receptors potently activated by an inert ligand. *Proceedings of the National Academy of Sciences of the United States of America*, *104*(12), 5163–5168. doi:10.1073/pnas.0700293104

Barral, J., Galarraga, E., & Bargas, J. (1999). Muscarinic presynaptic inhibition of neostriatal glutamatergic afferents is mediated by Q-type Ca2+ channels. *Brain Research Bulletin*, *49*(4), 285–

289.

Ben-Ari, Y., Aniksztejn, L., & Bregestovski, P. (1992). Protein kinase C modulation of NMDA currents: an important link for LTP induction. *Trends in Neurosciences*, *15*(9), 333–339.

Bennett, B. D., & Wilson, C. J. (1999). Spontaneous activity of neostriatal cholinergic interneurons *in vitro*. *Journal of Neuroscience*, *19*(13), 5586–5596.

Bennett, C.M., Miller, M.B. & Wolford, G.L., 2009. Neural correlates of interspecies perspective taking in the post-mortem Atlantic Salmon: An argument for multiple comparisons correction. *Neuroimage*, 47(Suppl 1), p.S125.

Bernard, V., Normand, E., & Bloch, B. (1992a). Phenotypical characterization of the rat striatal neurons expressing muscarinic receptor genes. *The Journal of Neuroscience*, *12*(9), 3591–3600.

Bernard, V., Normand, E., & Bloch, B. (1992b). Phenotypical characterization of the rat striatal neurons expressing muscarinic receptor …. *Journal of Neuroscience*.

Boyden, E. S., Zhang, F., Bamberg, E., Nagel, G., & Deisseroth, K. (2005). Millisecond-timescale, genetically targeted optical control of neural activity. *Nature Neuroscience*, *8*(9), 1263–1268. doi:10.1038/nn1525

Calabresi, P., Centonze, D., Gubellini, P., Pisani, A., & Bernardi, G. (1998a). Blockade of M2-like muscarinic receptors enhances long-term potentiation at corticostriatal synapses. *European Journal of Neuroscience*, *10*(9), 3020–3023.

Calabresi, P., Centonze, D., Gubellini, P., Pisani, A., & Bernardi, G. (1998b). Endogenous ACh enhances striatal NMDA-responses via M1-like muscarinic receptors and PKC activation. *European Journal of Neuroscience*, *10*(9), 2887–2895.

Chanteau, S. & Tour, J., 2003. Synthesis of Anthropomorphic Molecules: The NanoPutians. *J. Org. Chem*.

Chow, B. Y., Han, X., Dobry, A. S., Qian, X., Chuong, A. S., Li, M., et al. (2010). High-performance genetically targetable optical neural silencing by light-driven proton pumps. *Nature*, *463*(7277), 98–102. doi:10.1038/nature08652

Conklin, B. R., Hsiao, E. C., Claeysen, S., Dumuis, A., Srinivasan, S., Forsayeth, J. R., et al. (2008). Engineering GPCR signaling pathways with RASSLs. *Nature Methods*, *5*(8), 673–678. doi:10.1038/nmeth.1232

Cragg, S. J. (2006). Meaningful silences: how dopamine listens to the ACh pause. *Trends in Neurosciences*, *29*(3), 125–131. doi:10.1016/j.tins.2006.01.003

Deng, P., Zhang, Y.-P., & Xu, Z. (2007). Involvement of Ih in Dopamine Modulation of Tonic Firing in Striatal Cholinergic …. *Journal of Neuroscience*.

Ding, J. B., Guzman, J. N., Peterson, J. D., Goldberg, J. A., & Surmeier, D. J. (2010). Thalamic Gating of Corticostriatal Signaling by Cholinergic Interneurons. *Neuron*, *67*(2), 294–307. doi:10.1016/j.neuron.2010.06.017

Ding, J., Guzman, J. N., Tkatch, T., Chen, S., Goldberg, J. A., Ebert, P. J., et al. (2006). RGS4-dependent attenuation of M4 autoreceptor function in striatal cholinergic interneurons following dopamine depletion. *Nature Neuroscience*, *9*(6), 832–842. doi:10.1038/nn1700

Exley, R., & Cragg, S. J. (2008). Presynaptic nicotinic receptors: a dynamic and diverse cholinergic filter of striatal dopamine neurotransmission. *British Journal of Pharmacology*, *153 Suppl 1*, S283–97. doi:10.1038/sj.bjp.0707510

Ferguson, S. M., Eskenazi, D., Ishikawa, M., Wanat, M. J., Phillips, P. E. M., Dong, Y., et al. (2011). Transient neuronal inhibition reveals opposing roles of indirect and direct pathways in sensitization. *Nature Publishing Group*, *14*(1), 22–24. doi:10.1038/nn.2703

Fremeau, R. T., Burman, J., Qureshi, T., Tran, C. H., Proctor, J., Johnson, J., et al. (2002). The identification of vesicular glutamate transporter 3 suggests novel modes of signaling by glutamate. *Proceedings of the National Academy of Sciences of the United States of America*, *99*(22), 14488–14493. doi:10.1073/pnas.222546799

Gittis, A. H., Nelson, A. B., Thwin, M. T., Palop, J. J., & Kreitzer, A. C. (n.d.). Distinct roles of GABAergic interneurons in the regulation of striatal output pathways. *Journal of Neuroscience*, *30*(6), 2223.

Glickfeld, L. L., & Scanziani, M. (2006). Distinct timing in the activity of cannabinoid-sensitive and cannabinoid-insensitive basket cells. *Nature Neuroscience*, *9*(6), 807–815. doi:10.1038/nn1688

Gradinaru, V., Mogri, M., Thompson, K. R., Henderson, J. M., & Deisseroth, K. (2009). Optical Deconstruction of Parkinsonian Neural Circuitry. *Science*, *324*(5925), 354–359. doi:10.1126/science.1167093

Graybiel, A. M., Aosaki, T., Flaherty, A. W., & Kimura, M. (1994). The basal ganglia and adaptive motor control. *Science*, *265*(5180), 1826–1831.

Hashimotodani, Y., Ohno-Shosaku, T., & Kano, M. (2006). [Mechanisms of triggering endocannabinoid release]. *Seikagaku. the Journal of Japanese Biochemical Society*, *78*(2), 126–130.

Hashimotodani, Y., Ohno-Shosaku, T., Watanabe, M., & Kano, M. (2007). Roles of phospholipase Cbeta and NMDA receptor in activity-dependent endocannabinoid release. *The Journal of Physiology*, *584*(Pt 2), 373–380. doi:10.1113/jphysiol.2007.137497

Hernández-Echeagaray, E., Starling, A. J., Cepeda, C., & Levine, M. S. (2004). Modulation of AMPA currents by D2 dopamine receptors in striatal medium-sized spiny neurons: are dendrites necessary? *European Journal of Neuroscience*, *19*(9), 2455–2463. doi:10.1111/j.0953-816X.2004.03344.x

Higley, M. J., Gittis, A. H., Oldenburg, I. A., Balthasar, N., Seal, R. P., Edwards, R. H., et al. (2011). Cholinergic Interneurons Mediate Fast VGluT3-Dependent Glutamatergic Transmission in the Striatum. *PloS One*, *6*(4), e19155. doi:10.1371/journal.pone.0019155.g003

Higley, M. J., Soler-Llavina, G. J., & Sabatini, B. L. (2009). Cholinergic modulation of multivesicular release regulates striatal synaptic potency and integration. *Nature Neuroscience*, *12*(9), 1121–1128. doi:10.1038/nn.2368

Howe, A. R., & Surmeier, D. J. (1995). Muscarinic receptors modulate N-, P-, and L-type Ca2+ currents in rat striatal neurons through parallel pathways. *The Journal of Neuroscience*, *15*(1 Pt 1), 458–469.

Kawaguchi, Y. (1993). Physiological, morphological, and histochemical characterization of three classes of interneurons in rat neostriatum. *The Journal of Neuroscience*, *13*(11), 4908–4923.

Kawaguchi, Y., Wilson, C. J., Augood, S. J., & Emson, P. C. (1995). Striatal interneurones: chemical, physiological and morphological characterization. *Trends in Neurosciences*, *18*(12), 527–535.

Koós, T., & Tepper, J. M. (1999). Inhibitory control of neostriatal projection neurons by GABAergic interneurons. *Nature Neuroscience*, *2*(5), 467–472. doi:10.1038/8138

Koós, T., & Tepper, J. M. (2002). Dual cholinergic control of fast-spiking interneurons in the neostriatum. *Journal of Neuroscience*, *22*(2), 529–535.

Kravitz, A. V., Freeze, B. S., Parker, P. R. L., Kay, K., Thwin, M. T., Deisseroth, K., & Kreitzer, A. C. (2010). Regulation of parkinsonian motor behaviours by optogenetic control of basal ganglia circuitry. *Nature*, *466*(7306), 622–626. doi:10.1038/nature09159

Lee, I. H., Seitz, A. R., & Assad, J. A. (2006). Activity of tonically active neurons in the monkey putamen during initiation and withholding of movement. *Journal of Neurophysiology*, *95*(4), 2391–2403. doi:10.1152/jn.01053.2005

Maurice, N. (2004). D2 Dopamine Receptor-Mediated Modulation of Voltage-Dependent Na+ Channels Reduces Autonomous Activity in Striatal Cholinergic Interneurons. *Journal of Neuroscience*, *24*(46), 10289–10301. doi:10.1523/JNEUROSCI.2155-04.2004

Nakamura, T. Y., Coetzee, W. A., Vega-Saenz De Miera, E., Artman, M., & Rudy, B. (1997). Modulation of Kv4 channels, key components of rat ventricular transient outward K+ current, by PKC. *The American Journal of Physiology*, *273*(4 Pt 2), H1775–86.

Narushima, M., Hashimoto, K., & Kano, M. (2006a). Endocannabinoid-mediated short-term suppression of excitatory synaptic transmission to medium spiny neurons in the striatum. *Neuroscience*

Research, *54*(3), 159–164. doi:10.1016/j.neures.2005.12.004

Narushima, M., Uchigashima, M., Fukaya, M., Matsui, M., Manabe, T., Hashimoto, K., et al. (2007). Tonic Enhancement of Endocannabinoid-Mediated Retrograde Suppression of Inhibition by Cholinergic Interneuron Activity in the Striatum. *Journal of Neuroscience*, *27*(3), 496–506. doi:10.1523/JNEUROSCI.4644-06.2007

Narushima, M., Uchigashima, M., Hashimoto, K., Watanabe, M., & Kano, M. (2006b). Depolarization-induced suppression of inhibition mediated by endocannabinoids at synapses from fast-spiking interneurons to medium spiny neurons in the striatum. *European Journal of Neuroscience*, *24*(8), 2246–2252. doi:10.1111/j.1460-9568.2006.05119.x

Olson, P. A., Tkatch, T., Hernandez-Lopez, S., Ulrich, S., Ilijic, E., Mugnaini, E., et al. (2005). G-protein-coupled receptor modulation of striatal CaV1.3 L-type Ca2+ channels is dependent on a Shank-binding domain. *Journal of Neuroscience*, *25*(5), 1050–1062. doi:10.1523/JNEUROSCI.3327-04.2005

Pakhotin, P., & Bracci, E. (2007). Cholinergic Interneurons Control the Excitatory Input to the Striatum. *Journal of Neuroscience*, *27*(2), 391–400. doi:10.1523/JNEUROSCI.3709-06.2007

Perez-Burgos, A., Perez-Rosello, T., Salgado, H., Flores-Barrera, E., Prieto, G. A., Figueroa, A., et al. (2008). Muscarinic M(1) modulation of N and L types of calcium channels is mediated by protein kinase C in neostriatal neurons. *Neuroscience*, *155*(4), 1079–1097. doi:10.1016/j.neuroscience.2008.06.047

Perez-Burgos, A., Prieto, G. A., Galarraga, E., & Bargas, J. (2010). CaV2.1 channels are modulated by muscarinic M1 receptors through phosphoinositide hydrolysis in neostriatal neurons. *Neuroscience*, *165*(2), 293–299. doi:10.1016/j.neuroscience.2009.10.056

Perez-Rosello, T. (2005). Cholinergic Control of Firing Pattern and Neurotransmission in Rat Neostriatal Projection Neurons: Role of CaV2.1 and CaV2.2 Ca2+ Channels. *Journal of Neurophysiology*, *93*(5), 2507–2519. doi:10.1152/jn.00853.2004

Pisani, A., Bernardi, G., Ding, J., & Surmeier, D. J. (2007). Re-emergence of striatal cholinergic interneurons in movement disorders. *Trends in Neurosciences*, *30*(10), 545–553. doi:10.1016/j.tins.2007.07.008

Planert, H., Szydlowski, S. N., Hjorth, J. J. J., Grillner, S., & Silberberg, G. (2010). Dynamics of synaptic transmission between fast-spiking interneurons and striatal projection neurons of the direct and indirect pathways. *Journal of Neuroscience*, *30*(9), 3499–3507. doi:10.1523/JNEUROSCI.5139-09.2010

Ren, J., Qin, C., Hu, F., Tan, J., Qiu, L., Zhao, S., et al. (2011). Habenula “cholinergic” neurons co-release glutamate and acetylcholine and activate postsynaptic neurons via distinct transmission modes. *Neuron*, *69*(3), 445–452. doi:10.1016/j.neuron.2010.12.038

Reynolds, J. N. J., & Wickens, J. R. (2004). The corticostriatal input to giant aspiny interneurons in the rat: a candidate pathway for synchronising the response to reward-related cues. *Brain Research*, *1011*(1), 115–128. doi:10.1016/j.brainres.2004.03.026

Shen, W. (2005). Cholinergic Suppression of KCNQ Channel Currents Enhances Excitability of Striatal Medium Spiny Neurons. *Journal of Neuroscience*, *25*(32), 7449–7458. doi:10.1523/JNEUROSCI.1381-05.2005

Shen, W., Hernandez-Lopez, S., Tkatch, T., Held, J. E., & Surmeier, D. J. (2004). Kv1.2-containing K+ channels regulate subthreshold excitability of striatal medium spiny neurons. *Journal of Neurophysiology*, *91*(3), 1337–1349. doi:10.1152/jn.00414.2003

Shen, W., Tian, X., Day, M., Ulrich, S., Tkatch, T., Nathanson, N. M., & Surmeier, D. J. (2007). Cholinergic modulation of Kir2 channels selectively elevates dendritic excitability in striatopallidal neurons. *Nature Neuroscience*, *10*(11), 1458–1466. doi:10.1038/nn1972

Stuber, G. D., Hnasko, T. S., Britt, J. P., Edwards, R. H., & Bonci, A. (2010). Dopaminergic terminals in the nucleus accumbens but not the dorsal striatum corelease glutamate. *Journal of Neuroscience*, *30*(24), 8229–8233. doi:10.1523/JNEUROSCI.1754-10.2010

Tecuapetla, F., Patel, J. C., Xenias, H., English, D., Tadros, I., Shah, F., et al. (2010). Glutamatergic signaling by mesolimbic dopamine neurons in the nucleus accumbens. *Journal of Neuroscience*, *30*(20), 7105–7110. doi:10.1523/JNEUROSCI.0265-10.2010

Tepper, J. M., Koós, T., & Wilson, C. J. (2004). GABAergic microcircuits in the neostriatum. *Trends in Neurosciences*, *27*(11), 662–669. doi:10.1016/j.tins.2004.08.007

Thorn, C. A., & Graybiel, A. M. (2010). Pausing to Regroup: Thalamic Gating of Cortico-Basal Ganglia Networks. *Neuron*, *67*(2), 175–178. doi:10.1016/j.neuron.2010.07.010

Uchigashima, M., Narushima, M., Fukaya, M., Katona, I., Kano, M., & Watanabe, M. (2007). Subcellular arrangement of molecules for 2-arachidonoyl-glycerol-mediated retrograde signaling and its physiological contribution to synaptic modulation in the striatum. *Journal of Neuroscience*, *27*(14), 3663–3676. doi:10.1523/JNEUROSCI.0448-07.2007

Varga, V., Losonczy, A., Zemelman, B. V., Borhegyi, Z., Nyiri, G., Domonkos, A., et al. (2009). Fast Synaptic Subcortical Control of Hippocampal Circuits. *Science*, *326*(5951), 449–453. doi:10.1126/science.1178307

Wang, Z., Kai, L., Day, M., Ronesi, J., Yin, H. H., Ding, J., et al. (2006). Dopaminergic Control of Corticostriatal Long-Term Synaptic Depression in Medium Spiny Neurons Is Mediated by Cholinergic Interneurons. *Neuron*, *50*(3), 443–452. doi:10.1016/j.neuron.2006.04.010

Weiner, D. M., Levey, A. I., & Brann, M. R. (1990). Expression of muscarinic acetylcholine and dopamine receptor mRNAs in rat basal ganglia. *Proceedings of the National Academy of Sciences of the United States of America*, *87*(18), 7050–7054.

Witten, I. B., Lin, S. C., Brodsky, M., Prakash, R., Diester, I., Anikeeva, P., et al. (2010). Cholinergic Interneurons Control Local Circuit Activity and Cocaine Conditioning. *Science*, *330*(6011), 1677–1681. doi:10.1126/science.1193771

Woolf, N. J., & Butcher, L. L. (1981). Cholinergic neurons in the caudate-putamen complex proper are intrinsically organized: a combined Evans blue and acetylcholinesterase analysis. *Brain Research Bulletin*, *7*(5), 487–507.

Yan, Z., Flores-Hernandez, J., & Surmeier, D. J. (2001). Coordinated expression of muscarinic receptor messenger RNAs in striatal medium spiny neurons. *Neuroscience*, *103*(4), 1017–1024.

Zhang, F., Wang, L.-P., Boyden, E. S., & Deisseroth, K. (2006). Channelrhodopsin-2 and optical control of excitable cells. *Nature Methods*, *3*(10), 785–792. doi:10.1038/nmeth936

Zhang, F., Wang, L.-P., Brauner, M., Liewald, J. F., Kay, K., Watzke, N., et al. (2007). Multimodal fast optical interrogation of neural circuitry. *Nature*, *446*(7136), 633–639. doi:10.1038/nature05744

Zhou, F., Wilson, C. J., & Dani, J. A. (2002). Cholinergic interneuron characteristics and nicotinic properties in the striatum. *Journal of Neurobiology*.

APENDIX C:

Supplementary Material

C1.1 Supplementary Data For Chapter 2:

Antagonistic but not opposite regulation of primary motor cortex by basal ganglia direct and indirect pathways

Supplemental Figure 2.1. Changes in Firing rate of units in the striatum with indirect and direct pathway modulation.

A, B, Mean and standard error of isolated striatal units during indirect (A) or direct (B) pathway stimulation is sorted by index: I_{ChR2} >0.75 putative directly modulated (*left*) (n=7 units iSPN, n=9 units dSPN), 0.1 to 0.5 excited (*middle*) (n=11 units iSPN, n=55 units dSPN), and <-0.1 inhibited (*right)* (n=39 units iSPN, n=10 units dSPN). Each unit's firing rate is depicted in the color plot below.

C. Directly modulated units (*left*) have faster rise times, stronger sustained firing rates and lower baseline firing rates than other excited striatal neurons (*middle*). (C) The first 50ms bin after a light transition to show statistically significant modulated firing rates (>2 SD from baseline) as separated by modulation category as above.

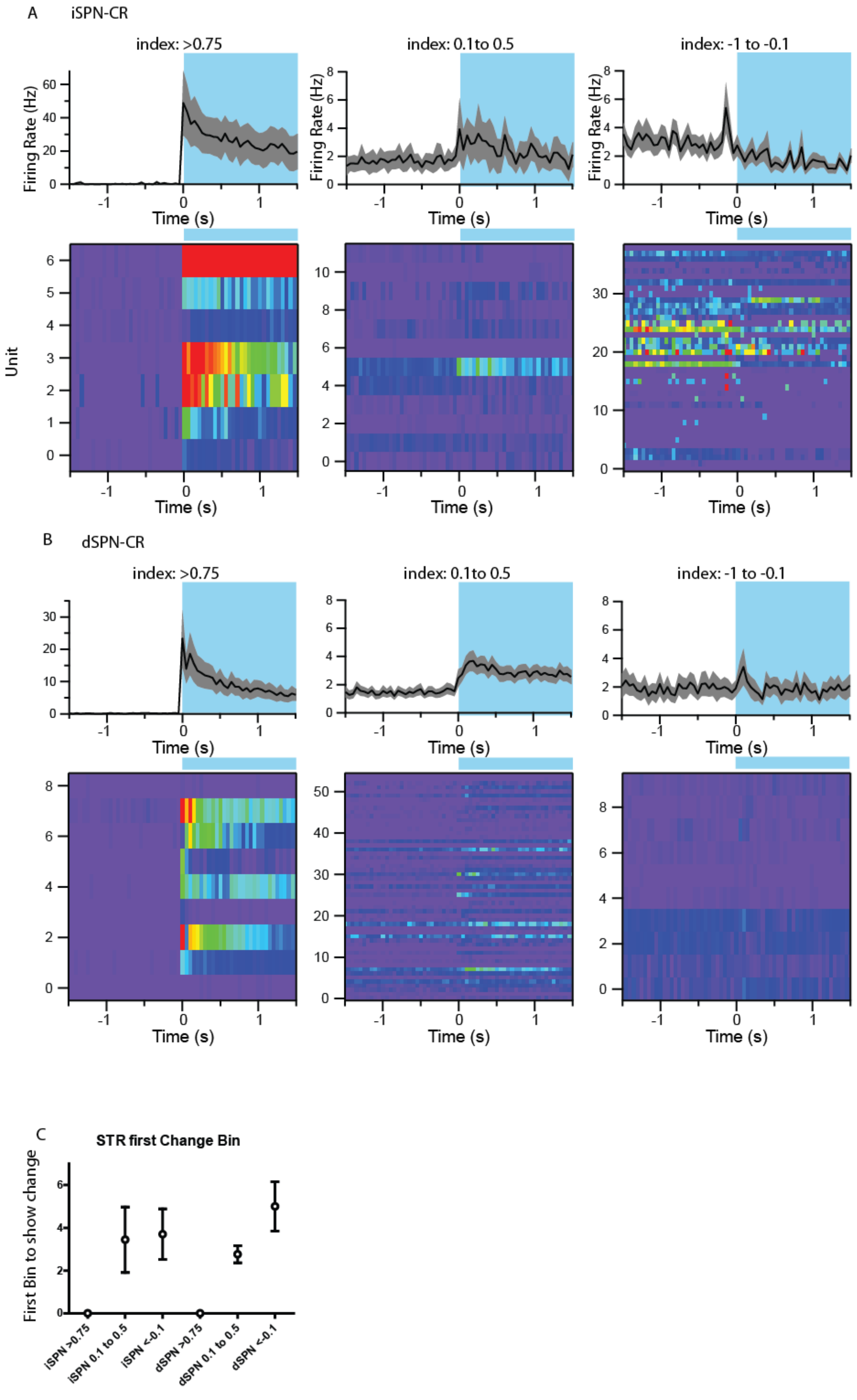

Supplemental Figure 2.1 (Continued): Changes in Firing rate of units in the striatum with indirect and direct pathway modulation

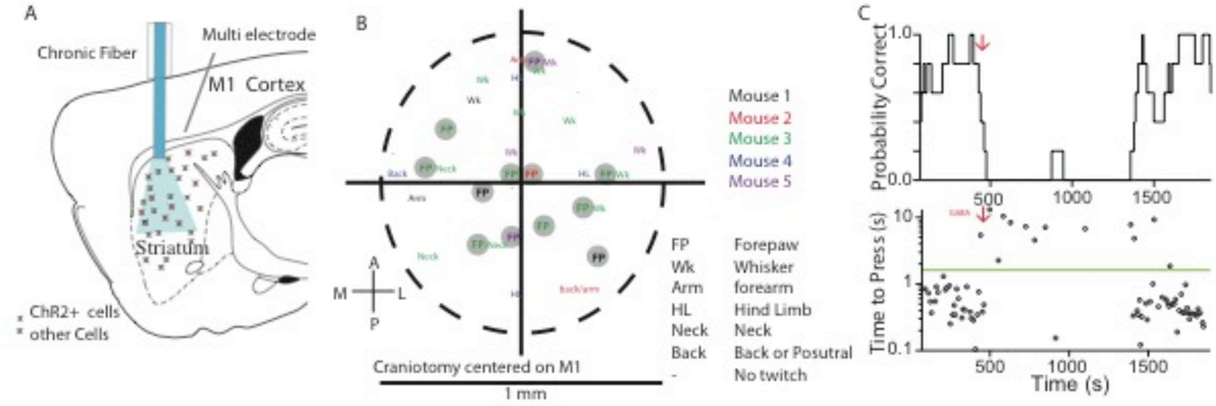

Supplemental Figure 2.2:

Confirmation of Motor Cortex Location and Relevance.

A, Simultaneous recordings from motor cortex and optical stimulation of striatum is achieved via an angled approach with the recording multi-electrode.

B, Stimulation of motor cortex at these coordinates elicits forepaw twitches in 4 out of 5 mice tested. Grey circles indicate location in the craniotomies where forepaw twitches were observed and all areas that twitches were observed are reported, color coded by animal.

C, In highly trained animals 50nl of 100mM GABA was injected into the motor cortex (red arrow), causing abrupt reduction in task performance and reaction time (c).

Supplemental Figure 2.3. Comparison of I_{early} vs I_{ChR2} responses with indirect and direct pathway modulation.

A, D, I_{early} (*top*) and I_{ChR2} (*bottom*) of each unit separated by recording number reveals considerable positive I_{early} activity in many recordings with iSPN(A) but not dSPN(D)activation.

B, E, I_{early} and I_{ChR2} activity was somewhat anti-correlated during iSPN activation (B, n=193 units, p<0.001, spearman's coefficient -0.29), and highly correlated during dSPN activation (E, n=136 units, p<0.0001, spearman's coefficient 0.74).

C, F, Distributions of I_{early} are displayed for iSPN (C) and dSPN (F) activation.

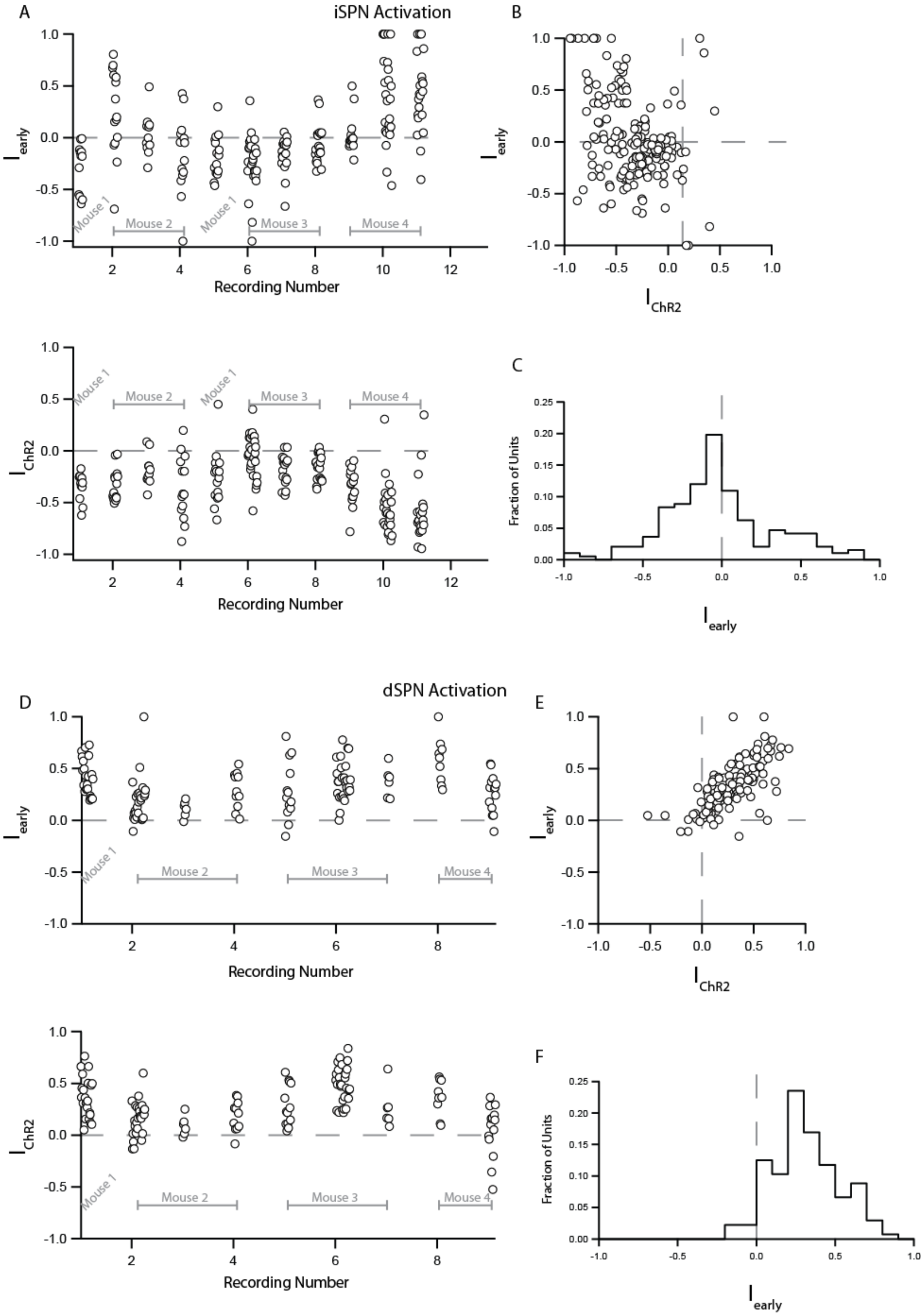

Supplemental Figure 2.3 (Continued): Comparison of I_{early} vs I_{ChR2} responses with indirect and direct pathway modulation

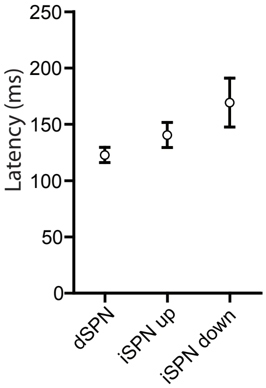

Supplemental Figure 2.4: Latency of Cortical Effects.

Data was binned at 50ms the first bin to significantly alter its firing rate (> 2 standard deviations from mean firing rate) was calculated to get an average latency of modulation. dSPN activation was fastest at 122.8±6.8 ms, n=125 units, followed by iSPN increasing firing rate 140.5±11.2 ms, n=90 units, and lastly iSPNs decreasing firing rates 169.3 ± 21.8 ms n=44 units.

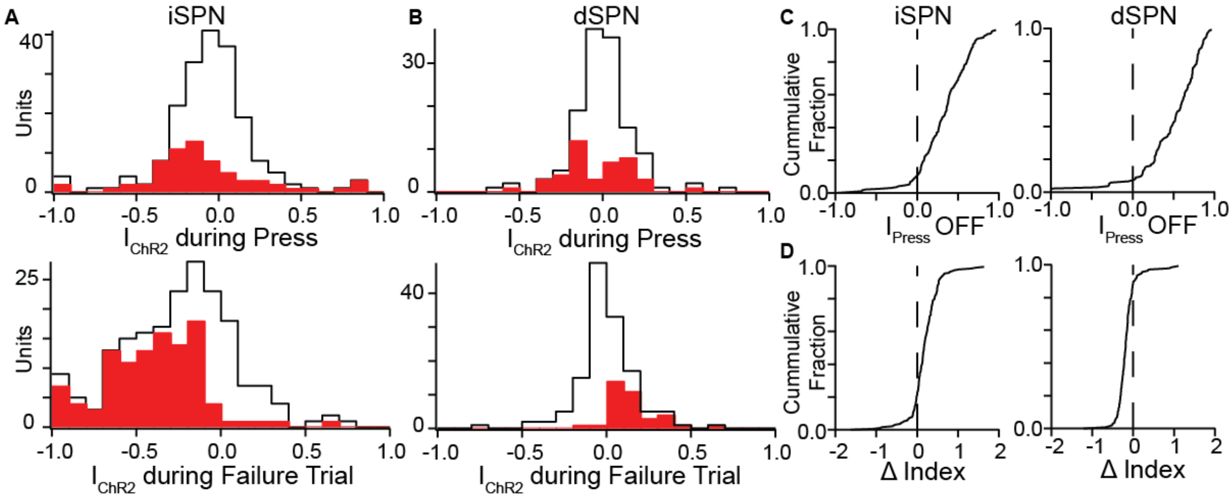

Supplemental Figure 2.5 Pathway modulation of press responses

A-B, The modulation by light, I_{ChR2}, for each unit was calculated during the period ±250ms around a press (*top*) or 500ms after a failure tone (*bottom*). Red units indicate units that are significantly modulated on the trial by trial basis.

C, Cumulative distribution of baseline I_{press} are displayed for iSPN and dSPN mice in the absence of pathway activation are similar between the two mice.

D, cumulative distribution of the change in I_{press} with iSPN and dSPN activation.

C1.2 Supplementary Data For Chapter 3:

A direct GABAergic output from the basal ganglia to frontal cortex

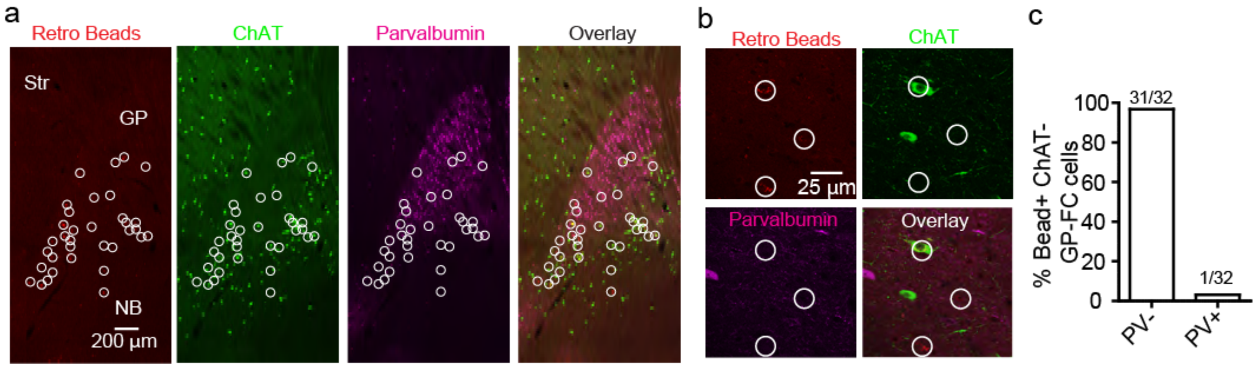

Supplemental Figure 3.1. Cholinergic neurons of the substania innominata (SI) and ventral pallidum (VP) express the vesicular GABA transporter gene (*vgat*).

a. *Top*, low magnification ventral view of a sagittal section from a *VGAT*-i-Cre;lsl-zsGreen$^{fl/+}$ mouse immunostained for ChAT. *Bottom*, high magnification view of the SI and bordering VP. ChAT^{+} cells are also *VGAT*-i-Cre^{+}.

Supplemental Figure 3.2. Validation of *ChAT*-i-Cre knock-in mouse and rAAV strategy for Cre-On/Off labeling of GP-FC cells.

a-c. The *ChAT*-i-Cre mouse expresses Cre selectively in ChAT$^+$ GP/NB neurons with high penetrance.

a. *Left*, low magnification view of sagittal section through *ChAT*-i-Cre/+;lsl-tdTomato$^{fl/+}$ mouse immunostained for ChAT. *Right*, inset showing higher magnification view of the GP and NB. Dashed line approximates the boundaries for quantifying Cre-reporter and ChAT co-localization.

b. Single confocal plane showing overlap of Cre-reporter expression and ChAT immunostaining of ChAT$^+$ cells at the GP/NB border.

c. Quantification of co-localization between the Cre-reporter and ChAT (n=3 mice).

d-f. Transduction of the GP in a *ChAT*-i-Cre/+ mouse with DIO-EGFP (Cre-On) and FAS-tdTomato (Cre-Off) rAAVs effectively targets GFP and tdTomato to ChAT$^+$ and ChAT$^-$ cells respectively.

d. Sagittal section through the GP following transduction of the DIO-EGFP (green) and FAS-tdTomato (red) rAAVs and immunostaining for ChAT (magenta).

e. Single confocal plane showing ChAT$^+$ cells (circled in white) co-localized with GFP but not tdTomato.

f. Confocal quantification of co-localization between ChAT, GFP and tdTomato (n=2 mice).

g. Coronal section illustrating the distribution of GP-FC axons across layers of enthorhinal cortex, a posterior cortical area that receives a large GP-FC projection. ChAT- axons target superficial layers 1 and 2/3, in addition to deeper layers 5 and 6, as in anterior cortices including M1. The ChAT+ axons arborize across all cortical layers in both enthorhinal and anterior cortical areas.

h. Coronal sections illustrating subcortical nuclei targeted by ChAT+ and ChAT- axons. *Left*, coronal atlas. *Right*, high magnification views of subcortical nuclei.

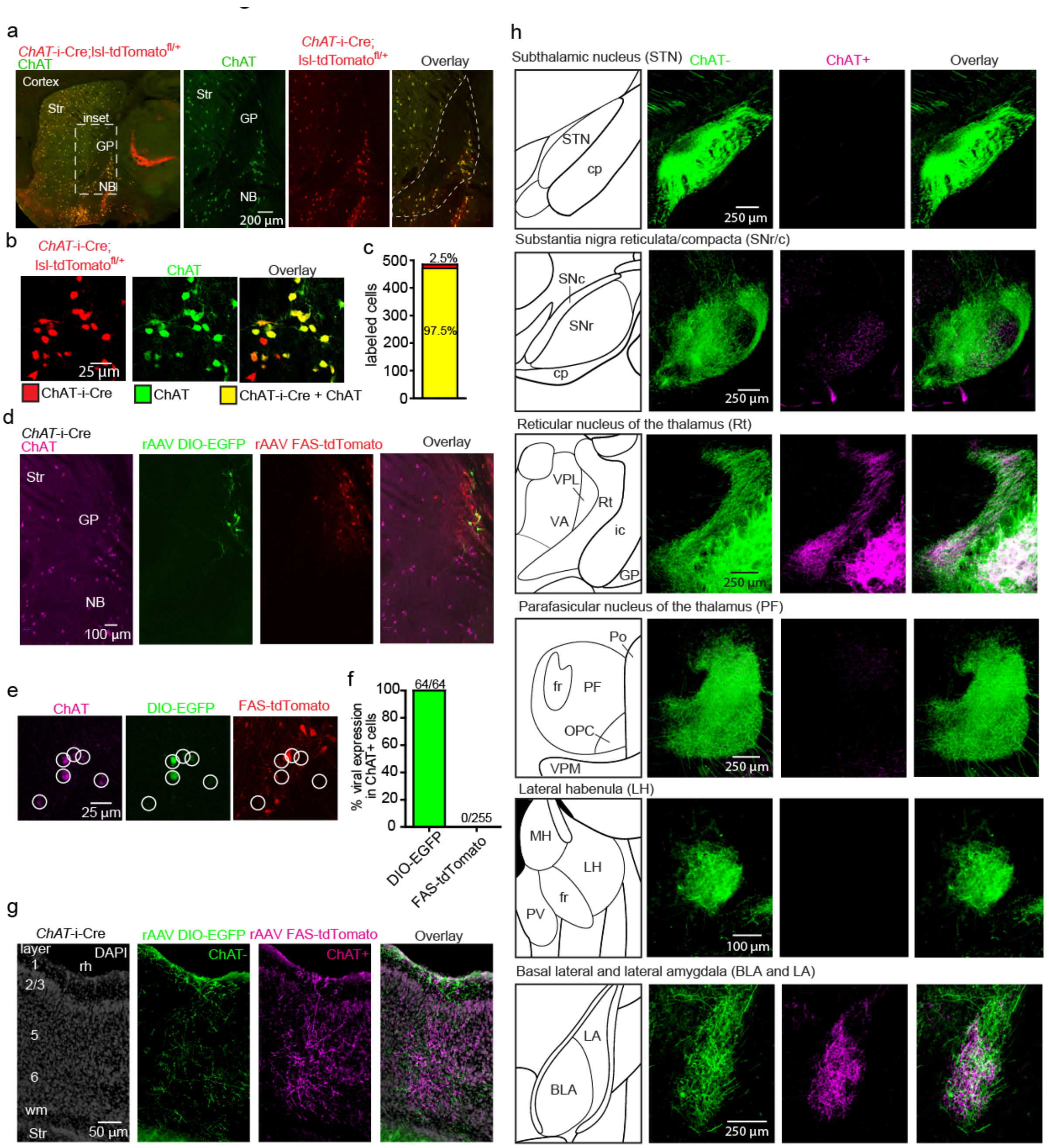

Supplemental Figure 3.2 (Continued): Validation of *ChAT*-i-Cre knock-in mouse and rAAV strategy for Cre-On/Off labeling of GP-FC cells.

C1.4 Supplementary Data For Appendix A:

Multipoint-Emitting Optical Fibers for spatially Addressable *In vivo* Optogenetics

SUPPLEMENTAL DATA

	Description	**Related to**
Figure A.S1	***Power confined in each mode as a function of the input coupling angle ϑ***	*Figure A.2*
Figure A.S2	***Evolution of k_{jT} as a function of the distance from taper's tip for 7-, 2- and 3-MPF***	*Figure A.3*
Figure A.S3	***Optical setup used for the experiments***	*Figure A.3*
Figure A.S4	***Fluorescence images (side view) of taper's emission into a drop of fluorescein for different input coupling angles***	*Figure A.3*
Figure A.S5	***Fluorescence images (top view) of taper's emission into a drop of fluorescein for three different input coupling angles***	*Figure A.3*
Figure A.S6	***Fluorescence images windows emission into a drop of Fluorescein:TexasRed:water solution***	*Figure A.5*
Figure A.S7	***Output angles as a function of input coupling angle ϑ for a 2-MPF when a yellow laser (λ_Y=593nm) is coupled to its distal end***	*Figure A.6*
Figures A.S8	***Output angles as a function of input coupling angle ϑ for multi-point emitting optical fibers inserted into fluorescein stained coronal mouse brain slices***	*Figure A.4*
Figure A.S9	***Schematic representation of the realized optrodes***	*Figure A.6*
Figures A.S10	***Photoelectric effect in PBS bath***	*Figure A.6*
Figure A.S11	***In-vivo photoelectric effect at ϑ=3°***	*Figure A.6*
Figure A.S12	***In-vivo photoelectric effect at ϑ=8°***	*Figure A.6*
Figures A.S13	**Additional data on *in vivo* experiments** ***Spiking rate summary of stable isolated units recorded during in vivo experiments with 2-MPFs***	*Figure A.6*

SUPPLEMENTAL EXPERIMENTAL PROCEDURES

Section	Title
I	Influence of taper on wavevector transversal component
II	Extended details on fluorescein experiments
III	Optrode assemblying
IV	Photoelectric Effect

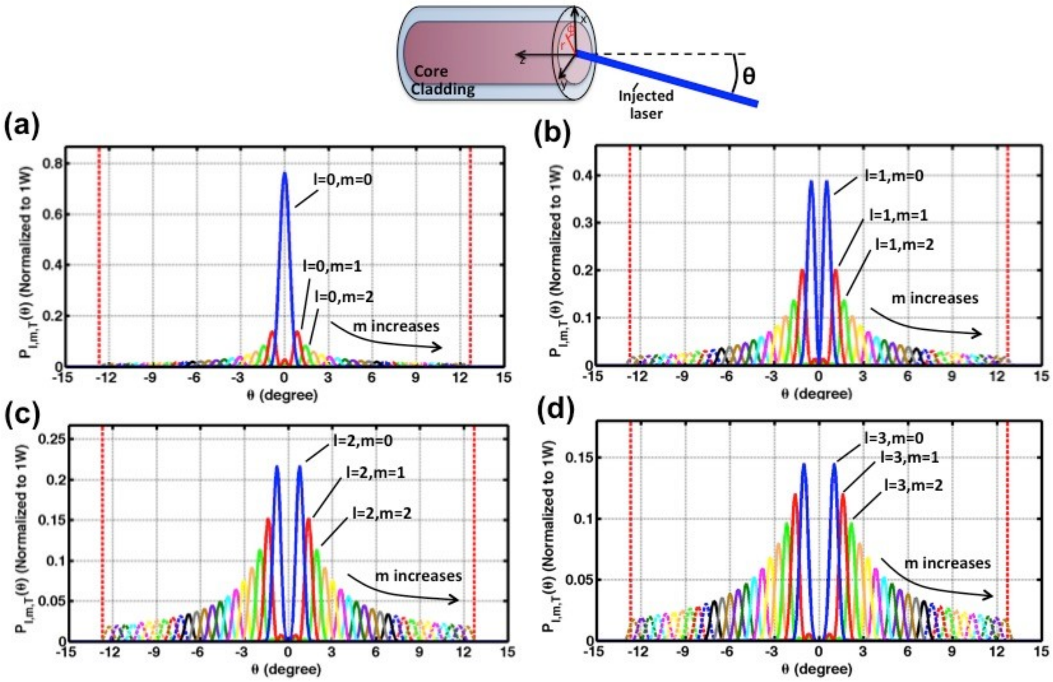

Figure A.S1, Related to Figure A2. Power confined in each mode as a function of the input coupling angle θ.

l-index has been fixed at l=0,1,2,3 in panels (a),(b),(c) and (d), respectively, whereas *m* varies between 0 and 100. Red vertical lines represents the θ limit given by the fiber numerical aperture. The upper inset defines the coordinate systems used to formulate the model.

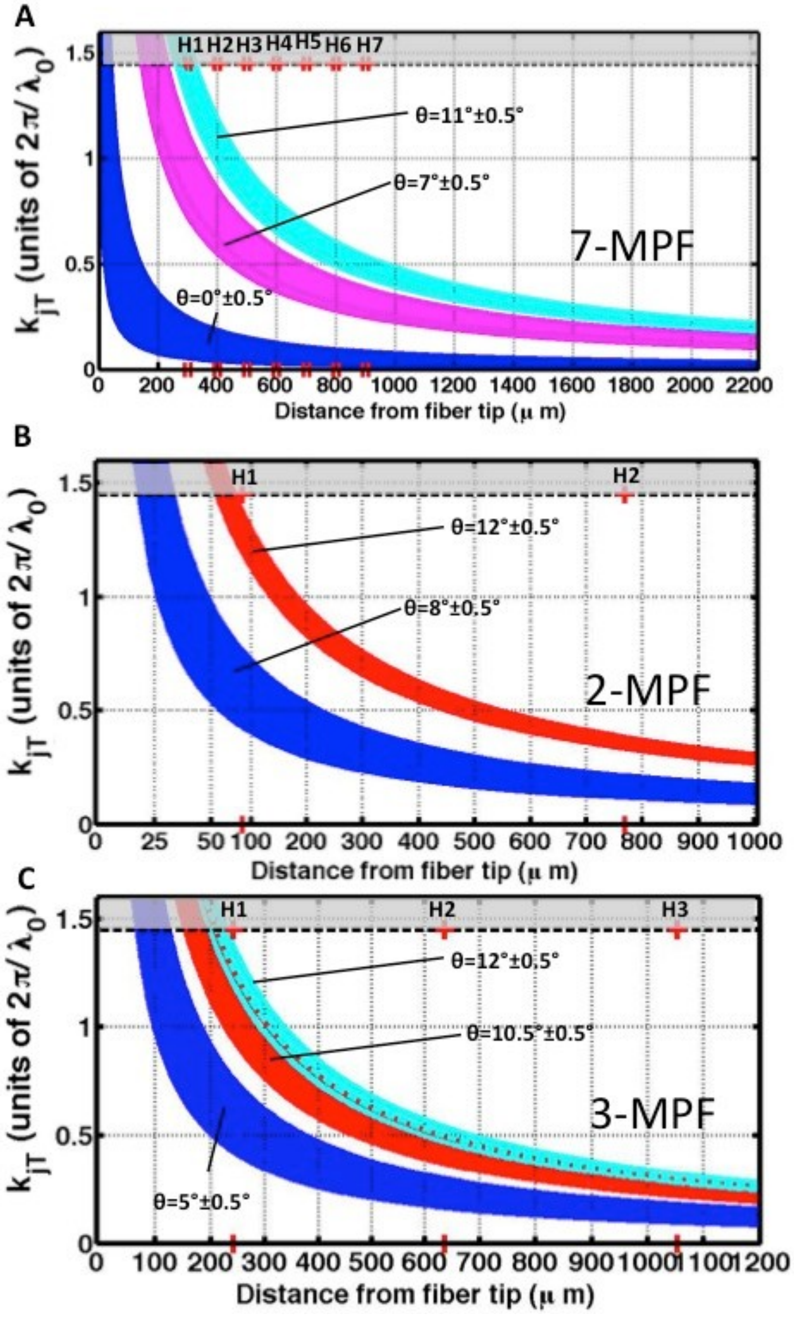

Figure A.S2, Related to Figure A3. Panels A, B and C: evolution of *kjT* as a function of the distance from taper's tip for 7-, 2- and 3-MPF, respectively.

Each filled area contains the *kjT* values for all modes carrying a light power higher than the 1% with respect to the most excited mode. Dashed line represents the *kj* value into the taper. For *kjT*> *kj*, the *j*-th mode becomes evanescent and lies in the grey area. Red symbols identify windows position along the taper.

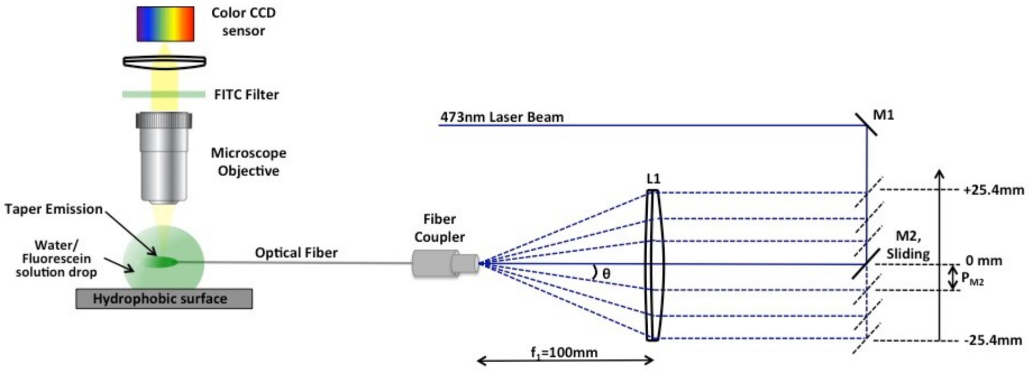

Figure A.S3, Related to Figure A3. Optical setup used for the experiments.

A 473nm CW laser is redirected on the lens L1 through two mirrors, M1 and M2. M2 is moved in order to modify the input coupling angle θ. The tapered region of the fiber is immersed in a fluorescein (in water) bath, dropcasted on a polydimethylsiloxane hydrophobic surface. The fluorescein emission is collected by means of a microscope objective and visualized by a CCD sensor through a FITC filter.

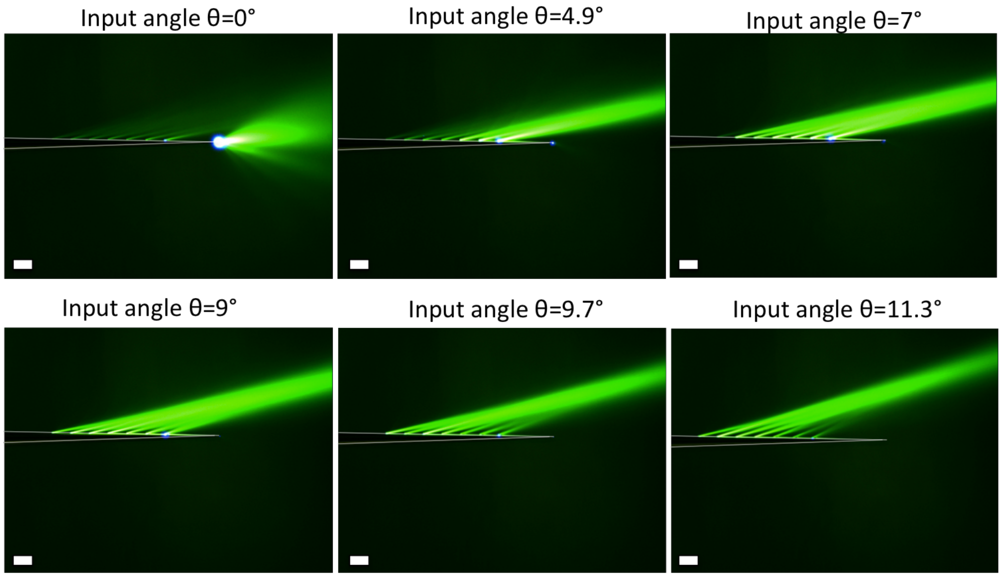
Input angle θ=0°
Input angle θ=4.9°
Input angle θ=7°
Input angle θ=9°
Input angle θ=9.7°
Input angle θ=11.3°

Figure A.S4, Related to Figure A3. Fluorescence images (side view) of taper's emission into a drop of fluorescein for different input coupling angles. Scale bars are 100μm.

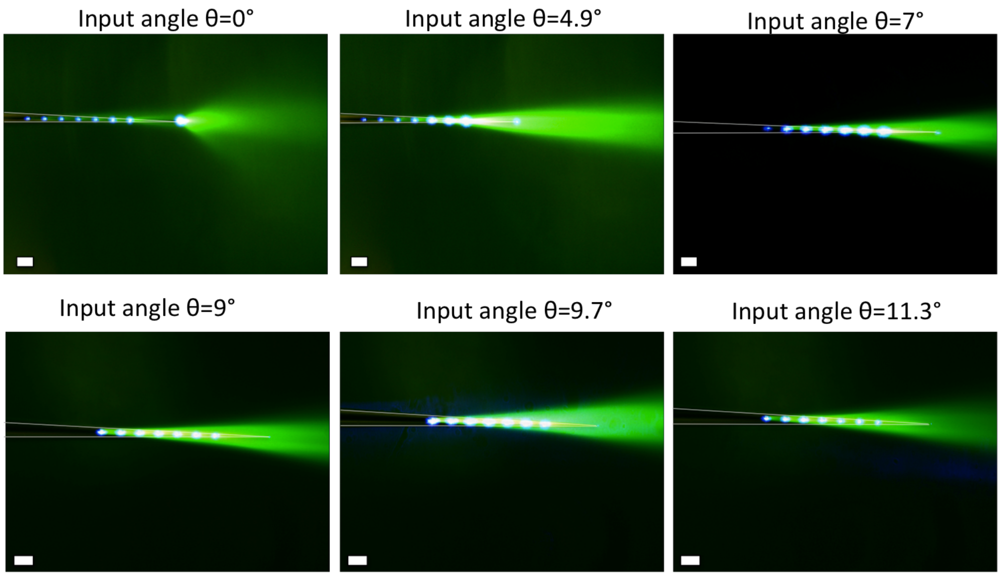

Figure A.S5, Related to Figure A3. Fluorescence images (top view) of taper's emission into fluorescein for three different input angles. Scale bars are 100µm.

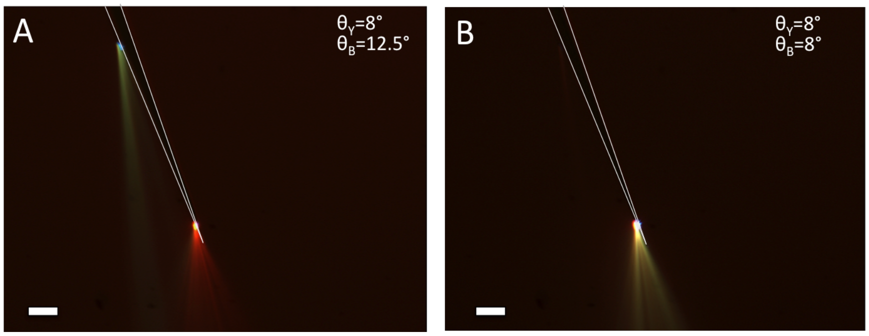

Figure A.S6, Related to Figure A5. Fluorescence images windows emission into a drop of Fluorescein:TexasRed:water solution.

Panel (A): Dual color emission from two different windows. **Panel (B):** Dual color emission from window H1. Scale bars are 100µm.

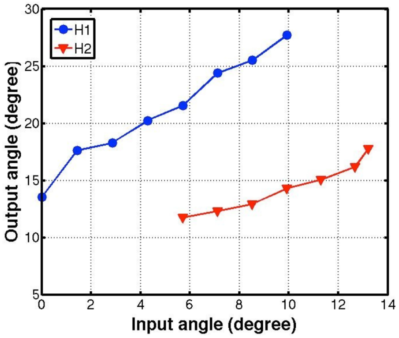

Figure A.S7, Related to Figure A5. Output angles as a function of input coupling angle θ for a 2-MPF when a yellow laser (λY=593nm) is coupled to its distal end.

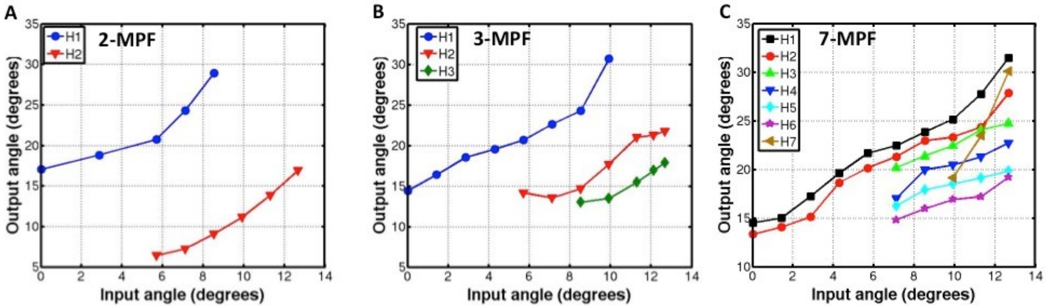

Figure A.S8, Related to Figure A4. Output angles as a function of input coupling angle θ for multi-point emitting optical fibers inserted into fluorescein stained coronal mouse brain slices.

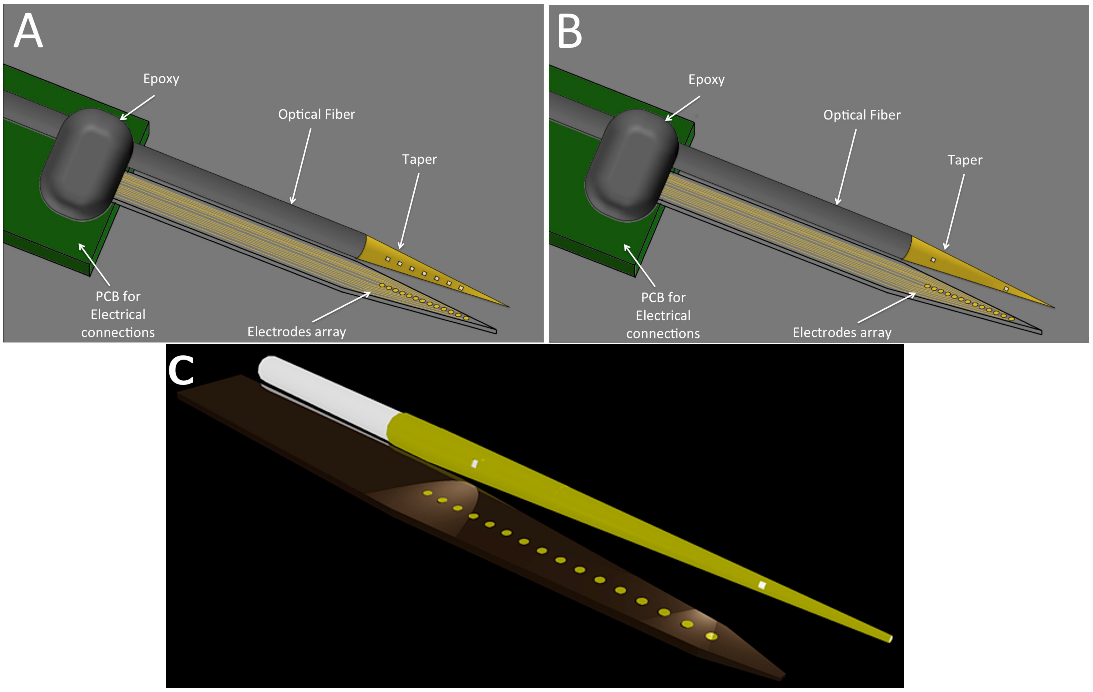

Figure A.S9, Related to Figure A.6.

Panels (A) and (B): Schematic representation of the realized optrode with a 7-MPF (panel A) or a 2-MPF (panel B). Panel (C): CAD detail of a 2-MPF.

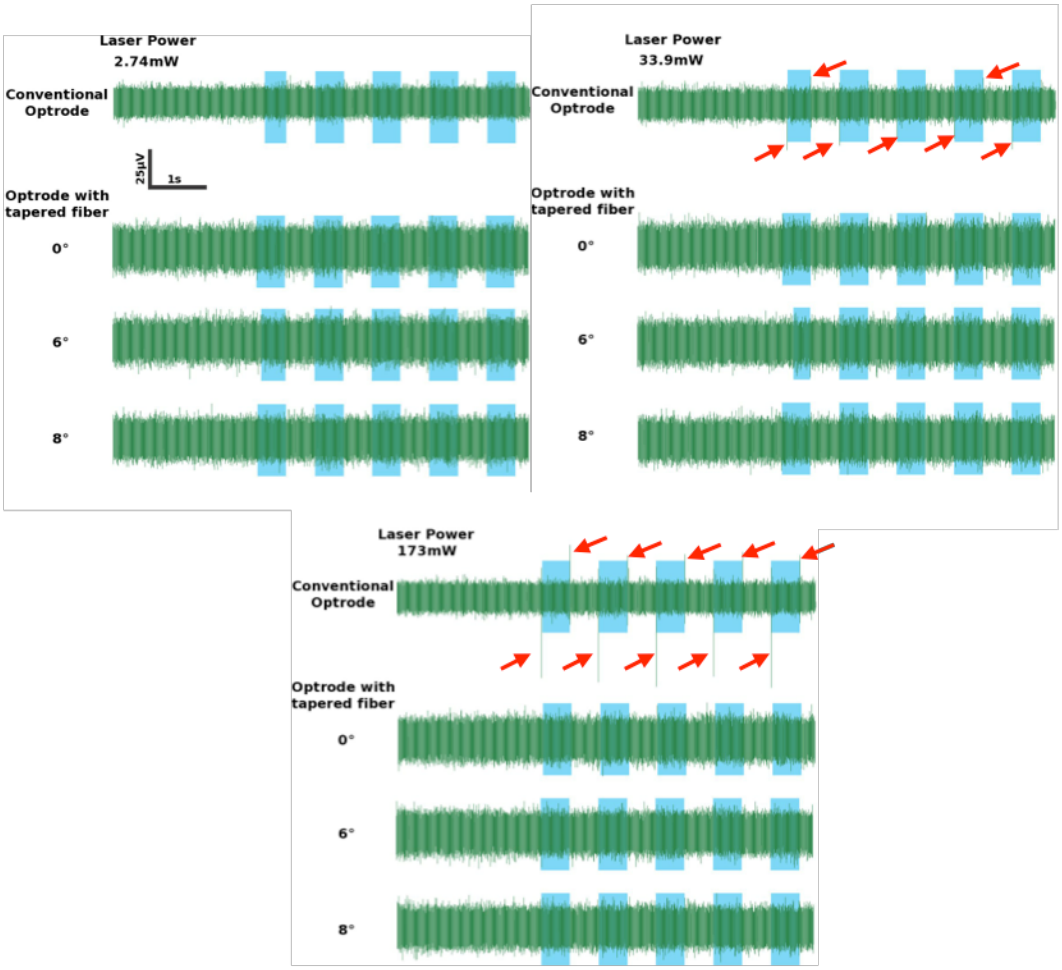

Figure A.S10, Related to Figure A6. Photoelectric effect in PBS bath.

Raw time traces recorded in a PBS bath for conventional A1x16-3mm-50-413-OA16-50 optrode from Neuronexus Technologies Inc. and the optrode based on our tapered optical fiber. Light blue area represent light ON periods. Red arrows highlight the photoelectrical effect observed at ON-OFF and OFF-ON laser transitions.

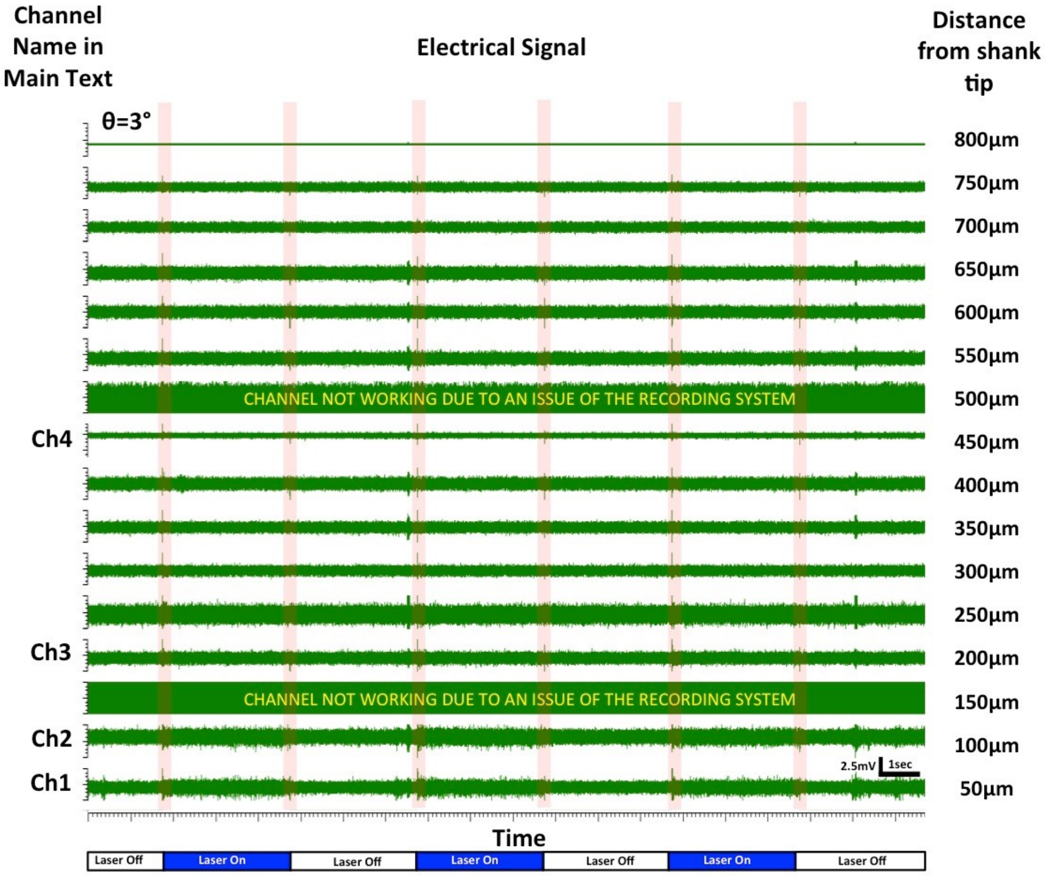

Figure A.S11, Related to Figure A6. In-vivo photoelectric effect at θ=3°.

Raw data collected at θ~3° during in-vivo experiments. Input laser power was tuned to about 11.8 mW. Photoelectric noise is detected at both onset and offset of light ON periods (highlighted by red regions). Recording sites at 150µm and 500µm from the shank's tip recorded a very high noise due to a problem of the signal amplification system for those channels.

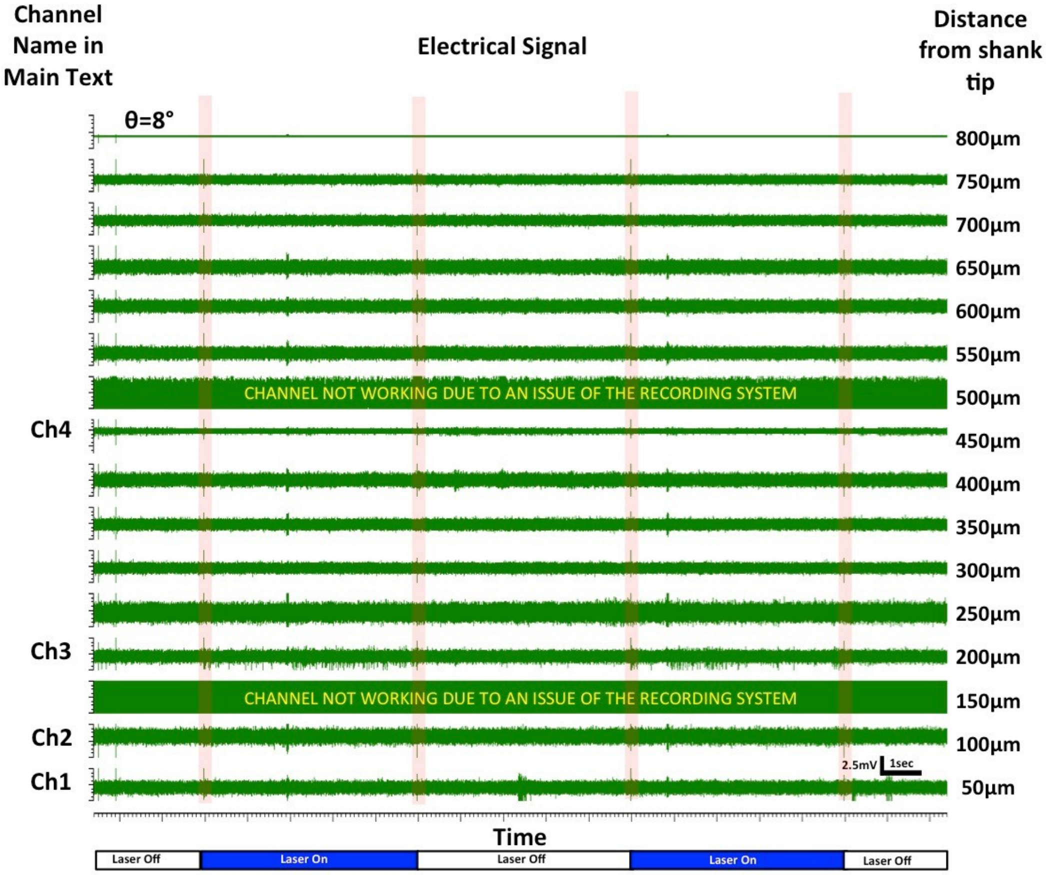

Figure A.S12, Related to Figure A6. In-vivo photoelectric effect at θ=8°.

Raw data collected at θ~8° during in-vivo experiments. Input laser power was tuned to about 33.9 mW. Photoelectric noise is detected at both onset and offset of light on periods (highlighted by red regions). Recording sites at 150µm and 500µm from the shank's tip recorded a very high noise due to a problem of the signal amplification system.

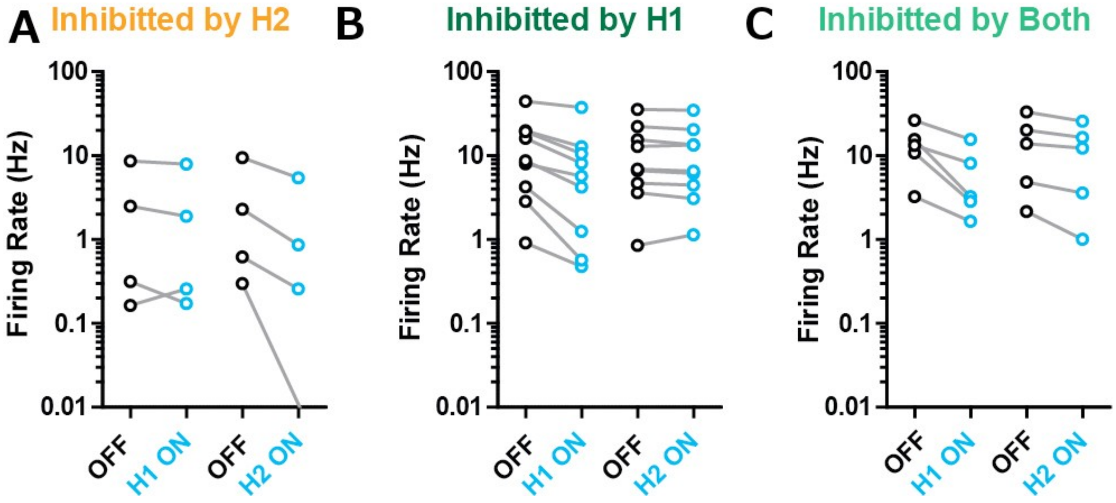

Figure A.S13, Related to Figure A6. Spiking rate summary of stable isolated units recorded during *in vivo* experiments with 2-MPFs.

Panel (A) Four units were inhibited by activating H2 but not by activating H1. **Panel (B)** Nine units were inhibited by activating H1 but not by activating H2. **Panel (C)** Five units were inhibited by activating H1 or H2

SUPPLEMENTAL EXPERIMENTAL PROCEDURES

I- Influence of taper on wavevector transversal component

Figure A.S2 shows k_{jT} variation along the taper for several values of θ for the three MPFs. At θ~0° some modes reach the taper tip, and are emitted by the circular aperture, but weak emission occurs from the side windows, due the low k_{jT} values at windows along the taper. When θ is increased the injected modes evanesce just after the window closest to the tip, whereas their higher k_{jT} enables efficient radiation from the optical aperture near the tip. For even higher θ angles light out-coupling at windows farther from the taper tip is facilitated by the higher k_{jT} of injected modes, reducing radiation from apertures close to the tip.

II- Extended details on fluorescein experiments

We here give more details on experimental results obtained with the fiber immersed in a fluorescein-water bath. The optical setup used for the fluorescein experiments is displayed in **Figure A.S3**, reporting also relative distances of optical elements, whereas **Figure A.S4** extends the data presentation of **Figure A.3D1-D3**, showing the obtained results for other input coupling angles. For completeness, in **Figure A.S5** we show a top view (*yz* plane, see **Figure A.1A** for axis definition) of the emission from the optical windows, as a function of θ. **Figures A.S6 and A.S7** extend the results shown in **Figure A.5** concerning the multi-wavelength excitation.

III-Optrode assemblying

The optrodes were realized by coupling together a 7-MPF or a 2-MPF and a commercial array of microelectrodes realized on a silicon shank (model A1x16 – 5mm – 50 – 177 – A16 from Neuronexus inc.). The fiber taper tip was aligned with the tip of the microelectrode shank, and the optical windows were oriented to illuminate the region just above the recording sites (see schematic representations in **Figure A.S9** and the optical microscope image in **Figure A.5A**). The optical fiber was secured with UV curable epoxy on the same PCB on which the silicon shank was previously soldered.

IV-Photoelectric Effect

Light mediated artifacts (due to the Becquerel photoelectric effect) are common in optrode recordings (S.K. Khijwania et al., 2009; X. Han *et al.* 2009). Our tapered fiber-electrode was designed to guide light away from the recording sites minimizing these artifacts. To compare the light mediated artifact we compared a conventional optrode (model A1x16-3mm-50-413-OA16-50 from Neuronexus Inc.) to our tapered fiber electrode in a saline bath. Light artifacts are readily visible at P_{FC}=33.9mW input power on the traditional optrode but are not visible at any input angle, even at P_{FC}=173mW input power, on the tapered fiber electrode, as shown in the sample traces displayed in **Figure A.S10**.

As mentioned in the main text, in *in-vivo* experiments photoelectrical artifacts at the initiation and termination of light ON periods were recorded also by the optrode based on tapered fibers, as displayed in the sample raw data reported in **Figures A.S11 and A.S12**. We attribute this phenomenon to the fact that tissue scattering redirect part of the light on the recording sites, leading to photoelectric effect.

SUPPLEMENTAL REFERENCES

Khijwania, S.K., Carter, F.D., Foley, J.T., and Singh, J.P. (2009). Effect of launching condition on modal power characteristics of multi-mode step-index optical fiber: a theoretical and experimental investigation. Fiber and Integrated Optics *29*, 62-75.

Novotny, L., and Hecht, B. (2006). Principles of nano-optics (Cambridge university press).

Snyder, A.W. (1969). Excitation and scattering of modes on a dielectric or optical fiber. Microwave Theory and Techniques, IEEE Transactions on *17*, 1138-1144.

Snyder, A.W., and Love, J. (1983). Optical waveguide theory, Vol 190 (Springer)